

Optical Properties of Semiconductor Nanostructures in Magnetic Field

DISSERTATION

zur Erlangung des akademischen Grades
doctor rerum naturalium
(Dr. rer. nat.)
im Fach Physik

eingereicht an der
Mathematisch-Naturwissenschaftlichen Fakultät I
Humboldt-Universität zu Berlin

von
Herrn Magister Michal Grochol
geboren am 22.10.1979 in Ostrava, Tschechische Republik

Präsident der Humboldt-Universität zu Berlin:
Prof. Dr. Christoph Marksches

Dekan der Mathematisch-Naturwissenschaftlichen Fakultät I:
Prof. Dr. Christian Limberg

Gutachter:

1. Prof. Dr. R. Zimmermann (HU Berlin)
2. PD Dr. B. Esser (HU Berlin)
3. Prof. Dr. P. Vogl (TU München)

eingereicht am: 15. Januar 2007
Tag der mündlichen Prüfung: 03. April 2007

Abstract

In this work, the near bandgap linear optical properties of semiconductor quantum structures under applied magnetic field are investigated. These properties are determined mainly by a quasi-particle consisting of one electron and one hole called exciton.

First, the exciton theory is developed starting with the one-electron Hamiltonian in a crystal, continuing with the Luttinger and Bir-Pikus Hamiltonian, and ending with the exciton Hamiltonian in the envelope function approximation. Further, concentrating on the quantum well and thus assuming strong confinement in the growth (z -) direction, the motion parallel and perpendicular to the xy -plane is factorized leading to the well-known single sublevel approximation. A magnetic field perpendicular to the xy -plane is applied, and a general theorem describing the behavior of the energy eigenvalues is derived. This theorem is generally valid for any many-particle system. Last but not least, the strain calculation within the isotropic elasticity approach is described in detail.

Second, disorder is taken into account. After discussing its properties, the standard ansatz of factorizing exciton relative and center-of-mass motion is introduced. The Schrödinger equation is solved numerically for both the full model and the factorization with artificially generated disorder potentials showing that the differences between them are pronounced especially for tail states. From the physical point of view it is shown that (i) the diamagnetic shift, i. e. energy change with magnetic field, is inversionally proportional to the localization of the wave function, (ii) the distribution of the diamagnetic shifts of individual exciton states exists and these shifts are non-monotonic in energy, (iii) the average value of the diamagnetic shift increases with energy, and (iv) absorption and consequently photoluminescence spectra become wider with increasing magnetic field.

Furthermore, having structural information from the cross-sectional scanning tunneling microscopy of a given sample available, the statistical properties of the disorder in a real quantum well have been analyzed. This analysis enabled the numerical generation of new lateral disorder potentials which served as input in the simulation of exciton optical properties. In particular, temperature dependent photoluminescence spectra and diamagnetic shift statistics, have been compared with the experimental ones and very good agreement has been found.

The second part of this thesis deals predominantly with highly symmetrical structures embedded in the quantum well: namely quantum rings and

dots. First, adopting an ansatz for the wave function, the Hamiltonian matrix is derived discussing which matrix elements are non-zero according to the symmetry of the potential. Additionally, the expectation values of the current and magnetization operators are evaluated. Then, concentrating on the case of the highest (circular) symmetry, the model of zero width ring is introduced. Within this model the close relation between the oscillatory component of the exciton energy (*exciton Aharonov-Bohm effect*) and the persistent current is revealed. Examples for different material systems follow revealing the importance of the relation between exciton Bohr radius and ring diameter for oscillations and persistent current to be observed. The circular quantum dot is treated briefly. Finally, a case of the non-circular ring is discussed and it is shown that oscillations can be observed although with lower amplitude compared to circular case.

Finally, the exciton emission kinetics is calculated, too. The limitations of the experimental observability of energy oscillations, photoluminescence quenching, caused by non-zero non-radiative channels are disclosed.

Keywords:

Exciton, Magnetic field, Nanostructures, Optical properties, Kinetics

Zusammenfassung

In dieser Arbeit werden die linearen optischen Eigenschaften von Halbleiter-Nanostrukturen in der Nähe der Bandlücke im Magnetfeld untersucht. Diese Eigenschaften werden hauptsächlich vom Quasiteilchen Exziton, das aus einem Elektron und einem Loch besteht, bestimmt.

Zuerst wird die Exziton-Theorie entwickelt: Beginnend mit dem Hamilton-Operator eines Elektrons im Kristall wird der Luttinger- und Bir-Pikus-Hamilton-Operator entwickelt, und schließlich wird der Hamilton-Operator eines Exzitons in der Enveloppen-Näherung aufgestellt. In weiteren wird ein Quantengraben betrachtet, wo eine starke Beschränkung der Wellenfunktion in der Wachstumsrichtung (z -Richtung) angenommen werden kann, und die Bewegung parallel und senkrecht zur xy -Ebene faktorisiert. Das führt zur bekannten Näherung des isolierten Sublevels. Für ein senkrecht angelegtes Magnetfeld wird ein allgemeines Theorem für das Verhalten der Energie-Eigenwerte abgeleitet. Dieses Theorem gilt auch für mehrere Teilchen. Die Berechnung der Verzerrung des Halbleitermaterials in der Näherung der isotropen Elastizität wird im Detail beschrieben.

Zweitens wird die Unordnung berücksichtigt und ihre Eigenschaften diskutiert. Der übliche Ansatz für die Faktorisierung in Schwerpunkt- und Relativ-Bewegung des Exzitons wird eingeführt. Die Schrödinger-Gleichung wird für das volle Modell und die Faktorisierung mit künstlich generierten Potentialen numerisch gelöst. Die Lösung zeigt, daß die Unterschiede zwischen beiden Modellen hauptsächlich für Zustände im Ausläufer der optischen Spektren wichtig sind. Weiter wird gezeigt, daß (i) die diamagnetische Verschiebung, d. h. Änderung der Energie mit einem Magnetfeld, umgekehrt proportional zur Lokalisierung der Wellenfunktion ist, (ii) eine Verteilung der diamagnetischen Verschiebungen der lokalisierten Zustände des Exzitons existiert, (iii) der Mittelwert der diamagnetischen Verschiebung mit der Energie anwächst, und (iv) Absorptions- und Photolumineszenz-Spektren mit dem Magnetfeld breiter werden.

Drittens werden die statistischen Eigenschaften der Unordnung in einem realen Quantengraben analysiert, von dem strukturelle Informationen verfügbar waren, die mit dem Raster-Tunnelmikroskop an einer Querschnittsfläche gewonnen wurden. Diese Analyse ermöglicht die numerische Erzeugung neuer Unordnungspotentiale, die dann für die Simulation der optischen Eigenschaften benutzt wurden. Insbesondere temperaturabhängige Photolumineszenz-Spektren und die Statistik der diamagnetischen Verschiebungen wurden mit

den experimentellen Daten verglichen, wobei eine sehr gute Übereinstimmung gefunden wurde.

Der zweite Teil dieser Dissertation beschäftigt sich überwiegend mit hochsymmetrischen Strukturen eingebettet im Quantengraben, nämlich Quantenringen und Quantenpunkten. Mit einem Ansatz für die Wellenfunktion wird die Hamilton-Matrix abgeleitet, wobei der Zusammenhang zwischen nichtverschwindenden Matrixelementen und der Symmetrie des Potentials diskutiert wird. Zusätzlich werden die Erwartungswerte des Stromoperators und der Magnetisierung ausgewertet. Dann wird die höchste (zirkuläre) Symmetrie angenommen und das Modell eines Ringes mit verschwindender Breite eingeführt. Im Rahmen dieses Modells wird der enge Zusammenhang zwischen der oszillatorischen Komponente der Exziton-Energie (*Aharonov-Bohm Effekt des Exzitons*) und dem persistenten Strom aufgezeigt. Es folgen einige Beispiele für unterschiedliche Materialien, die den engen Bezug zwischen dem Bohr-Radius des Exzitons und dem Durchmesser des Ringes im Hinblick auf die Beobachtbarkeit der Oszillationen und des persistenten Stroms zeigen. Zirkuläre Quantenpunkte werden kurz behandelt. Schließlich wird der Fall eines nichtzirkulären Ringes diskutiert und gezeigt, daß Oszillationen beobachtbar sein sollten, obwohl mit kleinerer Amplitude im Vergleich zum zirkulären Ring.

Zum Schluß wird die Kinetik der Emission des Exzitons behandelt. Einschränkungen der Beobachtbarkeit der oszillatorischen Komponente der Exziton-Energie werden aufgezeigt, die mit der Unterdrückung der Photolumineszenz durch nichtradiative Prozesse zusammenhängen.

Schlagwörter:

Exziton, Magnetfeld, Nanostrukturen, Optische Eigenschaften, Kinetik

Dedication

To all those who had endless patience with me during the time I have been working on this thesis.

Všem těm, kteří se mnou měli nekonečnou trpělivost během práce na této dizertaci.

Contents

I	Introduction	1
II	Exciton in Quantum Well	7
1	Theoretical approach	9
1.1	Crystalline and electronic properties	9
1.2	k.p analysis	10
1.3	Luttinger and Bir-Pikus Hamiltonian	12
1.4	Envelope function approximation	15
1.5	Exciton in ideal bulk	17
1.6	Exciton in ideal quantum well in zero magnetic field	20
1.7	Exciton in ideal quantum well in non-zero magnetic field	23
1.7.1	General properties	24
1.7.2	Optical activity	27
1.8	Electron effective mass enhancement	28
1.9	Strain	30
1.9.1	Basics	30
1.9.2	Isotropic elasticity	31
2	Disordered Quantum Well	35
2.1	Hamiltonian	35
2.2	Disorder	37
2.3	Rigid exciton approximation	39
2.4	Analysis of the wave function	40
2.5	Comparison between full solution and factorization	41
2.5.1	No magnetic field	41
2.5.2	Diamagnetic shift	44
2.6	Diamagnetic shift and wave function localization	48
2.7	Enhanced electron effective mass	50
2.8	Real quantum well	51
2.8.1	Experiment	52

2.8.2	Potential reconstruction and generation	54
2.8.3	Micro-photoluminescence	57
2.8.4	Diamagnetic shift coefficient	61
III	Exciton in Quantum Ring	63
3	Quantum Ring	65
3.1	Hamiltonian	66
3.2	Persistent current and magnetization	69
3.3	Circular quantum ring	71
3.3.1	Zero width ring	71
3.3.2	Exciton Aharonov-Bohm effect	75
3.3.3	Persistent current and magnetization	86
3.4	Circular quantum dot	87
3.5	Non-circular quantum ring	90
4	Emission kinetics	97
4.1	Theory	97
4.2	Circular quantum ring of zero width	101
4.3	Non-circular quantum ring of zero width	104
IV	Summary and Outlook	107
V	Appendices	111
A	Material parameters	113
B	Gauge transformation	115
B.1	Choice of the gauge	115
B.2	Numerical implementation	116
C	Numerics	117
C.1	Leapfrog method	117
C.2	Implementation and tests	118
C.3	Lanczos method	120
D	Correlation function	121
E	Radiative rates	123

F Strain	125
F.1 Dot	125
F.2 Ring	127
G List of abbreviations	129
Bibliography	131
Zusätzliches Material	143
Danksagung	143
Lebenslauf	145
Aufstellung der wissenschaftlichen Veröffentlichungen	147
Selbständigkeitserklärung	151

Part I
Introduction

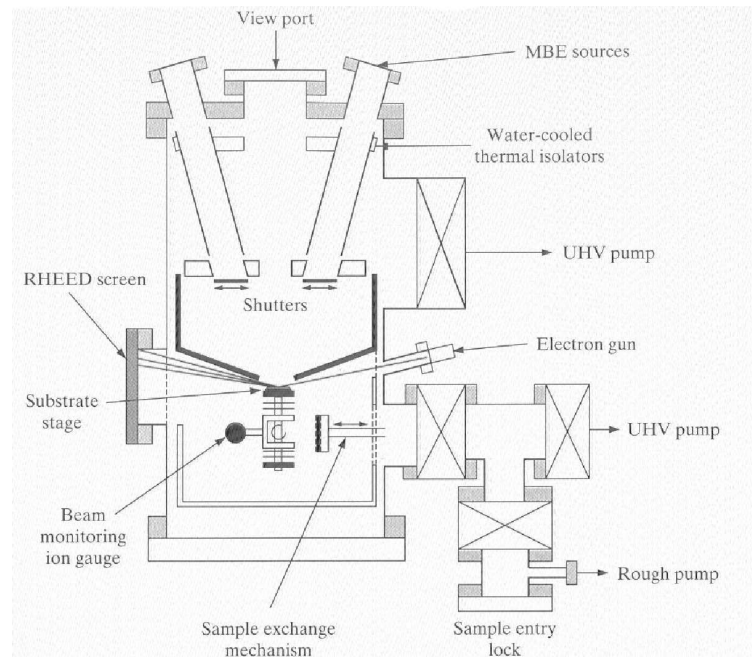


Figure 1: The schematic picture of the molecular beam epitaxy [YC94].

The semiconductor nanostructures like quantum wells, wires or dots have been investigated now for more than 30 years. They have found a giant number of applications in the technology, just to mention few of them: lasers, light emitting diodes, light detectors or transistors. This number is still increasing and these structures are nowadays considered to be even more perspective for future applications e.g. for quantum computing. This is one of the reasons why after such a long time the amount of research performed on this field does not decrease but grows further.

The scientific interest and technological progress would not be thinkable without the key invention: molecular beam epitaxy (MBE) [CA75]. This method (schematically plotted in Fig. 1) enables to grow structures layer by layer with very high quality. The structures with excellent properties like very high carrier mobility or optical yield are grown in this way. Unfortunately, due to many reasons these structures are even with this advanced method far from being ideal due to e. g. the rough interfaces between two materials or random position of atoms in an alloy. Among other methods used to grow such structures metal oxide chemical vapor deposition [Dap82] should be mentioned.

Due to the strong dependence of transport and optical properties on the applied magnetic and electric field, the two-dimensional planar structures

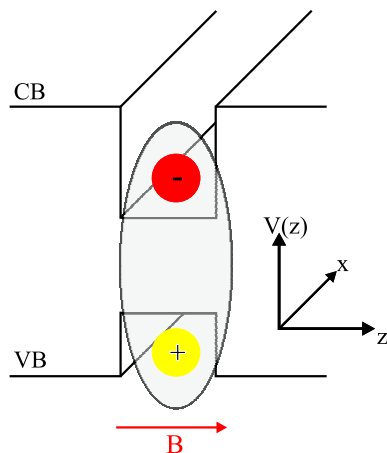


Figure 2: The schematic picture of the ideal quantum well. The conduction (CB) and valence (VB) band profiles with electron (-) and hole (+) are indicated.

(quantum wells, schematically shown in Fig. 2), coupled quantum wells and multiple quantum wells) have been under focus. The mostly used material for fabricating these structures is GaAs/AlGaAs thanks to its properties: (i) direct bandgap of the ternary alloy (up to 40% of the Aluminum concentration) and (ii) practically the same lattice constant of GaAs and AlAs, which reduces the strain substantially.

The technological importance of the quantum wells and related structures makes it necessary to investigate the influence of imperfections on physical properties. There is the well-known model of disorder introduced by Anderson [And58] which predicts that according to the strength of disorder the transition (mobility edge) between conducting (delocalized wave function of the carrier) and non-conducting (localized wave function) regime exists.

Like transport also optical properties give information about disorder. The linear optical properties near the bandgap of the semiconductor are dominated by the quasi-particle called *exciton*, consisting of the electron in the conduction band and the hole in the valence band. The sensitivity to the disorder of *the magnetic field* dependent exciton properties like inhomogeneous line-width of the absorption and photoluminescence spectra and diamagnetic shift of the localized excitons enable to learn a lot of about underlying structure. Several experimental techniques have been developed to obtain as much detailed information as possible like: Microphotoluminescence [ZBH⁺94; BAB⁺94; GSK95], scanning near-field optical spectroscopy [HBH⁺94], and cathodoluminescence [RMJ⁺95]. The theoretical approaches to this phenomena, which will be discussed in detail in Chap-

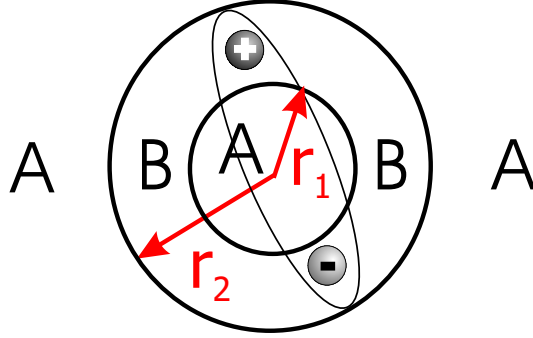


Figure 3: The schematic picture of the ideal quantum ring in xy -plan. Two materials A and B are distinguished.

ter 2, have been developed successfully. There is an excellent agreement between theory and experiment showing how much about disorder has been understood.

However, it may seem surprising that there is only a little experimental work that directly confirms the connection between structure and optics in simple situations. By "directly" we mean that the structural properties of a given sample are measured as precisely as possible (e. g. by transmission electron microscopy [OTC89], X-ray diffraction [Fle80], or scanning tunneling microscopy [LZY⁺98]) and predictions on the optical properties are made from the structural data, and that those are contrasted by an optical experiment.¹ We will address this open question in Chapter 2, too.

The second part of this thesis deals with ideal structures (like quantum ring² which is schematically plotted in Fig. 3) embedded in the quantum well. Unlike in the first part, magnetic field is not a tool to get some information about disorder but induces qualitatively new effects: exciton Aharonov-Bohm effect (ABE) [AB59] and exciton persistent current. Even though we focus on the structures which are very hard to grow [GMRS⁺97; MKS⁺05] and we find effects which are hard to observe experimentally, they are surprising on the first glance since the exciton as a neutral (composite) particle should interact with magnetic field only weakly.

The original ABE is found only for charged particles [AB59] as a purely quantum mechanical effect showing the important role of the vector potential. The ground state energy of a charged particle oscillates with the magnetic flux $\Phi_B = \oint \mathbf{B} \cdot d\mathbf{S}$. If the particle orbits in a ring around an

¹Relaxing mentioned criteria there are methods that investigate experimentally and theoretically semiconductor optical properties near bandgap like e.g. comparative studies of ion-beam induced defect formation in crystalline solids [WMBW94].

²We will use throughout this thesis the names quantum ring and nanoring equivalently.

infinitely long solenoid with radius r_0 where the magnetic field B is concentrated then the magnetic flux is $\Phi_B = \pi r_0^2 B$. The oscillation period is given in units of the magnetic flux quantum h/e . Shortly after its theoretical prediction the ABE has been confirmed experimentally [Cha60; MB62]. Furthermore, even recently ABE has been observed e.g. in mesoscopic metal rings [vODNM98], carbon nanotubes [BSS⁺99], and in doped semiconductor InAs/GaAs nanorings [LLG⁺00]. Last but not least, the persistent current, induced by an electron orbiting in a cylindrical film of a normal metal, has been measured for the first time in Ref. [SS81] and recently in mesoscopic metals [LDDDB90; CWB⁺91] and semiconductor rings [MCB93]. Moreover, also interacting electrons in the ring exhibit both ABE and the persistent current [WF95; WFC95].

This thesis is divided into two parts: The first one deals with excitons in quantum well under applied magnetic field. First, we start with the descriptions of our theoretical approach (Chapter 1) and then we focus on the exciton in the disordered quantum wells (Chapter 2), performing demanding numerical simulations. In the second part we add another nanostructures, either quantum dot or ring, into the ideal quantum well. We concentrate on the energy, persistent current, and magnetization as a function of the magnetic field in Chapter 3. The emission kinetics is investigated in Chapter 4. The results are summarized in Chapter 5. Many calculations are described in detail in the appendices.

Part II

Exciton in Quantum Well

Chapter 1

Theoretical approach

The theory of exciton in the quantum well is developed in this chapter. We start with the crystal structure and adopting justified approximations we succeed to reduce the dimensionality and complexity of the problem enormously. Finally, we end with the rather simple two-particle and two dimensional exciton Hamiltonian which we solve without any further approximations and lateron compare the results with the experiment in Chapter 2.

1.1 Crystalline and electronic properties

The III-V compounds which are the object of our interest crystallize in the zincblende structure. The first Brillouin zone of the reciprocal lattice is a truncated octahedron (see Fig. 1.1). Several high symmetry points or lines of the first Brillouin zone have received specific notations, e.g. X, L and Γ points. In a III-V binary material like GaAs, there are 8 electrons per unit cell (3 from Ga and 5 from As) which contribute to the chemical bounds. We can say that the orbital of every atom hybridize (due to interaction with his neighbors) to form bonding and antibonding state which broaden into bands because of a great number of unit cells interacting. Two electrons fill the s -band and remaining six electrons occupy the p -bands. Antibonding bands are empty and the lowest lying one forms the conduction band (representation Γ_6^1 in the Γ point). All III-V compounds have the top of the valence band in the center of Brillouin zone. The spin-orbit coupling lowers the sixfold degeneracy in the point Γ , and gives rise to a quadruplet with

¹There are five irreducible representations of the cubic symmetry group T_d . Taking into account spin-orbit coupling this number is increased since the spin is not invariant to the rotation by the angle 2π . The eight representations Γ_{1-8} of double groups are formed [YC94].

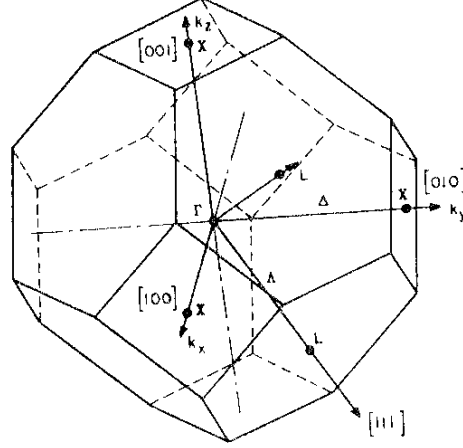


Figure 1.1: First Brillouin zone of face-centred cubic lattice, taken from [Bas92].

$J = 3/2$ (representation Γ_8) and a doublet $J = 1/2$ (representation Γ_7). The conduction band edge of the III-V materials is situated near one of the points Γ , L or X . The heavier the cation the more likely it is to find band edge in the point Γ .

1.2 k.p analysis

The starting point of our approach is the one-electron Schrödinger equation in a bulk crystal which takes the form of

$$\left[\frac{p^2}{2m_0} + V(\mathbf{r}) + \frac{\hbar^2}{4m_0^2c^2} (\boldsymbol{\sigma} \times \nabla V) \cdot \mathbf{p} + H_r \right] \Psi(\mathbf{r}) = E\Psi(\mathbf{r}), \quad (1.1)$$

where $V(\mathbf{r})$ is the crystalline potential which includes an average of the electron-electron interaction and is periodic with the period of the Bravais lattice. The third term is the spin-orbit coupling and the fourth term is the relativistic correction (mass-velocity and Darwin term). The solution of Eq. (1.1) can be written in the Bloch form:

$$\Psi_{n\mathbf{k}}(\mathbf{r}) = N u_{n\mathbf{k}}(\mathbf{r}) \exp(i\mathbf{k} \cdot \mathbf{r}), \quad (1.2)$$

where N is a normalization coefficient and $u_{n\mathbf{k}}(\mathbf{r})$ is a periodic function of \mathbf{r} with the period of the lattice. The periodic parts of the Bloch functions

$u_{n\mathbf{k}}(\mathbf{r})$ are the solutions of (dropping the relativistic corrections)

$$\left[\frac{p^2}{2m_0} + V(\mathbf{r}) + \frac{\hbar^2}{4m_0^2c^2} (\boldsymbol{\sigma} \times \nabla V) \cdot \mathbf{p} + \frac{\hbar^2 k^2}{2m_0} + \frac{\hbar \mathbf{k}}{2m_0} \cdot \left(\mathbf{p} + \frac{\hbar^2}{4m_0^2c^2} (\boldsymbol{\sigma} \times \nabla V) \right) \right] u_{n\mathbf{k}}(\mathbf{r}) = \varepsilon_{n\mathbf{k}} u_{n\mathbf{k}}(\mathbf{r}). \quad (1.3)$$

The \mathbf{k} -dependent terms in (1.3) vanish at $\mathbf{k}=0$ and commute with the translation operator. The functions $u_{m\mathbf{0}}(\mathbf{r})$ form a complete basis and can be used to investigate the energy dispersion $\varepsilon_{n\mathbf{k}}$ and wave function properties for small \mathbf{k}

$$u_{n\mathbf{k}}(\mathbf{r}) = \sum_m c_m(\mathbf{k}) u_{m\mathbf{0}}(\mathbf{r}). \quad (1.4)$$

By inserting (1.4) into (1.3), multiplying by $u_{n\mathbf{0}}^*(\mathbf{r})$ and integrating over a unit cell we obtain:

$$\sum_m \left\{ \left(\varepsilon_{n\mathbf{0}} - \varepsilon_{n\mathbf{k}} + \frac{\hbar^2 k^2}{2m_0} \right) \delta_{nm} + \frac{\hbar \mathbf{k}}{m_0} \cdot \langle n\mathbf{0} | \mathbf{p} + \frac{\hbar^2}{4m_0^2c^2} (\boldsymbol{\sigma} \times \nabla V) | m\mathbf{0} \rangle \right\} c_m(\mathbf{k}) = 0, \quad (1.5)$$

where

$$\langle n\mathbf{0} | A | m\mathbf{0} \rangle = \int_{\text{unit cell}} u_{n\mathbf{0}}^*(\mathbf{r}) A u_{m\mathbf{0}}(\mathbf{r}) d^3r. \quad (1.6)$$

The Eq. (1.5) is well suited for the perturbation approach. Supposing that the n^{th} band edge is *non-degenerate*, we can then assume for small \mathbf{k} :

$$c_n(\mathbf{k}) \sim 1; \quad c_m(\mathbf{k}) = \alpha \cdot \mathbf{k}, \quad (1.7)$$

which inserted in Eq. (1.5), results in

$$c_m(\mathbf{k}) = \frac{\hbar \mathbf{k}}{m_0} \cdot \boldsymbol{\Pi}_{nm} \frac{1}{\varepsilon_{n\mathbf{0}} - \varepsilon_{m\mathbf{0}}}, \quad (1.8)$$

and gives the second order correction to $\varepsilon_{n\mathbf{0}}$:

$$\varepsilon_{n\mathbf{k}} = \varepsilon_{n\mathbf{0}} + \frac{\hbar^2 k^2}{2m_0} + \frac{\hbar^2}{m_0} \sum_{m \neq n} \frac{|\boldsymbol{\Pi}_{nm} \cdot \mathbf{k}|^2}{\varepsilon_{n\mathbf{0}} - \varepsilon_{m\mathbf{0}}}. \quad (1.9)$$

The vector $\boldsymbol{\Pi}$ is defined as:

$$\boldsymbol{\Pi} = \mathbf{p} + \frac{\hbar^2}{4m_0^2c^2} (\boldsymbol{\sigma} \times \nabla V). \quad (1.10)$$

As long as \mathbf{k} is small ($\varepsilon_{n\mathbf{k}} - \varepsilon_{n\mathbf{0}}$ remains much smaller than all band edge gaps $\varepsilon_{n\mathbf{0}} - \varepsilon_{m\mathbf{0}}$) the dispersion relations of the non-degenerate bands are parabolic in \mathbf{k} in the vicinity of the Γ point.

$$\varepsilon_{n\mathbf{k}} = \varepsilon_{n\mathbf{0}} + \frac{\hbar^2}{m_0} \sum_{\alpha,\beta} k_\alpha \frac{1}{\mu_n^{\alpha\beta}} k_\beta, \quad (1.11)$$

where

$$\frac{1}{\mu_n^{\alpha\beta}} = \frac{1}{m_0} \delta_{\alpha\beta} + \frac{2}{m_0^2} \sum_{m \neq n} \frac{\Pi_{mn}^\alpha \Pi_{nm}^\beta}{\varepsilon_{n\mathbf{0}} - \varepsilon_{m\mathbf{0}}}, \quad (1.12)$$

$\mu_n^{\alpha\beta}$ is the effective mass tensor which describes the carrier kinematics in the vicinity of the zone center and for the energy close to the n^{th} band edge. Assuming the validity of Eq. (1.12) the overall effects of the band structure are embodied in the use of an effective mass instead of the free electron mass. This approach is well suited for the lowest conduction band (Γ_6).

1.3 Luttinger and Bir-Pikus Hamiltonian

In the case of degenerate bands the simple perturbation theory cannot be used. Instead a different approach is developed. The most important is the case of the topmost 6 valence bands which are treated exactly in the $\mathbf{k} \cdot \mathbf{p}$ approach and the coupling to higher conduction bands is included within the perturbation theory [YC94]. Taking into account the spin-orbit coupling $\frac{\hbar^2}{4m_0^2 c^2} (\boldsymbol{\sigma} \times \nabla V)$ only the total angular momentum

$$J = L + S, \quad (1.13)$$

where L is the orbital angular momentum and S is the spin, remains the good quantum number. There are two values of $J = 3/2$ and $1/2$ for the valence bands and corresponding basis function can be found with the help of Clebsch-Gordan coefficients $|JJ_z\rangle$

$$\begin{aligned} \left| \frac{3}{2} + \frac{3}{2} \right\rangle &= -\frac{1}{2} |(X + iY) \uparrow\rangle, & \left| \frac{3}{2} + \frac{1}{2} \right\rangle &= \frac{1}{\sqrt{6}} |-(X + iY) \downarrow + 2Z \uparrow\rangle, \\ \left| \frac{3}{2} - \frac{1}{2} \right\rangle &= \frac{1}{\sqrt{6}} |(X - iY) \uparrow + 2Z \downarrow\rangle, & \left| \frac{3}{2} - \frac{3}{2} \right\rangle &= \frac{1}{2} |(X - iY) \downarrow\rangle, \\ \left| \frac{1}{2} + \frac{1}{2} \right\rangle &= \frac{1}{\sqrt{3}} |(X + iY) \downarrow + Z \uparrow\rangle, & \left| \frac{1}{2} - \frac{1}{2} \right\rangle &= \frac{1}{\sqrt{3}} |(X - iY) \uparrow - Z \downarrow\rangle, \end{aligned} \quad (1.14)$$

where $\uparrow(\downarrow)$ is spin up (down), $|X\rangle$, $|Y\rangle$, and $|Z\rangle$ are p -like functions and their combinations $\frac{1}{2}(X + iY)$, Z , and $\frac{1}{2}(X - iY)$, which are eigenfunctions of L and L_z , are analogous to spherical harmonics. The Hamiltonian Eq. (1.1) is projected on the basis Eq. (1.14) and the coupling with the lowest conduction bands is included within the perturbation theory.

There is also a different approach where the Hamiltonian is derived using symmetry of the cubic or zinc blend lattice with effective parameters which are related to the energies coming from the $\mathbf{k}\cdot\mathbf{p}$ calculation. This Hamiltonian has been derived for the first time by Luttinger and Kohn [LK55] and the parameters are thus called Luttinger-Kohn parameters. Furthermore, Bir and Pikus have introduced strain into this Hamiltonian [BP74] which has the following complex form of [CC92]

$$H = \begin{bmatrix} P + Q & -S & R & 0 & -\frac{1}{\sqrt{2}}S & \sqrt{2}R \\ -S^\dagger & P - Q & 0 & R & -\sqrt{2}Q & \sqrt{\frac{3}{2}}S \\ R^\dagger & 0 & P - Q & S & \sqrt{\frac{3}{2}}S^\dagger & \sqrt{2}Q \\ 0 & R^\dagger & S^\dagger & P + Q & -\sqrt{2}R & -\frac{1}{\sqrt{2}}S^\dagger \\ -\frac{1}{\sqrt{2}}S^\dagger & -\sqrt{2}Q & \sqrt{\frac{3}{2}}S & -\sqrt{2}R & P + \Delta & 0 \\ \sqrt{2}R^\dagger & \sqrt{\frac{3}{2}}S^\dagger & \sqrt{2}Q & -\frac{1}{\sqrt{2}}S & 0 & P + \Delta \end{bmatrix}, \quad (1.15)$$

where

$$\begin{aligned} P &= P_k + P_\epsilon, & Q &= Q_k + Q_\epsilon, \\ R &= R_k + R_\epsilon, & S &= S_k + S_\epsilon, \\ P_k &= \left(\frac{\hbar^2}{2m_0}\right) \gamma_1(k_x^2 + k_y^2 + k_z^2), \\ Q_k &= \left(\frac{\hbar^2}{2m_0}\right) \gamma_2(k_x^2 + k_y^2 - 2k_z^2), \\ R_k &= \left(\frac{\hbar^2}{2m_0}\right) \sqrt{3}[-\gamma_2(k_x^2 - k_y^2) + 2i\gamma_3 k_x k_y], \\ S_k &= \left(\frac{\hbar^2}{2m_0}\right) 2\sqrt{3}\gamma_3(k_x - ik_y)k_z, \\ P_\epsilon &= -a_v(\epsilon_{xx} + \epsilon_{yy} + \epsilon_{zz}), \\ Q_\epsilon &= -\frac{b}{2}(\epsilon_{xx} + \epsilon_{yy} - 2\epsilon_{zz}), \\ R_\epsilon &= \frac{\sqrt{3}}{2}b(\epsilon_{xx} - \epsilon_{yy}) - id\epsilon_{xy}, \\ S_\epsilon &= -d(\epsilon_{zx} - i\epsilon_{yz}), \end{aligned} \quad (1.16)$$

where ϵ_{ij} is the strain tensor, γ_1 , γ_2 , and γ_3 are Luttinger-Kohn parameters, a_v , b , and d are Bir-Pikus deformation potentials, and Δ is the spin-orbit split-off energy. The energy zero is taken at the top of unstrained valence band.

Further assumptions can be made: Since the spin-off offsets is of order of eV, much larger than tens of meV in which we are interested, we neglect coupling between these bands and the rest. This reduces the matrix of Eq. (1.15) to 4×4 (the first submatrix). Since the hydrostatic and biaxial strain are the most important in III-IV semiconductors we restrict ourselves only to them in the following, which means

$$\begin{aligned}\epsilon_{xx} &= \epsilon_{yy} \neq \epsilon_{zz}, \\ \epsilon_{yx} &= \epsilon_{yz} = \epsilon_{zx} = 0,\end{aligned}$$

and then

$$R_\epsilon = S_\epsilon = 0. \quad (1.17)$$

The eigenenergies of the reduced 4×4 Eq. (1.15) are

$$E_1(k) = -P - \text{sgn}(Q_\epsilon) \sqrt{Q^2 + |R|^2 + |S|^2}, \quad (1.18)$$

$$E_2(k) = -P + \text{sgn}(Q_\epsilon) \sqrt{Q^2 + |R|^2 + |S|^2}. \quad (1.19)$$

The sign of Q_ϵ is important for the type of the strain: negative (positive) for compressive (tensile). The equation (1.18) can be expanded for small k and the dispersion relation can be obtained

$$E_1(k) = -P_\epsilon - Q_\epsilon - \left(\frac{\hbar^2}{2m_0} \right) [(\gamma_1 + \gamma_2)(k_x^2 + k_y^2) + (\gamma_1 - 2\gamma_2)k_z^2], \quad (1.20)$$

$$E_2(k) = -P_\epsilon + Q_\epsilon - \left(\frac{\hbar^2}{2m_0} \right) [(\gamma_1 - \gamma_2)(k_x^2 + k_y^2) + (\gamma_1 + 2\gamma_2)k_z^2], \quad (1.21)$$

and band edges are

$$E_1(0) = -P_\epsilon - Q_\epsilon, \quad E_2(0) = -P_\epsilon + Q_\epsilon. \quad (1.22)$$

The typical situation in the semiconductors is that the valence band is almost filled and only few electrons are found in the conduction band. We may look on this as there were empty places in the valence band called *holes*. The hole has positive charge and effective mass ($m_h = -m_v$) and it can be treated

as a quasi-particle. Since there are two dispersion relations, Eq. (1.20), two types of holes have to be distinguished according to their effective masses

$$m_{hh,\perp}^* = (\gamma_1 - 2\gamma_2)^{-1}m_0, \quad m_{hh,\parallel}^* = (\gamma_1 + \gamma_2)^{-1}m_0, \quad (1.23)$$

$$m_{lh,\perp}^* = (\gamma_1 + 2\gamma_2)^{-1}m_0, \quad m_{lh,\parallel}^* = (\gamma_1 - \gamma_2)^{-1}m_0, \quad (1.24)$$

where \parallel (\perp) stands for the motion in (perpendicular to) the xy -plane. Comparing the hole masses in the z -direction (perpendicular ones) the hole with larger (smaller) mass is called heavy (light). The heavy hole has smaller parallel mass than the light hole. The importance of the z -direction will be clear when discussing the quantum wells. The heavy and light hole dispersion relation can be written for clarity (omitting the superscript $*$ from now)

$$E_{hh}(k) = P_\epsilon + Q_\epsilon + \left(\frac{\hbar^2}{2m_0}\right) \left(\frac{k_{\parallel}}{m_{hh,\parallel}} + \frac{k_{\perp}}{m_{hh,\perp}}\right), \quad (1.25)$$

$$E_{lh}(k) = P_\epsilon - Q_\epsilon + \left(\frac{\hbar^2}{2m_0}\right) \left(\frac{k_{\parallel}}{m_{lh,\parallel}} + \frac{k_{\perp}}{m_{lh,\perp}}\right). \quad (1.26)$$

1.4 Envelope function approximation

We have treated only the ideal bulk so far. Now we introduce an additional potential $U(\mathbf{r})$ into the original Hamiltonian H_0 Eq. (1.1). This potential stands for e.g. impurities, donors, acceptors, the quantum well profile or magnetic² and electric field. We assume that $U(\mathbf{r})$ is a weak and slowly varying potential so that the perturbation theory can be applied. We may suppose that an additional non-periodic potential localizes the wave function and that's why the application of the delocalized periodic Bloch functions $\Psi_{n\mathbf{k}}(\mathbf{r})$ is not the best choice. More appropriate is to use the localized functions for a complete basis. These can be obtained by Fourier transformation of the Bloch functions, these are called the Wannier functions $a_n(\mathbf{r}, \mathbf{R}_i)$

$$a_n(\mathbf{r}, \mathbf{R}_i) = \frac{1}{\sqrt{N}} \sum_{\mathbf{k}} e^{-i\mathbf{k}\mathbf{R}_i} \Psi_{n\mathbf{k}}(\mathbf{r}), \quad (1.27)$$

$$\Psi_{n\mathbf{k}}(\mathbf{r}) = \frac{1}{\sqrt{N}} \sum_{\mathbf{R}_i} e^{i\mathbf{k}\mathbf{R}_i} a_n(\mathbf{r}, \mathbf{R}_i), \quad (1.28)$$

where N is the number of unit cells of the crystal³ and \mathbf{R}_i is a lattice vector. Since these functions are the eigenfunction of the lattice vector operator $\hat{\mathbf{R}}$

$$\hat{\mathbf{R}} a_n(\mathbf{r}, \mathbf{R}_i) = \mathbf{R}_i a_n(\mathbf{r}, \mathbf{R}_i), \quad (1.29)$$

²The vector potential $A(\mathbf{r})$ is meant here.

³Periodic (Born-Karmán) boundary conditions are assumed.

the application of this operator on the wave function

$$\psi(\mathbf{r}) = \sum_{n,\mathbf{k}} A_n(\mathbf{k}) \Psi_{n\mathbf{k}}(\mathbf{r}) \quad (1.30)$$

can be approximated by

$$\hat{\mathbf{R}}\psi(\mathbf{r}) \approx \sum_{n,\mathbf{k}} \left(i \frac{\partial}{\partial \mathbf{k}} A_n(\mathbf{k}) \right) \Psi_{n\mathbf{k}}(\mathbf{r}). \quad (1.31)$$

The equality is not found here since both \mathbf{k} and \mathbf{R} are discrete.

Having found this useful correspondence,

$$\mathbf{R} \leftrightarrow \left(i \frac{\partial}{\partial \mathbf{k}} \right) \quad \text{and} \quad \mathbf{k} \leftrightarrow \left(i \frac{\partial}{\partial \mathbf{R}} \right), \quad (1.32)$$

we may start to search for the solution of the Schrödinger equation in the form of

$$\psi(\mathbf{r}) = \frac{1}{\sqrt{N}} \sum_{n,i} \Phi_n(\mathbf{R}_i) a_n(\mathbf{r}, \mathbf{R}_i), \quad (1.33)$$

where $\Phi_n(\mathbf{R}_i)$ are *envelope functions*. Applying this ansatz in the Eq. (1.1) with additional $U(\mathbf{r})$ and multiplying with $a_m^*(\mathbf{r}, \mathbf{R}_j)$ on the lefthand side, the unperturbed part gives

$$\langle m, R_j | H_0 | n, R_i \rangle = \delta_{n,m} \delta_{i,j} E_n \left(i \frac{\partial}{\partial \mathbf{R}} \right), \quad (1.34)$$

where $E_n(\mathbf{k})$ is a dispersion relation of the n^{th} band. The second contribution can be approximated by

$$\langle m, R_j | U(\mathbf{r}) | n, R_i \rangle = \delta_{n,m} \delta_{i,j} U_n(\mathbf{R}). \quad (1.35)$$

The Schrödinger equation for the envelope functions can be thus written as

$$\left[E_n \left(i \frac{\partial}{\partial \mathbf{R}} \right) + U_n(\mathbf{R}) \right] \Phi_n(\mathbf{R}) = E \Phi_n(\mathbf{R}). \quad (1.36)$$

This approach is one of the mostly used in the theory of nanostructures since the Bloch functions (and consequently Wannier functions) of many semiconductors are almost identical. The values of the following matrix element

$$P = \frac{-i}{m_0} \langle S | p_x | X \rangle = \frac{-i}{m_0} \langle S | p_y | Y \rangle = \frac{-i}{m_0} \langle S | p_z | Z \rangle, \quad (1.37)$$

where S represents s -function, which are listed in Tab. 1.1, reveal it clearly. When combining different materials, the envelope function approximation is sufficient as the first approximation where $U_n(\mathbf{R})$ can be the position-dependent bandgap.

Table 1.1: Values of $E_p = 2m_0P^2$ in eV in some III-V materials, taken from [Bas92].

material	E_p (eV)
InP	17.00
InAs	21.11
InSb	22.49
GaAs	22.71
GaSb	22.88

1.5 Exciton in ideal bulk

Our approach has focused on the one-electron problem up to now, which is, of course, a very crude approximation since there are many electrons in a crystal. In order to deal with them the many body theory should be used: either Green's functions or density matrix approximation. Nevertheless, in some special cases the problem can be reduced substantially.

Let us assume that all valence bands are full, only one electron from the topmost one has been excited into the conduction band leaving a hole in the valence band. These two particles interact via Coulomb interaction and the Schrödinger equation for the electron-hole envelope function reads

$$\left(-\frac{\hbar^2}{2m_e} \frac{\partial}{\partial \mathbf{r}_e} - \frac{\hbar^2}{2m_h} \frac{\partial}{\partial \mathbf{r}_h} - \frac{e^2}{4\pi\epsilon_0\epsilon_S|\mathbf{r}_e - \mathbf{r}_h|} \right) \Phi(\mathbf{r}_e, \mathbf{r}_h) = E \Phi(\mathbf{r}_e, \mathbf{r}_h), \quad (1.38)$$

where subscript e stands for an electron in the conduction band and h is either heavy or light hole (if they are decoupled) in the valence band, ϵ_S is dielectric constant. This is a somewhat heuristic derivation but gives the same result as the density matrix approach in the Hartree-Fock approximation. The solution of the Eq. (1.38) is straightforward since it is exactly the hydrogen problem for the quasi-particle called *exciton*. Transforming coordinates to relative \mathbf{r} and center-of-mass \mathbf{R} ones

$$\mathbf{r} = \mathbf{r}_e - \mathbf{r}_h, \quad \mathbf{R} = \frac{\mathbf{r}_e m_e + \mathbf{r}_h m_h}{M}, \quad (1.39)$$

where $M = m_e + m_h$ is the total exciton mass, the Eq. (1.38) changes into

$$\left(-\frac{\hbar^2}{2M} \frac{\partial}{\partial \mathbf{R}} - \frac{\hbar^2}{2\mu} \frac{\partial}{\partial \mathbf{r}} - \frac{e^2}{4\pi\epsilon_0\epsilon_S r} \right) \Phi(\mathbf{r}, \mathbf{R}) = E \Phi(\mathbf{r}, \mathbf{R}), \quad (1.40)$$

where $\mu = m_e m_h / M$ is the reduced exciton mass. The wave function is written easily

$$\Phi_{\nu, \mathbf{K}}(\mathbf{r}, \mathbf{R}) = \frac{1}{\sqrt{\Omega}} e^{i\mathbf{K}\cdot\mathbf{R}} \phi_{\nu}(\mathbf{r}), \quad (1.41)$$

where Ω is a volume of the semiconductor and $\phi_\nu(\mathbf{r})$ is the solution of

$$\left(-\frac{\hbar^2}{2\mu} \frac{\partial}{\partial \mathbf{r}} - \frac{e^2}{4\pi\epsilon_0\epsilon_S r} \right) \phi_\nu(\mathbf{r}) = \xi_\nu \phi_\nu(\mathbf{r}), \quad (1.42)$$

which has the simple form for the ground state

$$\xi_{1s} = -\frac{\mu}{2} \left(\frac{e^2}{4\pi\epsilon_0\epsilon_S \hbar} \right)^2, \quad \phi_{1s} = \frac{1}{\sqrt{\pi a_0^3}} e^{-r/a_0}, \quad (1.43)$$

where

$$a_0 = \frac{\hbar^2 4\pi\epsilon_0\epsilon_S}{\mu e} \quad (1.44)$$

is the effective exciton Bohr radius. The details of the calculation of the ξ_ν and $\phi_\nu(\mathbf{r})$ of excited states can be found e.g. in Ref. [HK94]. The total exciton energy is

$$E_{\nu,K} = \frac{\hbar^2 K^2}{2M} + \xi_\nu. \quad (1.45)$$

The absorption coefficient $\alpha(\omega)$ which determines the decay of the light intensity per unit volume is related to the optical susceptibility $\chi(\omega)$ as

$$\alpha(\omega) = \frac{\omega}{n(\omega)} \text{Im}\chi(\omega), \quad (1.46)$$

where $n(\omega)$ is a refractive index of the semiconductor which is typically only weakly frequency dependent and the optical susceptibility describes the response of the dielectric medium on the applied electric field

$$\mathbf{P}(t) = \chi(\omega)\epsilon_0\mathbf{E}_\omega(t); \quad \mathbf{E}_\omega(t) = \mathbf{E}_0 e^{-i\omega t}. \quad (1.47)$$

The simple picture of the photon absorption near the bandgap energy is that an electron in the valence band is excited by the photon and the electron-hole pair is created. This pair under certain conditions⁴ forms an exciton which changes the absorption profile from the well-known square-root law in the bulk. Within the second quantization it can be shown that the induced

⁴The most important role plays the density of electron and holes, if too high then electron-hole plasma forms. The presented theory is valid in the limit of $n_{exc} a_B^3 \ll 1$ where n_{exc} is the exciton density. For higher densities (especially in the case of possible Bose-Einstein condensation of exciton) the exciton-exciton interaction $\sim n_{exc}^2$ cannot be neglected.

interband polarization per unit volume is the solution of the inhomogeneous Schrödinger equation [HK94]

$$\left[\hbar\omega + i0^+ - \hat{H}(\mathbf{r}_e, \mathbf{r}_h) \right] \mathbf{P}(\mathbf{r}_e, \mathbf{r}_h, \omega) = -d_{cv} \mathbf{E}_0 \delta(\mathbf{r}_e - \mathbf{r}_h), \quad (1.48)$$

where $\hat{H}(\mathbf{r}_e, \mathbf{r}_h)$ is electron-hole Hamiltonian for envelope functions and

$$d_{cv} = \langle c | \hat{\mathbf{d}} | v \rangle \quad (1.49)$$

is the interband dipole ($\hat{\mathbf{d}} = e\hat{\mathbf{x}}$) matrix element between conduction $|c\rangle$ and valence $|v\rangle$ band Bloch functions (see also Eq. (1.37)). The linear electron-hole susceptibility is then calculated from its definition Eq. (1.47) integrating the polarization $\mathbf{P}(\mathbf{r}_e, \mathbf{r}_h, t) = \mathbf{P}(\mathbf{r}_e, \mathbf{r}_h, \omega) e^{-i\omega t}$ over the volume Ω

$$\chi(\omega) = \frac{1}{\epsilon_0 |\mathbf{E}_0|} \int_{\Omega} d\mathbf{r} |\mathbf{P}(\mathbf{r}, \mathbf{r}, \omega)|. \quad (1.50)$$

This can be also expressed using the eigenvalues E_α and eigenvectors Φ_α of the Hamiltonian $\hat{H}(\mathbf{r}_e, \mathbf{r}_h)$ as

$$\chi(\omega) = |d_{cv}|^2 \sum_{\alpha} \frac{|\int_{\Omega} d\mathbf{r} \Phi_{\alpha}(\mathbf{r}, \mathbf{r})|^2}{\hbar\omega + i0^+ - E_{\alpha}}. \quad (1.51)$$

The knowledge of the solution of the Eq. (1.38) enables to rewrite Eq. (1.51) as

$$\chi(\omega) = |d_{cv}|^2 \sum_{\nu} \frac{|\phi_{\nu}(0)|^2}{\hbar\omega + i0^+ - \xi_{\nu} - E_g}, \quad (1.52)$$

where E_g is the bandgap energy. This can be calculated explicitly and Sommerfeld enhancement of the absorption coefficient is obtained (see e.g. the classical paper by Elliott [Eli57]).

The oscillator strength of individual exciton states α may be defined from the Eq. (1.51) as

$$M_{\alpha} = \int d\mathbf{r} \Phi_{\alpha}(\mathbf{r}_e = \mathbf{r}, \mathbf{r}_h = \mathbf{r}), \quad (1.53)$$

which has an intuitive interpretation: an exciton can be created (annihilated) only if the electron and the hole are found on the same spot. We define the optical density as

$$D(\omega) = \pi \sum_{\alpha} M_{\alpha}^2 \delta(\hbar\omega - E_{\alpha}), \quad (1.54)$$

which is proportional to $\text{Im}\chi(\omega)$. We will refer to $D(\omega)$ as to the absorption from now neglecting thus the constant prefactor d_{cv} and the factor ω in Eq. (1.46) which is almost constant and equal to E_g/\hbar .

Nevertheless, the quantity which is easily accessible in the experiment is photoluminescence (PL). This is similar to the absorption but the occupation N_α of a state α is not constant for all states but has some distribution, it would be Maxwell-Boltzmann distribution in a thermal equilibrium, and is defined as

$$P(\omega) = \pi \sum_{\alpha} M_{\alpha}^2 N_{\alpha} \delta(\hbar\omega - E_{\alpha}). \quad (1.55)$$

In general, the calculation of the occupation function is a demanding task since the interaction between excitons or better electron-hole plasma and optical and acoustic phonons have to be taken into account.

1.6 Exciton in ideal quantum well in zero magnetic field

As has been already mentioned in the introduction the idea of combining two materials in such a way that a thin slab of small bandgap material A is sandwiched between large bandgap material B, has turned out to be extremely fruitful. The motivation behind is to confine the carriers in the thin slab in order to increase their mobility.

Here the envelope function formalism comes into play: the difference between bandgaps of both material divided between electron and hole⁵ can be interpreted as the slowly varying potential $U(\mathbf{R})$

$$U_a(\mathbf{R}) = (E_{g,B} - E_{g,A}) f_a \theta_B(\mathbf{R}), \quad (1.56)$$

where a stands for either electron or hole, $E_{g,B(A)}$ is bandgap of material B (A), f_a is bandgap ratio ($f_e + f_h = 1$), and $\theta_B(\mathbf{R})$ is the Heavyside function which is unity in material B.

The exciton Hamiltonian for the envelope function can be formulated using the results of previous sections

$$H_{exc} = H_e(\mathbf{r}_e) + H_h(\mathbf{r}_h) - \frac{e^2}{4\pi\epsilon_0\epsilon_S|\mathbf{r}_e - \mathbf{r}_h|}, \quad (1.57)$$

⁵The most widely used theoretical model is the electron affinity rule which calculates the conduction band discontinuity ΔE_c as the difference between electron affinities of the two semiconductors. The valence band discontinuity is then found from the relation $\Delta E_g = \Delta E_c + \Delta E_v$ [Ada94].

where the electron and hole Hamiltonians are generalized compared to the Eq. (1.38). The conduction band modification due to the strain has to be included

$$H_e(\mathbf{r}_e) = -\frac{\hbar^2}{2m_e} \frac{\partial}{\partial \mathbf{r}_e} + a_c(\epsilon_{xx} + \epsilon_{yy} + \epsilon_{zz}) + U_e(\mathbf{r}_e), \quad (1.58)$$

where a_c is conduction band deformation potential. Moreover, taking into account the energy dispersion of the topmost valence bands Eq. (1.15) and applying the rule for the envelope function Eq. (1.36) the hole Hamiltonian may be written as

$$H_h(\mathbf{r}_h) = H_v \left(i \frac{\partial}{\partial \mathbf{r}_h} \right) + U_h(\mathbf{r}_h) \mathbf{I}, \quad (1.59)$$

where \mathbf{I} is the identity matrix. The matrix $H_v(\mathbf{k})$ neglecting spin-orbit band and replacing γ_i (a, b, d) with $-\gamma_i$ ($-a, -b, -d$) has the form of

$$H_v(\mathbf{k}) = \begin{bmatrix} P+Q & -S & R & 0 \\ -S^\dagger & P-Q & 0 & R \\ R^\dagger & 0 & P-Q & S \\ 0 & R^\dagger & S^\dagger & P+Q \end{bmatrix}. \quad (1.60)$$

The solution of the Schrödinger equation with exciton Hamiltonian Eq. (1.57) is possible only numerically and is rather demanding [SRZ00].

Nevertheless, justified simplifications are possible. First, since we restrict ourselves only to the vicinity of the Γ point where the heavy and light hole decoupling Eq. (1.25) is valid, the hole part of the Hamiltonian Eq. (1.57) decouples into two diagonal terms

$$H_{hh} = P_\epsilon(\mathbf{r}_h) + Q_\epsilon(\mathbf{r}_h) - \left(\frac{\hbar^2}{2m_{hh,\parallel}} \frac{\partial^2}{\partial \mathbf{r}_h^2} + \frac{\hbar^2}{2m_{hh,\perp}} \frac{\partial^2}{\partial z_h^2} \right) + U_h(\mathbf{r}_h, z_h), \quad (1.61)$$

$$H_{lh} = P_\epsilon(\mathbf{r}_h) - Q_\epsilon(\mathbf{r}_h) - \left(\frac{\hbar^2}{2m_{lh,\parallel}} \frac{\partial^2}{\partial \mathbf{r}_h^2} + \frac{\hbar^2}{2m_{lh,\perp}} \frac{\partial^2}{\partial z_h^2} \right) + U_h(\mathbf{r}_h, z_h), \quad (1.62)$$

where \mathbf{r}_a is two-dimensional vector in the xy -plane from now. This means that there are two kinds of excitons: heavy and light hole excitons.

Second, we assume that (i) the confining potential $U_a(\mathbf{r}_a, z_a)$ is only function of z_a and (ii) the potential is strong enough that the expansion of the total wave function

$$\Phi(\mathbf{r}_e, \mathbf{r}_h, z_e, z_h) = \sum_{\mu, \nu} \Psi_{\mu, \nu}(\mathbf{r}_e, \mathbf{r}_h) v_{e, \mu}(z_e) v_{h, \nu}(z_h) \quad (1.63)$$

can be limited only to the ground state functions $v_{a,0}(z_a)$ and thus the one-particle motion in the z -direction and in the xy -plane can be separated (omitting the subscript 0)

$$\Phi(\mathbf{r}_e, \mathbf{r}_h, z_e, z_h) = \Psi(\mathbf{r}_e, \mathbf{r}_h) v_e(z_e) v_h(z_h), \quad (1.64)$$

where the confinement wave functions satisfy

$$\left(-\frac{\hbar^2}{2m_{a,\perp}} \frac{\partial^2}{\partial z_a^2} + U_a(z_a) \right) v_a(z_a) = E_{C,a} v_a(z_a), \quad (1.65)$$

and where heavy and light hole is comprised in h and $E_{C,a}$ is the confinement energy. This is the well-known single sublevel approximation. If the mass $m_{a,\perp}$ was a function of z then the kinetic term in Eq. (1.65) would not be a hermitian operator. There are several possibilities how to write the operator $\frac{1}{m_{a,\perp}} \frac{\partial^2}{\partial z_a^2}$ in a hermitian way. The requirement that the operator is hermitian and homogeneous is satisfied by

$$m_{a,\perp}^{(\beta-1)/2}(z) \frac{\partial}{\partial z_a} m_{a,\perp}^{-\beta}(z) \frac{\partial}{\partial z_a} m_{a,\perp}^{(\beta-1)/2}(z), \quad (1.66)$$

which implies the continuity conditions:

$$m_{a,\perp}^{(\beta-1)/2}(z) v_a(z_a), \quad \text{and} \quad m_{a,\perp}^{(-\beta-1)/2}(z) \frac{\partial}{\partial z_a} v_a(z_a). \quad (1.67)$$

Only the choice of $\beta = 1$ gives the continuous density of probability $|v_a(z_a)|^2$, which is the most used variant in the literature and is called Ben Daniel-Duke model [Bas92]

$$\frac{1}{m_{a,\perp}} \frac{\partial^2}{\partial z_a^2} \rightarrow \frac{\partial}{\partial z_a} \frac{1}{m_{a,\perp}(z)} \frac{\partial}{\partial z_a}. \quad (1.68)$$

This allows to write down the exciton Hamiltonian in the compact way

$$\hat{H} = \sum_{a=e,h} \left(-\frac{\hbar^2}{2m_{a,\parallel}} \Delta_{\mathbf{r},a} - \frac{\partial}{\partial z_a} \frac{\hbar^2}{m_{a,\perp}(z)} \frac{\partial}{\partial z_a} + U_a(z_a) \right) - \frac{e^2}{4\pi\epsilon_0\epsilon_S \sqrt{(\mathbf{r}_e - \mathbf{r}_h)^2 + (z_e - z_h)^2}}, \quad (1.69)$$

where the dependence of the in-plane mass $m_{a,\parallel}$ on z was neglected.⁶ Separating the motion in the z -direction Eq. (1.65), the xy -plane Hamiltonian

⁶Due to the confinement taking just the effective mass of the quantum well material is a very good approximation.

reads

$$\hat{H} = - \sum_{a=e,h} \frac{\hbar^2}{2m_{a,\parallel}} \Delta_{\mathbf{r},a} - V_C(\mathbf{r}_e - \mathbf{r}_h), \quad (1.70)$$

where V_C is the averaged Coulomb potential

$$V_C(\mathbf{r}) = \int dz_e dz_h v_e^2(z_e) v_h^2(z_h) \frac{e^2}{4\pi\epsilon_0\epsilon_S \sqrt{\mathbf{r}^2 + (z_e - z_h)^2}}. \quad (1.71)$$

Even though the effective mass of the lowest conduction band is a scalar, we distinguish between $m_{e,\perp}$ and $m_{e,\parallel}$ since the quartic correction of the dispersion relation plays a role due to the confinement as we will see in Sec. 1.8. Eq. (1.65) should also contain strain dependent terms but we suppose that the confinement $U_a(z_a)$ is dominant (which is not obvious).

Moreover, it has been assumed so far that the static dielectric constant ϵ_S is the same in the barrier ϵ_S^b and in the well ϵ_S^w , which is not generally true. In order to take it into account the Poisson equation has to be solved first, which is usually done with the help of image charges. Nevertheless, if the difference $\epsilon_S^b - \epsilon_S^w$ is small (as in the case of GaAs/AlGaAs) then the exciton binding energy changes negligibly [TTZGB90; WH91].

1.7 Exciton in ideal quantum well in non-zero magnetic field

Let us continue including a perpendicular magnetic field $\mathbf{B} = B\mathbf{e}_z$ ⁷ into the Hamiltonian Eq. (1.69) which is modified to

$$\begin{aligned} \hat{H} = & \sum_{a=e,h} \left(\frac{1}{2m_{a,\parallel}} \left[-i\hbar \frac{d}{d\mathbf{r}_a} - eq_a \mathbf{A}(\mathbf{r}_a, z_a) \right]^2 - \frac{\hbar^2}{2} \frac{d}{dz_a} \frac{1}{m_{a,\perp}(z_a)} \frac{d}{dz_a} \right. \\ & \left. + U_a(z_a) \right) + (g_e^* \mu_B B \sigma_e^z - g_h^* \mu_B B \sigma_h^z) - \sum_{i=x,y,z} c_i \sigma_e^i \sigma_h^i \\ & - \frac{e^2}{4\pi\epsilon_0\epsilon_S \sqrt{(\mathbf{r}_e - \mathbf{r}_h)^2 + (z_e - z_h)^2}}, \end{aligned} \quad (1.72)$$

where $\mathbf{A}(\mathbf{r}, z)$ is the vector potential which is related to the magnetic field as

$$\mathbf{B} = \nabla \times \mathbf{A}(\mathbf{r}, z), \quad (1.73)$$

⁷Precisely, B is magnetic induction and H is the magnetic field. They are related in linear materials as $B = \mu H$ where μ is the magnetic permeability.

and one possible choice is e. g. $\mathbf{A}(\mathbf{r}, z) = \frac{B}{2}(-y, x, 0)$. The prefactor q_a gives the sign of the charge: positive (negative) for hole (electron), g_a^* are effective g -factors for electron and hole, μ_B is the Bohr magneton, σ^z is the Pauli spin matrix, and c_i is the coupling constant which represents the short-range electron hole exchange interaction and is a function of the quantum well width [BSH⁺94].

1.7.1 General properties

Here we investigate general properties of an exciton under an applied homogeneous magnetic field going beyond the variational arguments for the ground state presented in Ref. [WR98].

First, the Hamiltonian Eq. (1.72) is rewritten dropping spin-dependent parts as

$$\hat{H} = \sum_{a=e,h} \frac{1}{2m_a} (\hat{p}_a - q_a e \mathbf{A}_a(r_e, r_h))^2 + \mathbf{V}(r_e, r_h), \quad (1.74)$$

where r_a is a three-dimensional vector, $\hat{p}_a = -i\hbar\nabla_a$ is the momentum operator, and the spatial dependence of masses is neglected for simplicity. The two-particle potential $\mathbf{V}(r_e, r_h)$ includes the Coulomb interaction, disorder, and lateral confinement. $\mathbf{A}_a(r_e, r_h)$ is the vector potential in an arbitrary two-particle gauge linear in B where the second coordinate (e.g. r_h in the case of electron) can be regarded as a parameter. The magnetic field is obtained as before via

$$\mathbf{B} = \nabla_e \times \mathbf{A}_e(r_e, r_h) = \nabla_h \times \mathbf{A}_h(r_e, r_h). \quad (1.75)$$

A general gauge transformation reads⁸

$$\check{\mathbf{A}}_a(r_e, r_h) = \mathbf{A}_a(r_e, r_h) + q_a \frac{\hbar}{e} \nabla_a \lambda(r_e, r_h) \quad (1.76)$$

with an arbitrary two-particle function $\lambda(r_e, r_h)$. Consequently, the wave function is transformed as

$$\check{\Psi}(r_e, r_h) = e^{i\lambda(r_e, r_h)} \Psi(r_e, r_h). \quad (1.77)$$

⁸In order to become more familiar with a two-particle gauge $\mathbf{A}_a(r_e, r_h)$ one can start with the one-particle one $\mathbf{A}(r)$. Changing the gauge using Eqs. (1.76) one sees immediately that Eq. (1.75) is fulfilled.

Next, the Hamiltonian terms can be sorted according to powers of B

$$H_0 = \sum_{a=e,h} \frac{\hat{p}_a^2}{2m_a} + \mathcal{V}(r_e, r_h), \quad (1.78)$$

$$H_1 = \sum_{a=e,h} \frac{1}{2m_a} [\hat{p}_a, q_a e \mathbf{A}_a(r_e, r_h)]_+, \quad (1.79)$$

$$H_2 = \sum_{a=e,h} \frac{1}{2m_a} e^2 \mathbf{A}_a^2(r_e, r_h), \quad (1.80)$$

where $[\hat{A}, \hat{B}]_+ = \hat{A}\hat{B} + \hat{B}\hat{A}$ is the anticommutator, H_1 is purely imaginary and linear in B , and H_2 is non-negative and quadratic in B .

Second, our aim is to derive a general statement on the B -dependence of the exciton ground state energy $E_0(B)$. Let us separate the wave function of the ground state into amplitude and phase⁹

$$\Psi_0(r_e, r_h) = e^{i\xi_0(r_e, r_h)} \chi_0(r_e, r_h), \quad (1.81)$$

where both $\xi_0(r_e, r_h)$ and $\chi_0(r_e, r_h)$ are real and well-behaved continuous functions. According to Eq. (1.77), this corresponds to a special gauge transformation. Redefining the Hamiltonian parts Eqs. (1.79) and (1.80) as

$$\hat{H}_1^{\xi_0} = \sum_{a=e,h} \frac{1}{2m_a} [\hat{p}_a, \{q_a e \mathbf{A}_a(r_e, r_h) + \hat{p}_a i \xi_0(r_e, r_h)\}]_+, \quad (1.82)$$

$$\hat{H}_2^{\xi_0} = \sum_{a=e,h} \frac{1}{2m_a} \{q_a e \mathbf{A}_a(r_e, r_h) + \hat{p}_a i \xi_0(r_e, r_h)\}^2, \quad (1.83)$$

the Schrödinger equations for the imaginary and real part read

$$\hat{H}_1^{\xi_0} |\chi_0(r_e, r_h)\rangle = 0, \quad (1.84)$$

$$\left(H_0 + \hat{H}_2^{\xi_0} \right) |\chi_0(r_e, r_h)\rangle = E_0(B) |\chi_0(r_e, r_h)\rangle. \quad (1.85)$$

Next, the expectation value of Eq. (1.85) is formed

$$E_0(B) = \langle \chi_0 | H_0 | \chi_0 \rangle + \langle \chi_0 | \hat{H}_2^{\xi_0} | \chi_0 \rangle. \quad (1.86)$$

Applying variational arguments the inequality $\langle \chi_0 | H_0 | \chi_0 \rangle \geq E_0(0)$ holds where $E_0(0)$ is the ground state energy at $B = 0$ T. Since the second term

⁹We thank E. A. Muljarov for pointing out the usefulness of such a separation. Nevertheless, the necessary analytic behavior of $\xi_0(r_e, r_h)$ for $B \rightarrow 0$ holds only for the ground state in general. Details go beyond the scope of this work.

gives always a positive contribution, we have derived a lower boundary for the ground state for any magnetic field,

$$E_0(B) \geq E_0(0). \quad (1.87)$$

Further, the general property of the Hamiltonian $H(B) = H^*(-B)$ implies

$$\Psi_\alpha(B) = \Psi_\alpha^*(-B) + 2\pi n(r_e, r_h), \quad (1.88)$$

where $n(r_e, r_h)$ is function having only integer values. This leads to the following expansion of the phase and the amplitude for the ground state for which $n(r_e, r_h)$ is identically zero

$$\begin{aligned} \xi_0(r_e, r_h) &= \sum_{i=2k+1}^{\infty} B^i \xi_0^{(i)}(r_e, r_h), \quad (1.89) \\ \chi_0(r_e, r_h) &= \sum_{i=2k}^{\infty} B^i \chi_0^{(i)}(r_e, r_h) \quad k \text{ being non-negative integer.} \quad (1.90) \end{aligned}$$

Now, adopting perturbation theory for non-degenerate states¹⁰, the zeroth order in B of Eq. (1.85) gives $H_0 \xi_0^{(0)} = E_0(0) \xi_0^{(0)}$, the first order is zero, and the second one gives

$$(H_0 - E_0(0))|\chi_0^{(2)}\rangle + (\hat{H}_2^{\xi_0} - E_0^{(2)})|\chi_0^{(0)}\rangle = 0, \quad (1.91)$$

where only the first term of the phase $\xi_0^{(1)}$ is considered in $\hat{H}_2^{\xi_0}$. Multiplying this equation from left with $\langle \chi_0^{(0)} |$ the perturbed eigenenergy may be written as

$$E_0(B) = E_0(0) + \gamma_{2,0} B^2, \quad (1.92)$$

where the diamagnetic shift coefficient of the ground state has been introduced ($\tilde{\mathbf{A}}_a(r_e, r_h) = \mathbf{A}_a(r_e, r_h)/B$)

$$\gamma_{2,0} = \left\langle \chi_0^{(0)} \left| \sum_{a=e,h} \frac{1}{2m_a} \left(q_a \tilde{\mathbf{A}}_a(r_e, r_h) + \hat{p}_a i \xi_0^{(1)}(r_e, r_h) \right)^2 \right| \chi_0^{(0)} \right\rangle, \quad (1.93)$$

which is by construction a non-negative quantity.

Therefore, in order to obtain the value of the diamagnetic shift coefficient the knowledge of the wave function at $B = 0$ T is generally *not* sufficient and

¹⁰Assuming thus that the potential $V(r_e, r_h)$ plays a dominant role, which excludes e. g. highly degenerate free-electron Landau levels.

additionally Eq. (1.84) has to be solved. This is equivalent to the solution of the Schrödinger equation with the Hamiltonian Eq. (1.74) for small B .

Generally, the diamagnetic coefficients of the state α are defined as

$$\gamma_{1,\alpha} = \lim_{B \rightarrow 0} \frac{dE_\alpha(B)}{dB} \quad (1.94)$$

$$\gamma_{2,\alpha} = \lim_{B \rightarrow 0} \frac{1}{2} \frac{d^2 E_\alpha(B)}{dB^2}, \quad (1.95)$$

and may have positive or negative values for excited states. However, due to the reality of the wave function belonging to non-degenerate states their linear term is zero. In the case of degenerate states at $B = 0$ T, the degeneracy can be lifted at $B \neq 0$ T as easily follows from perturbation theory and consequently, a linear term in B may appear.

It should be noticed that these theorems are generally valid for any *many particle state*. This can be shown adopting the same steps but changing arguments $(r_e, r_h) \rightarrow (r_1 \dots r_i \dots r_N)$.

1.7.2 Optical activity

Let us now concentrate on the optical activity of different exciton states.

First, the total angular momentum J of the Bloch function has to be considered: $J = 1/2$ for electrons (see Sec. 1.1), $J = 3/2$, $J_z = \pm 3/2$ for heavy, and $J = 3/2$, $J_z = \pm 1/2$ for light holes (see Eq. (1.14)). Selection rules imply that only dipole matrix element Eq. (1.49) between states with difference in the total angular momentum $\Delta J = 1$ are non-zero. Two kinds of excitons (apart from heavy and light ones) can be distinguished: optically active (bright) ones with $J_{exc} = 1$ and non-optically active (dark) ones with $J_{exc} = 2$.

Second, although the spin-orbit coupling is neglected spin degrees of freedom can be factorized only in the case of heavy hole Eq. (1.14). Nevertheless, this is relevant for us as we will see in the next Chapter. Thus regarding the spin four different exciton states with $J_{exc} = 1$ can be distinguished $|\sigma_e^z \sigma_h^z\rangle$

$$\begin{aligned} |\chi_1\rangle &= \left| \frac{1}{2}, -\frac{1}{2} \right\rangle, & |\chi_2\rangle &= \left| -\frac{1}{2}, \frac{1}{2} \right\rangle, \\ |\chi_3\rangle &= \left| \frac{1}{2}, \frac{1}{2} \right\rangle, & |\chi_4\rangle &= \left| -\frac{1}{2}, -\frac{1}{2} \right\rangle. \end{aligned} \quad (1.96)$$

In zero magnetic field these states are energetically separated by the electron-hole exchange interaction into two doublets $\chi_{1,2}$ and $\chi_{3,4}$ in which spins are

antiparallel and parallel. Optically active are only states $\chi_{1,2}$ because the following selection rule applies

$$\sigma_{exc}^z = \sigma_e^z + \sigma_h^z = 0. \quad (1.97)$$

They emit circularly polarized light σ^+ and σ^- in the z -direction. In non-zero magnetic field both doublets are further splitted

$$\Delta_{12} = |g_e^* + g_h^*| \mu_B B, \quad \Delta_{34} = |g_e^* - g_h^*| \mu_B B, \quad (1.98)$$

and an effective exciton g -factor of optically active states can be defined [SBMH92]

$$g_{exc} = g_e^* + g_h^*. \quad (1.99)$$

In the following only (heavy hole) excitons with $J_{exc} = 1$ and spin component $\chi_{1,2}$ are treated. The oscillator strength Eq. (1.53) within the approximation Eq. (1.64) takes the form of

$$M_\alpha = \int d\mathbf{r} \Psi_\alpha(\mathbf{r}, \mathbf{r}) \int dz v_e(z) v_h(z), \quad (1.100)$$

since the second part is state independent (gives only prefactor), we concentrate on the first part when dealing with quantum wells.

1.8 Electron effective mass enhancement

The change of the electron effective mass due to the confinement (e. g. in quantum wells) has been investigated in detail by Ekenberg [Eke89]. We follow his ideas.

It turns out to be necessary to go beyond the quadratic dispersion of the conduction band in order to study the influence of the confinement on the dispersion relation. Thus, it follows from the symmetry arguments that a dispersion relation of the lowest conduction band in the point Γ in the bulk up to the fourth order reads

$$E(\mathbf{k}) = \frac{\hbar^2}{2m} k^2 + \alpha_0 k^4 + \beta_0 (k_x^2 k_y^2 + k_y^2 k_x^2 + k_z^2 k_x^2) \pm \gamma_0 [k^2 (k_x^2 k_y^2 + k_y^2 k_x^2 + k_z^2 k_x^2) - 9k_x^2 k_y^2 k_z^2]^{1/2}, \quad (1.101)$$

where m is the effective mass in material and α_0 , β_0 , and γ_0 are coefficients which can be determined from $\mathbf{k} \cdot \mathbf{p}$ calculation. The last term describes the spin-splitting due to the lack of inversion symmetry in III-V semiconductors.

In order to calculate new confinement energies, the kinetic operator in Eq. (1.65) has to be modified. Assuming translational symmetry in the xy -plane the ground state energy is found if $k_x = k_y = 0$ and according to Eq. (1.32) kinetic energy operator changes to

$$-\frac{\hbar^2}{2m} \frac{\partial^2}{\partial dz_a^2} \rightarrow -\frac{\hbar^2}{2m} \frac{\partial^2}{\partial dz_a^2} + \alpha_0 \frac{\partial^4}{\partial dz_a^4}. \quad (1.102)$$

Let us look on this from a different angle. The relation between confinement energy E_c and quasi-momentum K

$$E_c = \frac{\hbar^2}{2m} K^2 + \alpha_0 K^4 \quad (1.103)$$

can be easily inverted to

$$K = \left(\frac{m}{\alpha' \hbar^2} [1 - (1 - 4\alpha' E_c)^{1/2}] \right)^{1/2}, \quad \alpha' \equiv -\frac{2m}{\hbar^2} \alpha_0. \quad (1.104)$$

Comparing this with the parabolic case $K = \sqrt{2m_\perp E_c / \hbar^2}$ the idea is, instead of applying Eq. (1.102), to adopt the standard kinetic operator but with enhanced effective mass which takes the form of

$$m_\perp(E_c) = \frac{m}{2\alpha' E_c} [1 - (1 - 4\alpha' E_c)^{1/2}]. \quad (1.105)$$

This mass cannot be measured, it has been only introduced to obtain the correct confinement energy.

The enhancement of the parallel mass is more intuitive since the confinement energy fixes the value of $k_z = K$, which changes the in-plane dispersion relation to

$$E_\parallel(\mathbf{k}_\parallel) = \left(\frac{\hbar^2}{2m} + (2\alpha_0 + \beta_0) K^2 \right) k_\parallel^2. \quad (1.106)$$

Performing the second derivative with respect to the quasi-momentum k_\parallel the effective mass is enhanced as

$$m_\parallel(E_c) = m[1 + (2\alpha' + \beta') E_c], \quad \beta' \equiv -\frac{2m}{\hbar^2} \beta_0. \quad (1.107)$$

The mass enhancement which is usually a few percent can be experimentally confirmed only in special cases, mainly if a magnetic field is present as it is demonstrated in the next Chapter.

1.9 Strain

Finally, since the strain plays an important role in many materials it should be calculated and included in the Hamiltonian Eqs. (1.61) and (1.62). Although what is presented in this Section is not directly related to the semiconductor theory and it is almost only classical mechanics, due to its validity it is widely used in the numerical simulation of the semiconductor properties.

1.9.1 Basics

We start with the general definition of the strain tensor in the limit of the small deformation and linear elasticity

$$\epsilon_{ij} = \frac{1}{2} \left(\frac{\partial u_i}{\partial x_j} + \frac{\partial u_j}{\partial x_i} \right), \quad (1.108)$$

where u_i is a displacement from the equilibrium position. The relation between deformation energy (or better free energy F) density per unit volume and strain can be found following the analogy with the harmonic oscillator¹¹

$$\mathcal{E} = \frac{1}{2} \sum_{ijkl} C_{ijkl} \epsilon_{ij} \epsilon_{kl}, \quad (1.109)$$

where C_{ijkl} is a tensor of elastic constants which has 21 independent entries. This number is drastically reduced if the symmetry is increased, e. g. in the case of the cubic symmetry there are only three independent constants¹²

$$\begin{aligned} C_{11} &= C_{xxxx} = C_{yyyy} = C_{zzzz}, \\ C_{12} &= C_{xxyy} = C_{yyzz} = C_{zzxx}, \\ C_{44} &= C_{xyxy} = C_{yzyz} = C_{zxzx}. \end{aligned} \quad (1.110)$$

If the isotropic medium is taken into account the Eq. (1.109) can be simplified to

$$\mathcal{E} = \frac{1}{2} \sum_{ij} \left(2\mu \epsilon_{ij} + \lambda \delta_{ij} \sum_i \epsilon_{ii} \right) \epsilon_{ij}, \quad (1.111)$$

¹¹In order to see it the stress tensor (force per area) is defined as $\sigma_{ij} = \sum_{kl} C_{ijkl} \epsilon_{kl}$. Since the force of the harmonic oscillator is defined as $F = kx$ and the energy as $E = \frac{1}{2} kx^2$ the same arguments may be used to derive Eq. (1.109).

¹²The Voigt notation, reducing four indices to two according to the following key: 1 \equiv xx , 2 \equiv yy , 3 \equiv zz , 4 \equiv yz , 5 \equiv xz , and 6 \equiv xy , has been introduced.

where λ and μ are Lamè constants. The relations between these and elastic constants Eq. (1.110) can be found easily

$$C_{11} = 2\mu + \lambda, \quad C_{12} = \lambda, \quad C_{44} = \mu, \quad (1.112)$$

which reveals a relation between elastic constants for the isotropic medium¹³

$$C_{11} - C_{12} - 2C_{44} = 0. \quad (1.113)$$

The Lamè and elastic constants can be related to the other well-known constant: Poisson ratio¹⁴ ν which gives the ratio of the relative contraction strain, or transverse strain (normal to the applied load), divided by the relative extension strain

$$\nu = \frac{\lambda}{2(\mu + \lambda)} = \frac{C_{12}}{C_{11} + C_{12}}. \quad (1.114)$$

1.9.2 Isotropic elasticity

The calculation of the strain profile in the nanostructures is not an easy task in general. Different approaches have been developed to calculate the strain profile. There are atomistic models like valence force field [Kea66] with phenomenological expressions for the elastic energy which depends on atomic coordinates and two empirical parameters which are easily derived from the experimental elastic constants. Another approach is to apply continuum mechanics: the functional form of the elastic energy is minimized to obtain the distribution of the displacement in the structure and consequently the strain.

Let us assume that there is a object O of an arbitrary shape made up from material A inside material B. These two materials have different lattice constants ($\lambda_A > \lambda_B$) which leads to the misfit strain $\epsilon_\lambda = (\lambda_A - \lambda_B)/\lambda_B$. Due to this misfit there is a hydrostatic pressure which tries to reduce the lattice constant of material A. Thus, the strain may be decomposed into two parts

$$\epsilon_{ij}(\mathbf{r}) = -\delta_{ij}\epsilon_\lambda\theta(\mathbf{r} \in O) + \tilde{\epsilon}_{ij}(\mathbf{r}), \quad (1.115)$$

¹³Such a relation can be also derived directly from the Eq. (1.109) taking into account infinitesimal rotation which does not change this expression.

¹⁴Another well-known constant is the Young modulus which is defined as the ratio, for small strains, of the rate of change of stress σ with strain ϵ and can be expressed as $Y = \frac{\mu(2\mu+3\lambda)}{2\mu+3\lambda}$.

where $\tilde{\epsilon}_{ij}$ describes an unknown relaxation of the medium upon the applied pressure. Substituting Eq. (1.115) into the Eq. (1.109) and integrating over volume the elastic energy takes form of (omitting tilde from now)

$$E_{el} = \int_V dV \left[\frac{1}{2} C_{11} (\epsilon_{xx}^2 + \epsilon_{yy}^2 + \epsilon_{zz}^2) + C_{12} (\epsilon_{xx}\epsilon_{yy} + \epsilon_{yy}\epsilon_{zz} + \epsilon_{zz}\epsilon_{xx}) \right. \\ \left. + 2C_{44} (\epsilon_{xy}^2 + \epsilon_{yz}^2 + \epsilon_{zx}^2) - 2\alpha (\epsilon_{xx} + \epsilon_{yy} + \epsilon_{zz}) \epsilon_\lambda + 3\alpha \epsilon_\lambda^2 \right], \quad (1.116)$$

where V is equilibrium volume and $\alpha = C_{11}/2 + C_{12}$. The elastic energy is minimized with respect to the displacement

$$\frac{dE_{el}}{du_x} = \frac{dE_{el}}{du_y} = \frac{dE_{el}}{du_z} = 0, \quad (1.117)$$

which has to be solved numerically.

Recently, an efficient method to calculate the strain distribution in an isotropic and homogeneous material has been proposed [Dav98]. The equation of equilibrium can be derived for the displacement $\mathbf{u}(\mathbf{r})$ taking into account Newton's laws, which for an isotropic medium has a compact form of [LL59]¹⁵

$$\frac{3(1-\nu)}{1+\nu} \nabla \nabla \cdot \mathbf{u} - \frac{3(1-2\nu)}{2(1+\nu)} \nabla \times \nabla \times \mathbf{u} = \alpha_T \nabla \mathbf{T}, \quad (1.118)$$

where α_T is the thermal expansion coefficient and \mathbf{T} is a vector of temperature. Here the trick can be used, instead of assuming any temperature gradient we take as a source term the volume change due to the misfit strain $\alpha_T \mathbf{T} = 3\epsilon_\lambda(\mathbf{r}) \equiv 3\epsilon_\lambda \theta(\mathbf{r} \in O)$. We look for the solution which fulfills $\nabla \times \mathbf{u} = 0$ and

$$\nabla \cdot \mathbf{u}(\mathbf{r}) = \frac{1+\nu}{1-\nu} \epsilon_\lambda(\mathbf{r}), \quad (1.119)$$

which can be found integrating over volume¹⁶

$$\mathbf{u}(\mathbf{r}) = \frac{1}{4\pi} \frac{1+\nu}{1-\nu} \nabla \int_O \frac{\epsilon_\lambda(\mathbf{r}')}{|\mathbf{r}-\mathbf{r}'|} dV'. \quad (1.120)$$

¹⁵The equations of equilibrium disregarding gravity are $\frac{\partial \sigma_{ij}}{\partial x_j} = 0$ which can be further treated using $\sigma_{ij} = 2\mu \epsilon_{ij} + \lambda \delta_{ij} \sum_i \epsilon_{ii}$ and identities of vector analysis. The thermal contribution can be added expanding the free energy $F(T) = F(T_0) - K \alpha_T (T - T_0) \sum_i \epsilon_{ii}$, where $K = \lambda + 2/3\mu$, and adopting $\sigma_{ij} = \frac{\partial F}{\partial \epsilon_{ij}}$

¹⁶Introducing Lamè potential $\mathbf{u} = \nabla \chi$ the Poisson equation is found $\Delta \chi(\mathbf{r}) = \frac{1+\nu}{1-\nu} \epsilon_\lambda(\mathbf{r})$ whose solution $\chi(\mathbf{r}) = \frac{1}{4\pi} \frac{1+\nu}{1-\nu} \int_O \frac{\epsilon_\lambda(\mathbf{r}')}{|\mathbf{r}-\mathbf{r}'|} dV'$ is well-known from the electrostatics.

By using the Gauss divergence theorem the strain coming from the relaxation under applied pressure has the form of

$$\epsilon_{ij}(\mathbf{r}) = -\frac{\epsilon_\lambda}{4\pi} \frac{1+\nu}{1-\nu} \oint_{S'} \frac{(x_i - x'_i) dS'_j}{|\mathbf{r} - \mathbf{r}'|^3}, \quad (1.121)$$

where S' is the surface of the object O . The total strain Eq. (1.115) is thus

$$\epsilon_{ij}(\mathbf{r}) = -\delta_{ij} \epsilon_\lambda \theta(\mathbf{r} \in O) - \frac{\epsilon_\lambda}{4\pi} \frac{1+\nu}{1-\nu} \oint_{S'} \frac{(x_i - x'_i) dS'_j}{|\mathbf{r} - \mathbf{r}'|^3}. \quad (1.122)$$

If the elastic constants satisfy Eq. (1.113) then the strain distribution for the isotropic crystal is reproduced by the continuum elasticity. We have assumed so far that the Poisson ratio ν is identical in both materials A and B, which is not generally true. The conditions for the displacement vector \mathbf{u} on the interface between materials A and B follow from the Eq. (1.119) and with direct analogy with electrostatics¹⁷ we obtain

$$\begin{aligned} u_{A,n} \frac{1-\nu_A}{1+\nu_A} &= u_{B,n} \frac{1-\nu_B}{1+\nu_B}, \\ u_{A,t} &= u_{B,t}, \end{aligned} \quad (1.123)$$

where $u_{n(t)}$ is the normal (tangential) component of the \mathbf{u} to the interface.

There are several works comparing the quality of different approaches [TPJ⁺02; JPP03]. It turns out that despite its simplicity the isotropic elasticity gives results which are comparable with more elaborate approaches. From this reason we adopt this method to calculate the strain profile.

¹⁷The analogy can be seen from the Maxwell equation $\nabla \cdot \mathbf{D} = \rho$, boundary conditions $D_{A,n} = D_{B,n}$ and $E_{A,t} = E_{B,t}$, and the relation between electric displacement field and electric field $\mathbf{D} = \epsilon_r \epsilon_0 \mathbf{E}$.

Chapter 2

Disordered Quantum Well

There is a long-standing interest in understanding the effects of disorder on the excitons in the quantum wells where the interface and alloy disorder dominate, as indicated in Fig. 2.1. Even though the huge amount of work has been devoted to exciton in quantum wells there is still a lot of to be done. Here we leave the standardly used factorization approximation of the exciton wave function which leads to numerically very demanding calculations. The purpose of this is to describe correctly the behavior of exciton in the perpendicular magnetic field.

2.1 Hamiltonian

We may continue where we have stopped in Sec. 1.7. First, the gauge of the magnetic field has to be chosen. A Coulomb gauge in relative coordinates

$$\mathbf{A}_e(\mathbf{r}_e) = \frac{B}{2}(y_e - y_h, -(x_e - x_h), 0), \quad \mathbf{A}_h(\mathbf{r}) = -\mathbf{A}_e(\mathbf{r}),$$

which induces oscillating terms in the wave function of type $e^{-ie\mathbf{A}(\mathbf{r})\cdot\mathbf{r}/\hbar}$, has been selected. These oscillations are restricted to the wave function extension in relative space, which is of the order of the exciton Bohr radius (see appendix B for details of gauge transformation and numerical implementation).

Second, the spin dependent part of the Hamiltonian Eq. (1.72) will not be written explicitly further and our results are valid for the spin averaged energies Eq. (1.98). This linear contribution may be estimated for a 4 nm wide GaAs/AlGaAs quantum well which is investigated lateron. Taking $g_{exc} \sim 1.4$ the splitting is $\Delta_{12} = 58 \mu\text{eV}$ at $B = 1 \text{ T}$.

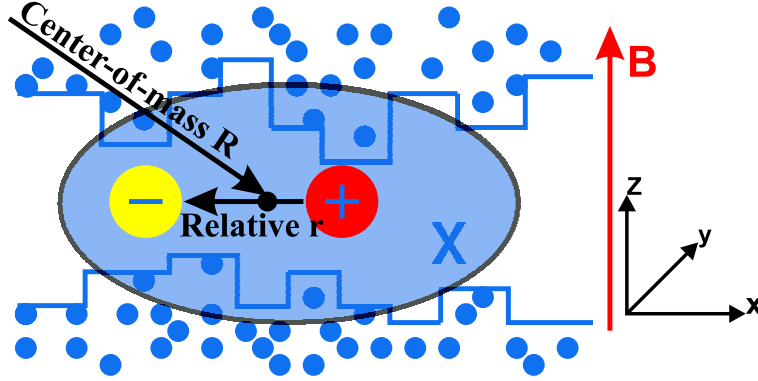


Figure 2.1: Schematic picture of the exciton in the quantum well with interface and alloy disorder. Perpendicular magnetic field, relative and center-of-mass coordinates are indicated.

Third, as we know no quantum well is, of course, perfect. The real potential $U_a(\mathbf{r}_a, z_a)$ can be divided into two parts

$$\begin{aligned} U_a(\mathbf{r}_a, z_a) &= U_a(z_a) + W_a(\mathbf{r}_a, z_a), \\ U_a(z_a) &= \langle U_a(\mathbf{r}_a, z_a) \rangle_{xy}, \end{aligned} \quad (2.1)$$

where $\langle \rangle_{xy}$ means averaging over xy -plane. The first part $U_a(z_a)$ is a confining potential and the second part $W_a(\mathbf{r}_a, z_a)$ is due to disorder whose properties are analyzed in the next Section.

Finally, staying within the single sublevel approximation Eq. (1.64), the in-plane Hamiltonian Eq. (1.72) in the relative and center-of-mass coordinates Eq. (1.39) can be rewritten in the following way

$$\begin{aligned} \hat{H}_{exc} &= -\frac{\hbar^2}{2\mu}\Delta_{\mathbf{r}} - \frac{\hbar^2}{2M}\Delta_{\mathbf{R}} + \frac{eB}{2} \left(\frac{1}{m_e} - \frac{1}{m_h} \right) i\hbar(y\partial_x - x\partial_y) + \frac{e^2 B^2}{8\mu} r^2 \\ &+ \frac{eB}{M} i\hbar(y\partial_X - x\partial_Y) + W_e \left(\mathbf{R} + \frac{m_h}{M} \mathbf{r} \right) + W_h \left(\mathbf{R} - \frac{m_e}{M} \mathbf{r} \right) - V_C(\mathbf{r}). \end{aligned} \quad (2.2)$$

where $W_a(\mathbf{r}_a)$ is the averaged in-plane disorder (compare with Eq. (1.71))

$$W_a(\mathbf{r}_a) = \int dz_a v_a^2(z_a) W_a(\mathbf{r}_a, z_a). \quad (2.3)$$

The eigenenergies are solutions of the stationary Schrödinger equation

$$\hat{H}_{exc} \Psi_\alpha(\mathbf{r}, \mathbf{R}; B) = E_\alpha(B) \Psi_\alpha(\mathbf{r}, \mathbf{R}; B), \quad (2.4)$$

at a given magnetic field B . Zero of energy is taken at the quantum well gap plus electron and hole confinement energy.

In the Hamiltonian Eq. (2.2) there are three magnetic field dependent terms: The first term ($\sim B$) is proportional to the angular momentum in the growth direction

$$i\hbar(y\partial_x - x\partial_y) = \hat{L}_z. \quad (2.5)$$

Without disorder l_z (eigenvalue of the operator \hat{L}_z) is a good quantum number and only states with $l_z = 0$ (s-states) are bright. The second one ($\sim B^2$) gives rise to the well-known quadratic energy shift, which without disorder is equal to

$$\gamma = \frac{e^2}{8\mu} \langle |\mathbf{r}^2| \rangle \propto \frac{a_B^2}{\mu}. \quad (2.6)$$

This term gives always a positive contribution to the energy. The last term describes the B dependent mixing of relative and center-of-mass motion, which is again zero for bright states without disorder. The first and the third term together contribute negatively to the ground state energy for small magnetic fields.

Apart from the *diamagnetic shift coefficient* Eq. (1.95) γ_α ¹ (dropping subscript 2 from now) a state dependent *diamagnetic shift* ΔE_α is defined for our purposes as

$$\Delta E_\alpha(B) = E_\alpha(B) - E_\alpha(0). \quad (2.7)$$

The exciton diamagnetic shift has been already calculated in idealized quantum structures [WR98]. It gives additional information about the interplay between Coulomb interaction and transversal confinement. The influence of a perpendicular magnetic field on the dispersion relation of the exciton was investigated, too: The transition from a hydrogen like exciton towards the magneto-exciton (with increased electron-hole separation proportional to center-of-mass momentum and $1/B$) was predicted leading to the increase of the total mass of the exciton [LOV⁺02].

2.2 Disorder

The physical processes responsible for disorder in quantum wells are the island formation and random positions of the atoms in the ternary alloy since most of the barriers consist of ternary alloys as e.g. GaAs/AlGaAs.

¹Since the parabolic dependence of the eigenvalue E_α on B holds pretty well up to $B = 1$ T, we have calculated it numerically in as the energy difference $\gamma_\alpha = E_\alpha(B = 1 \text{ T}) - E_\alpha(0)$.

In order to model disorder the bandgap fluctuations are introduced as a suitable average with averaging function $A(\mathbf{r}_i, z_j)$ over a white noise random potential $U(\mathbf{r}_i, z_j)$ on the discrete (lattice) grid

$$W(\mathbf{r}_i, z_j) = \sum_{k,l} A(\mathbf{r}_i - \mathbf{r}_k, z_j - z_l) U(\mathbf{r}_k, z_l), \quad (2.8)$$

$$\langle U(\mathbf{r}_k, z_l) \rangle = 0, \quad \langle U(\mathbf{r}_i, z_j) U(\mathbf{r}_k, z_l) \rangle = \delta_{ik} \delta_{jl}, \quad (2.9)$$

where \mathbf{r}_i is a two-dimensional vector on a square grid. The statistical information is fully contained in the (three-dimensional) potential autocorrelation

$$C(\mathbf{r}_i, z_j) = \langle W(\mathbf{r}_{i+l}, z_{j+l}) W(\mathbf{r}_l, z_l) \rangle_l, \quad (2.10)$$

which simplifies in Fourier space to

$$C(\mathbf{k}_i, k_{z,j}) = |A(\mathbf{k}_i, k_{z,j})|^2. \quad (2.11)$$

The bandgap fluctuation are then divided between electron and hole (see Eq. (1.56))

$$W_a(\mathbf{r}_i, z_j) = f_a W(\mathbf{r}_i, z_j). \quad (2.12)$$

A fully correlated electron and hole disorder potential can be modelled in this way, other sources of disorder like charge impurities do not allow to separate disorder into one-particle ones and are neglected by this approach.

Two disorder parameters are usually regarded as the most relevant for its description: (i) variance σ_D^2 of the disorder potential

$$\sigma_D^2 = \langle W^2(\mathbf{r}_i, z_j) \rangle = C(\mathbf{0}, 0), \quad (2.13)$$

and (ii) the correlation lengths, which depend on the precise form of the averaging function $A(\mathbf{r}_i, z_j)$. If a Gaussian averaging function is assumed then

$$A(\mathbf{r}_i, z_j) = \frac{\sigma_D}{\eta} e^{-|\mathbf{x}_i|^2/(2l_{c,x}^2) - |\mathbf{y}_i|^2/(2l_{c,y}^2) - |z_j|^2/(2l_{c,\perp}^2)}, \quad (2.14)$$

$$\eta^2 = \sum_{ij} e^{-|\mathbf{x}_i|^2/l_{c,x}^2 - |\mathbf{y}_i|^2/l_{c,y}^2 - |z_j|^2/l_{c,\perp}^2}, \quad (2.15)$$

where $l_{c,x(y)}$ ($l_{c,\perp}$) is the x (y) in-plane (perpendicular) correlation length. The existence of more than one correlation lengths is reasonable since the growth in z and xy direction is different, and due to the surface reconstruction also x and y correlation lengths may differ.

The adoption of ad hoc parameters for the disorder should be avoided by calculating the exciton properties in structures which have been modelled by state-of-the-art growth simulations. Surprisingly enough, to our

best knowledge there is only one such an attempt with rather simple growth simulations [ZGR97]. Unfortunately this attempt concentrated only on the testing of the validity of the rigid exciton approximation which is described in the next Section.

2.3 Rigid exciton approximation

This approximation is well established in the literature due to its simplicity and reliability. The motivation behind is intuitive: an unperturbed relative motion can be assumed for weak disorder since the strength of the Coulomb interaction dominates. The influence of the disorder is seen mainly by the center-of-mass part since the translational invariance has been broken. The total wave function is factorized into relative and center-of-mass part [ZGR97]

$$\Psi_\alpha(\mathbf{r}, \mathbf{R}; B) = \phi_{1s}(\mathbf{r}; B)\psi_\alpha(\mathbf{R}; B), \quad (2.16)$$

where $\phi_{1s}(\mathbf{r}; B)$ is the solution of the relative motion Schrödinger equation without disorder,

$$\left(-\frac{\hbar^2}{2\mu}\Delta_{\mathbf{r}} + \frac{e^2 B^2}{8\mu}r^2 - V_C(r) - E_{1s}(B) \right) \phi_{1s}(\mathbf{r}; B) = 0. \quad (2.17)$$

As mentioned before, the term linear in B is zero for s-states. Proceeding further, the center-of-mass equation reads

$$\left(-\frac{\hbar^2}{2M}\Delta_{\mathbf{R}} + W(\mathbf{R}; B) \right) \psi_\alpha(\mathbf{R}; B) = E_\alpha(B)\psi_\alpha(\mathbf{R}; B) \quad (2.18)$$

with the disorder potential averaged by the relative wave function

$$W(\mathbf{R}; B) = \sum_{a=e,h} \int d\mathbf{r}_a \beta_a^2 \phi_{1s}^2(\beta_a(\mathbf{r}_a - \mathbf{R}); B) W_a(\mathbf{r}_a), \quad (2.19)$$

where $\beta_e = M/m_h$ and $\beta_h = M/m_e$. In the limiting case when the correlation length of the disorder potential $W_a(\mathbf{r}_a)$ fulfills $\lambda_W = \lambda_{W,e(h)} \ll a_B$ and the wave function $\phi_{1s}(\mathbf{r})$ is approximated by $\phi_{1s}^2(\mathbf{r}) = \frac{2}{\pi a_B^2} e^{-2r/a_B}$, the variance of the averaged potential Eq. (2.19) is

$$\sigma_{D,R} = \frac{\lambda_W^2}{a_B^2} (\beta_e^2 \langle W_e^2(\mathbf{0}) \rangle + \beta_h^2 \langle W_h^2(\mathbf{0}) \rangle + 8 \langle W_e(\mathbf{0}) W_h(\mathbf{0}) \rangle). \quad (2.20)$$

This expression shows that the potential fluctuation are reduced substantially by the factor $\frac{\lambda_W^2}{a_B^2}$ after averaging. The more explicit expression can be

obtained if models for alloy² and interface³ disorder are taken into account (see e. g. [Run02]).

Within the factorization ansatz the oscillator strength Eq. (1.53) reduces to

$$M_\alpha^{fact}(B) = \phi_{1s}(0; B) \int d\mathbf{R} \psi_\alpha(\mathbf{R}; B). \quad (2.21)$$

The state dependent diamagnetic shift Eq. (2.7) takes the following form

$$\Delta E_\alpha(B) = E_{1s}(B) - E_{1s}(0) + E_\alpha(B) - E_\alpha(0). \quad (2.22)$$

The first part $E_{1s}(B) - E_{1s}(0)$ is state independent and proportional to B^2 for small B . The second part $E_\alpha(B) - E_\alpha(0)$ is state dependent and also proportional to B^2 for small B . Since B tends to shrink the wave function $\phi_{1s}(\mathbf{r}; B)$, averaging is less effective: Potential minima become deeper, and have greater curvature. The center-of-mass potential change is quadratic for small B as can be easily checked by inserting a wave function from the second order perturbation theory ($\sim B^2$) into Eq. (2.19).

Within this factorization scheme, good agreement between theory and experiment could be achieved if the variance σ_D^2 and the in-plane correlation lengths $l_{c,x(y)}$ of the disorder were adjusted. The statistics of the oscillator strength was studied with two distinct regimes where Anderson localized states or Lifshitz tail states are dominant [RZ00]. Further, the enhanced resonant backscattering [LRSZ02], the resonant Rayleigh scattering [KLW⁺03], and quantum mechanical level repulsion [IEL⁺01] provided relevant information about disorder.

2.4 Analysis of the wave function

The complicated behavior of the four coordinate wave function can be better investigated by focusing on the projections of the wave function

$$\phi_\alpha^2(\mathbf{r}; B) = \int d\mathbf{R} \Psi_\alpha^2(\mathbf{r}, \mathbf{R}; B), \quad (2.23)$$

$$\psi_\alpha^2(\mathbf{R}; B) = \int d\mathbf{r} \Psi_\alpha^2(\mathbf{r}, \mathbf{R}; B). \quad (2.24)$$

²The alloy disorder can be modeled by the expression $W_a(\mathbf{r}_a) = \sum_i (n_i(\mathbf{r}_a) - x) \frac{dE_a}{dx} \Delta_i$ where $n_i(\mathbf{r}_a)$ is equal to 1 (0) if the atom of the third element (Al in AlGaAs) is (not) found in the i^{th} unit cell, $\frac{dE_a}{dx}$ is the first derivative of the conduction or valence band offset with respect to the average concentration x , and Δ_i is non-zero only in the i^{th} unit cell.

³The interface disorder can be modelled by the the well width fluctuations $W_a(\mathbf{r}_a) = (L(\mathbf{r}_a) - \bar{L}) \frac{dE_a}{dL}$ where $L(\mathbf{r}_a)$ is the local well width, \bar{L} is the average well width, and $\frac{dE_a}{dL}$ is the first derivative of the conduction or valence band offset with respect to the well width.

The projected relative wave function $\phi_\alpha^2(\mathbf{r}; B)$ does not vary much qualitatively between different local ground states: It is nodeless and rather isotropic due to the strength of the Coulomb interaction. Therefore, the value $\phi_\alpha^2(\mathbf{0}; B)$ is sufficient to characterize $\phi_\alpha^2(\mathbf{r}; B)$ and gives information about the extension of the relative wave function. We define a relative measure related to the no-disorder and zero B field case by

$$\rho_\alpha = \frac{\phi_\alpha^2(\mathbf{0}; B)}{\phi_{1s}^2(\mathbf{0}; 0)}, \quad (2.25)$$

where $\phi_{1s}^2(\mathbf{0}; 0)$ is structure specific and has the value of

$$\phi_{1s}^2(\mathbf{0}; 0) = 0.00582 \text{ nm}^{-2} \quad (2.26)$$

for parameters described below. The larger the value ρ_α , the smaller is the relative projection extension Eq. (2.23). The center-of-mass projections Eq. (2.24) are plotted using contour plots. The localization of the wave function can be visualized in this way.

2.5 Comparison between full solution and factorization

In this more technical section we compare the factorization and the full solution and show where the limitations of the factorization lie. We investigate a 4 nm wide GaAs/Al_{0.3}Ga_{0.7}As quantum well whose material parameters are listed in Tab. A.1. Up to now all derivations were valid for both heavy and light hole supposing that they are decoupled.⁴ Fig. 2.2 shows the confinement profile of a quantum well with two confinement wave functions and their energies. Since the energy difference between heavy $E_{C,hh} = 29.1$ meV and light hole confinement energies $E_{C,lh} = 60.7$ meV is 30 meV, which is large compared with heavy hole exciton binding energy of ≈ 12 meV, we take into account only the heavy hole in what follows.

As a model for disorder we have chosen Gaussian distributed and spatially uncorrelated fluctuations of the bandgap $W(\mathbf{r}_i)$ on a square grid with a grid step of 4 nm, neglecting thus the averaging Eq. (2.3). One example of $W(\mathbf{r}_i)$ is shown in Fig. 2.3

2.5.1 No magnetic field

Absorption spectra Eq. (1.54) calculated with and without factorization are compared for a single disorder realization in Fig. 2.4. Good agreement is

⁴Apart from the spin which is not written explicitly in this Chapter.

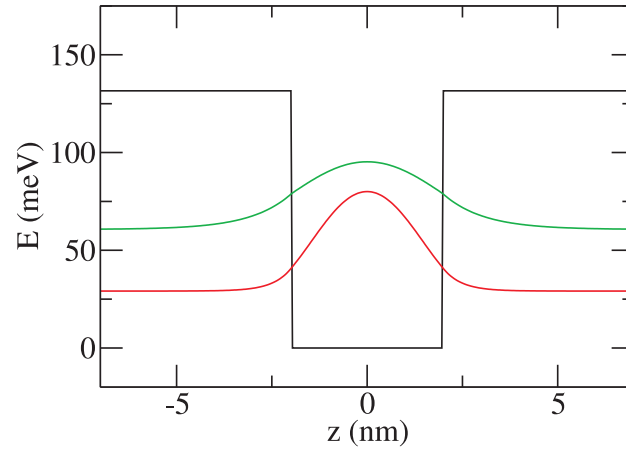


Figure 2.2: The quantum well hole confinement profile with the heavy and light hole wave function positioned at their confinements energies $E_{C,hh} = 29.1$ meV and $E_{C,lh} = 60.7$ meV.

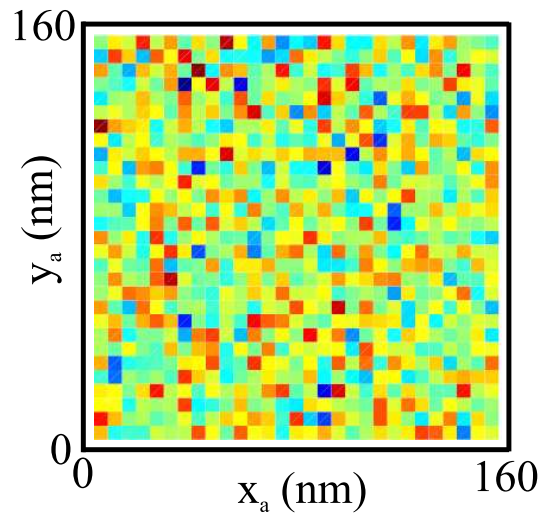


Figure 2.3: An example of the one disorder realization, 40×40 points with 4 nm step.

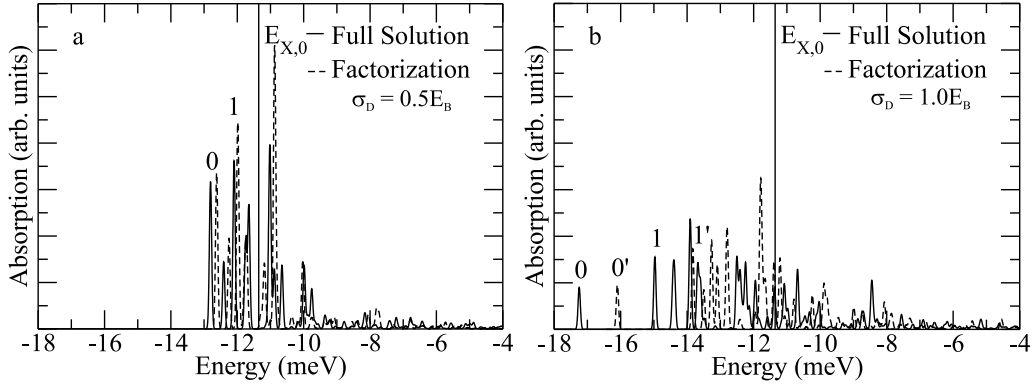


Figure 2.4: Calculated absorption spectra for two different strengths of the disorder ($\sigma_D = 0.5 E_B$ (a) and $\sigma_D = 1.0 E_B$ (b)). The full solution (solid) and factorization (dashed) are plotted. Two optically active states for each calculation are marked (with 0', 1' for factorization in b). Corresponding wave functions are shown in Fig. 2.5. Total simulation size is $160 \times 160 \text{ nm}^2$ with a grid step of 4 nm.

expected in the case of weak disorder where the factorization assumption of unperturbed relative motion is almost valid. Indeed, this is found in Fig. 2.4 a, *seemingly* approving the factorization. However, the ground state energy in the full solution is lower than in the factorization, which is consistent with variational arguments. The different effective (numerical) averaging in the full solution and factorization also contributes to the 0.2 meV rigid shift of all states in Fig. 2.4 a. Our calculations have shown that these shifts are magnetic field independent. The spectrum agreement worsens above the ideal exciton position $E_{X,0}$ (line in Fig. 2.4: $E_{X,0} = -E_B = -11.4 \text{ meV}$) where states mix with the ideal 2s state. Due to orthogonality, these states are modified by different local ground states, even if their relative parts in the full solution and factorization were similar. In the case of stronger disorder (Fig. 2.4 b) even the qualitative agreement is lost. A correspondence between wave functions may be expected only for the first few tail states since they are local ground states in deep minima.

For a better understanding it is important to distinguish between the local potential shape relevant for the localized exciton state and the global disorder given by the variance σ_D^2 . The local potential is characterized by a limited number of parameters, e.g. discrete values on grid points close to the position of the localized exciton. The change of the (global) disorder strength modifies the potential statistics. A relatively shallow minimum, which is highly probable in case of weak disorder, is less likely in a case with stronger disorder, where more deeper minima with strong curvatures

exist. The disorder strength determines *only the probability* of highly localized states which are not well described by a simple factorization ansatz since the effective compression of the relative part is neglected. The stronger the global disorder, the higher the probability that the factorization fails.

Next, we concentrate on the wave function properties. The center-of-mass projection Eq. (2.24) and the relative wave function measure ρ_α are shown in Fig. 2.5 for the same disorder realization used in Fig. 2.4. Several interesting features turn up. The values of ρ_α vary in the full solution between states: The most localized center-of-mass states have also the most compressed relative parts (greatest values ρ_α). This is physically understandable since a stronger localization of electron and hole leads to an effectively stronger Coulomb interaction, which is then state dependent.

Another appealing feature is the (dis)agreement of center-of-mass parts in the full solution and the factorization. The projections Eq. (2.23) and Eq. (2.24) play a different role: The relative part averages the disorder potential for the center-of-mass motion. This means that a small alteration in the relative part leads to a small alteration in the effective center-of-mass disorder potential and further in the center-of-mass localization (Fig. 2.5). This simple picture is not valid in the case of stronger disorder (Fig. 2.4 b). The ideal relative wave function $\phi_{1s}(\mathbf{r}; B)$ averages so that some minima can become too shallow (or even disappear), since $\phi_{1s}(\mathbf{r}; B)$ is more extended in size compared with the full solution. The energetic position can be shifted and the center-of-mass wave function can be changed (see specifically Fig. 2.5 f and h).

Using the wave function projections Eq. (2.23) and Eq. (2.24) we compare the localization of the center-of-mass projection in Fig. 2.5 and the oscillator strength of these states plotted in Fig. 2.4. The correspondence is found for the two plotted states: the most localized center-of-mass projection has the smallest oscillator strength. The contribution of the relative projection grows with the compression unlike the center-of-mass contribution which decreases with localization. This implies that the oscillator strength is predominantly determined by center-of-mass localization for local ground states.

2.5.2 Diamagnetic shift

So far only the disorder effect on the exciton was discussed. Now we include the perpendicular magnetic field in our comparison between the full solution and the factorization.

We focus again on the wave function projections Eq. (2.23) and Eq. (2.24) for a deeper understanding: The relative projection is affected proportional to its extension ($\sim \langle r^2 \rangle$). Since in the factorization the ideal relative wave

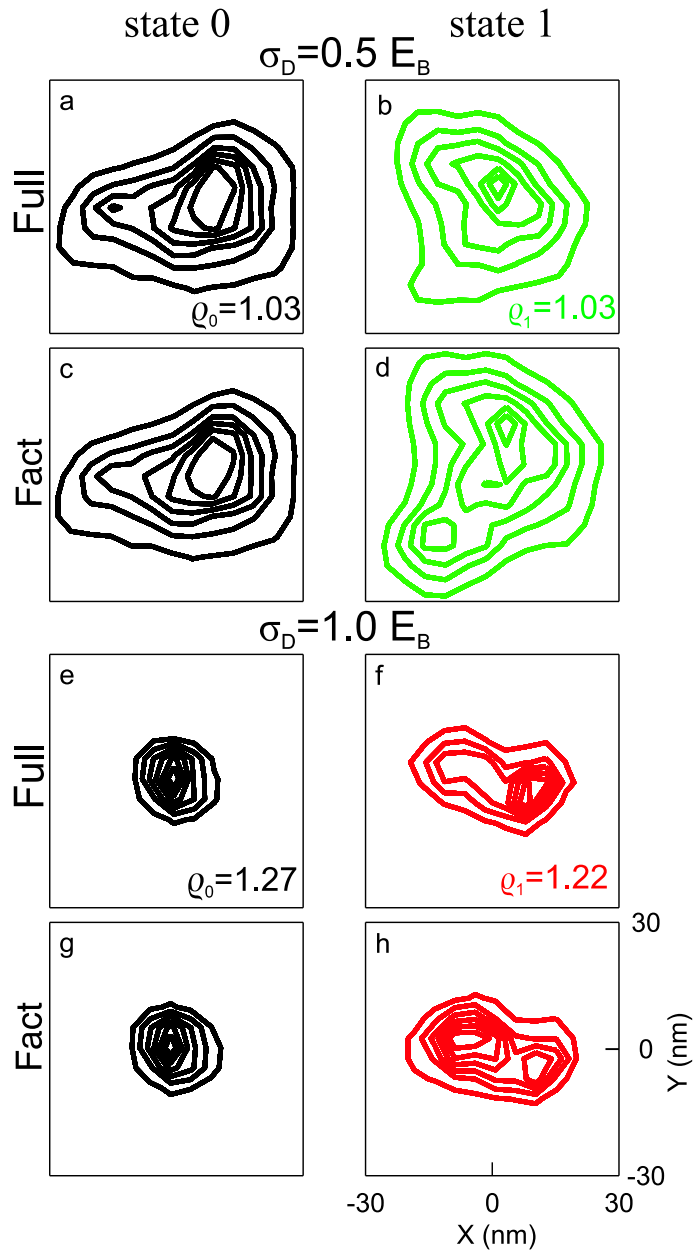


Figure 2.5: The probability densities of the center-of-mass part (projection) of the total wave functions Eq. (2.24) calculated for states (0, 1) of Fig. 2.4 as contour plots. [Inc01] Full solution (a, b, e, f) and factorization (c, d, g, h) for $\sigma_D = 0.5 E_B$ (a - d) and $\sigma_D = 1.0 E_B$ (e - h). The values ρ_α Eq. (2.25) are shown for each wave function in the full solution (in the factorization $\rho_\alpha \equiv 1.00$ per definition). Total simulation size is $160 \times 160 \text{ nm}^2$ with a grid step of 4 nm.

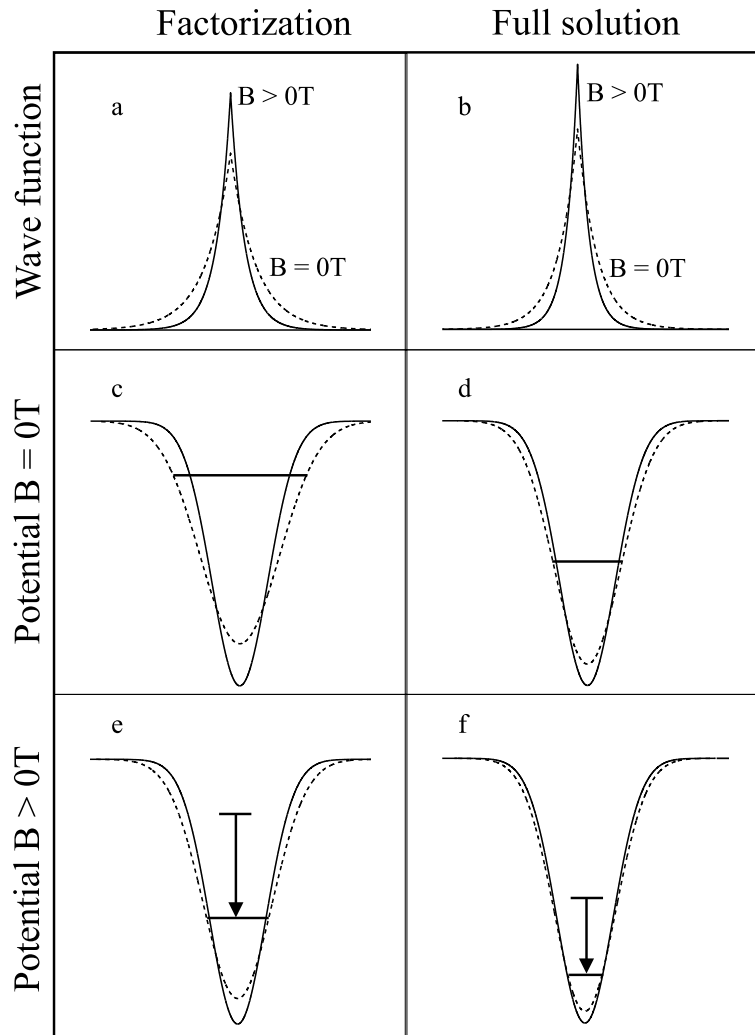


Figure 2.6: Schematic drawing of the exciton relative wave function (factorization a and full solution b) and original (solid) and averaged potential (dashed) as a functions of magnetic field. Energy levels are also depicted. The arrows indicate the negative center-of-mass contribution to the diamagnetic shift, the positive contribution from the relative motion is not shown.

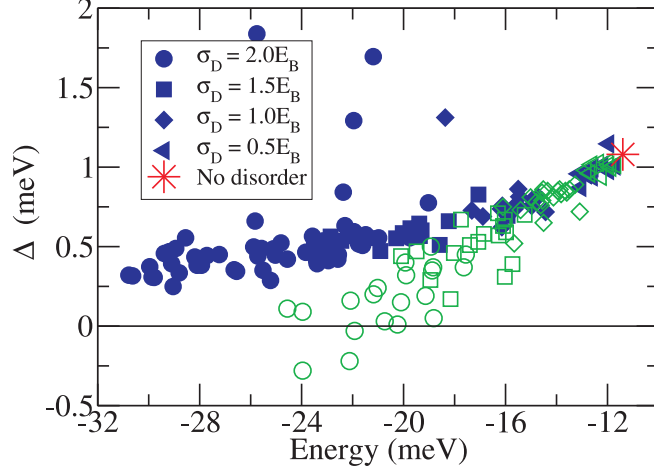


Figure 2.7: The distribution of the diamagnetic shifts at $B = 5$ T calculated with the full solution (full symbols) and factorization (open symbols) for different strengths of disorder. The grid step of 4 nm is used.

function $\phi_{1s}(\mathbf{r}; B)$ is used, it changes more with magnetic field than in the full solution, which is already shrunk due to localization as discussed above. This is schematically depicted in Fig. 2.6 a and b. The effective averaged center-of-mass potential minimum is then more shallow in the factorization, and the bound state has a higher energy (Fig. 2.6 c and d). The magnetic field has a greater impact on the effective center-of-mass potential in the factorization (Fig. 2.6 e) than in the full solution (Fig. 2.6 f). In the factorization both contributions to the diamagnetic shift are overestimated: The relative one proportional to $\langle r^2 \rangle$ (not shown in Fig. 2.6) and the downshift of the center-of-mass energy. If full solution and factorization agree without magnetic field, then also the diamagnetic shift agrees. In other cases (depending on local disorder), agreement is not to be expected. Unfortunately, looking at the potential landscape it is not clear from the beginning, to which extent the factorization and the full solution agree.

Furthermore, taking calculations for different realizations and disorder strengths, a statistics of the diamagnetic shift can be obtained as shown in Fig. 2.7. The analysis is always performed only for the first few tail states. The increase of the average diamagnetic shift with eigenenergy is obvious. The no-disorder case is marked as a star, and is properly positioned on the trend line. The existence of the trend line for the diamagnetic shift going through several disorder strengths is non trivial. In the present case, value and shape of minima are mainly fixed by the eigenenergy and depend much

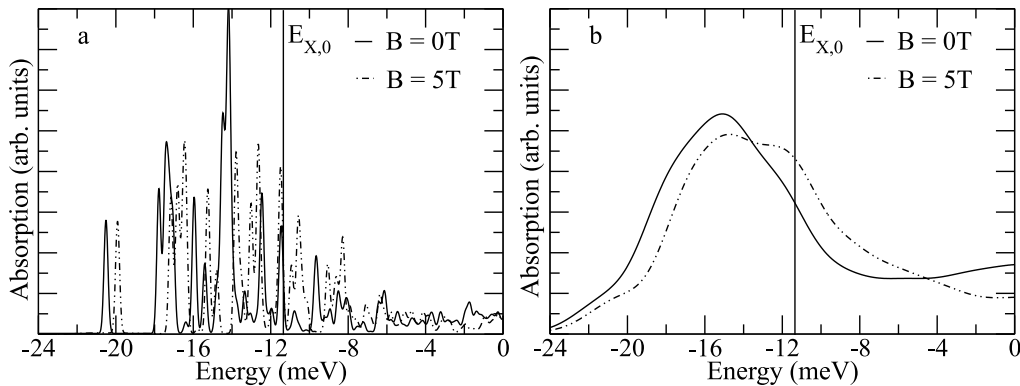


Figure 2.8: Absorption spectra calculated for two different magnetic fields (solid 0 T, dashed 5 T) and for a single disorder realization (a) (Gaussian broadening of single line $\sigma = 0.1$ meV Eq. (C.8)) and averaged over 12 realizations of disorder (b) (Gaussian broadening of single line $\sigma = 1.0$ meV). Disorder strength in both cases $\sigma_D = 1.5 E_B$. Total simulation size is 160×160 nm² with a grid step of 4 nm.

less on the global disorder strength.

The deviations between the full solution and the factorization increase with decreasing eigenenergy. This is well understood since highly localized states are not properly described in the factorization. The state independent relative wave function in the factorization may even lead to negative diamagnetic shifts in very deep potential minima, which is never observed in the full solution and is according to Sec. 1.7.1 forbidden. This is the strongest argument against the factorization.

2.6 Diamagnetic shift and wave function localization

Now we may turn our attention towards the relation between the localization of the wave function and the diamagnetic shift.

First, we start with literature overview since the combined effect of a perpendicular magnetic field and alloy disorder has been already investigated. The shift of the maximum of the photoluminescence peak towards higher energies was calculated together with a modification of the lineshape. The calculation was based on the factorization scheme, but center-of-mass wave functions were treated phenomenologically [Lyo94]. Also recent PL measurements reveal interesting features with magnetic field, namely the change of the PL peak shape and shift of the maximum [SBJ⁺03]. The calculation explaining

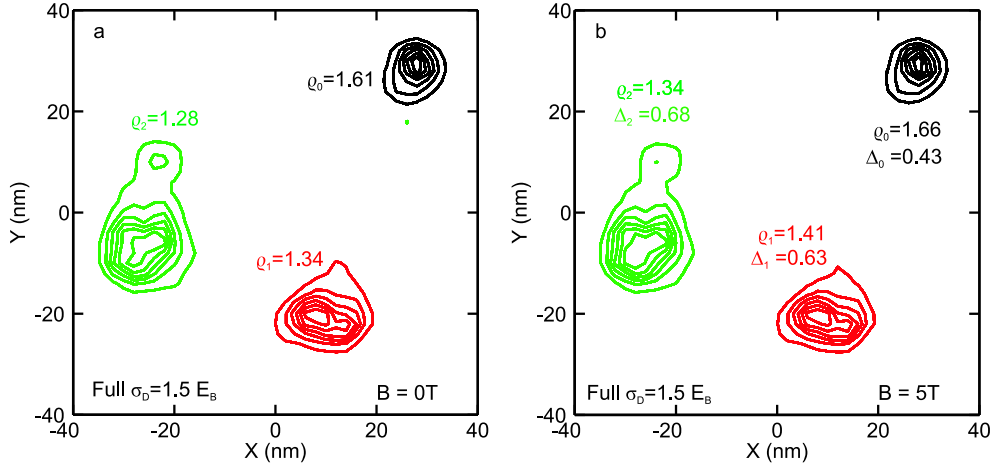


Figure 2.9: The probability densities of the center-of-mass projection of the total wave functions Eq. (2.24) calculated for the energetically lowest three states of the full solution for $\sigma_D = 1.5 E_B$ (a $B = 0$ T, b $B = 5$ T) as contour plots. [Inc01] A grid step of $\Delta = 2$ nm is used. The values ρ_α Eq. (2.25) are shown for each wave function. The diamagnetic shift $\Delta E_\alpha(B)$ in meV is given, too (without disorder, $\rho_{1s} = 1.123$ and $\Delta_{1s} = 1.08$ meV).

the experimental observations was performed with a rather simplified theory assuming a complete localization of holes in the GaAsSbN/GaAs structure under study. The well-known near-field optical experiment [HBH⁺94] and recent micro-photoluminescence spectra [ERW⁺06] have demonstrated on GaAs/AlGaAs quantum wells that the diamagnetic shift differs between localized excitons. Even negative diamagnetic shifts or spin splitted triplets were observed.

Second, the change of the absorption spectra Eq. (1.54) with magnetic field is shown in Fig. 2.8. The first few localized states can be recognized unambiguously, and the diamagnetic shift can be read off easily from Fig. 2.8 a. The changes of the oscillator strength $M_\alpha(B)$ with magnetic field can be extracted, too, but are marginal. The effects of the magnetic field on averaged (over several disorder realizations) spectra (Fig. 2.8 b) are the shift of the maximum and a widening since the diamagnetic shift $\Delta E_\alpha(B)$ increases in average with energy $E_\alpha(0)$. This average increase can also explain the changes in PL spectra. Here, the occupation of states enters in addition. Since higher states have lower occupation, the effect is weaker with respect to absorption spectra. Our simulations predict the widening with magnetic field in accordance with [SBJ⁺03] and [Lyo94].

Third, the influence of the magnetic field on the wave functions can be

seen in Fig. 2.9. The correlation between center-of-mass and relative projection is observed again. A new feature is the correlation between the diamagnetic shift and wave function extension. The diamagnetic shift for the three states is given in Fig. 2.9 b. As mentioned above the relative part is affected proportionally to its extension ($\langle r^2 \rangle$), which is illustrated by the change of ρ_α values in Fig. 2.9, where the smallest change with magnetic field is found for the ground state. In general, the diamagnetic shift ΔE_α is inversely correlated to the relative measure ρ_α . The positive relative contribution $\sim \langle r^2 \rangle$ is dominant. The center-of-mass contribution is negative but not necessarily small in absolute value. Minor modifications of the relative part may induce substantial modifications of the center-of-mass energy.

From the application side a very important question evolves: Is it possible to reconstruct local potential properties from the diamagnetic shift? The correlation between the diamagnetic shift and localization could be a way to access information about the local potential landscape and therefore the underlying structure. The Section 2.8 focuses on this open question.

2.7 Enhanced electron effective mass

After we have understood the relation between disorder, localization and diamagnetic shift we may look on the influence of the enhanced electron mass on the exciton properties as promised in Sec. 1.8. We take into account two masses (i) the bulk one $m_e^{(1)} = 0.067 m_0$ as used so far and (ii) the enhanced one according to the Eq. (1.107) $m_e^{(2)} = 0.078 m_0$. This choice enables to see where the limitations of the experimental observation of the enhanced mass lie.

First, the absorption spectra Eq. (1.54) are compared in Fig. 2.10. The differences between both spectra are only minor and seen mainly for the tail states. This is caused by the weak dependence of the exciton binding energy on the electron mass. The binding energies are $E_B^{(1)} = 11.4$ meV and $E_B^{(2)} = 12.4$ meV, respectively. Such a small difference makes it difficult to confirm the mass enhancement by measuring the absorption or photoluminescence spectra since excited exciton states (which are needed to extract the binding energy) are hard to observe.

Second, we turn our attention towards the diamagnetic shift coefficient γ_2 . As the disorder-free case Eq. (2.6) suggests, the dependence of the factor γ_2 on the mass m_e is more pronounced. The exciton Bohr radius is reduced due to the mass enhancement from $a_B^{(1)} = 9.0$ nm to $a_B^{(2)} = 8.2$ nm, thus by 10%. Taking into account Eq. (2.6), we may deduce that the diamagnetic shift reduction is proportional to the mass enhancement to the third power

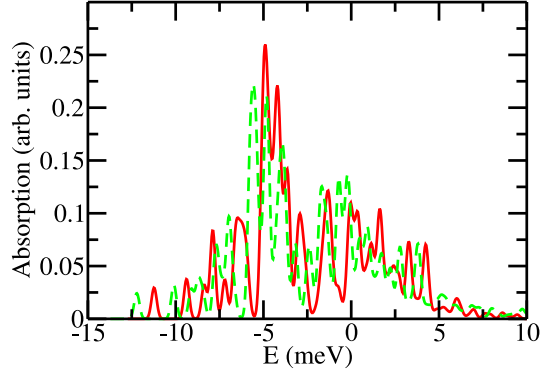


Figure 2.10: Exciton absorption spectra in the disordered quantum well for two effective electron masses: solid $m_e^{(1)}$ and dashed $m_e^{(2)}$ (see text). Simulation size is $96 \times 96 \text{ nm}^2$ for 7 realizations (the numerical grid $\Delta = 1.6 \text{ nm}$) and zero of the energy is the exciton binding energy.

approximately. This means that the slight increase of the electron mass by about 15%, as in our case, reduces the factor γ_2 by 40%. Such a behavior is clearly depicted in the Fig. 2.11a, where ideal cases ($\gamma_2^{(1)} = 50 \mu\text{eV}/\text{T}^2$ and $\gamma_2^{(2)} = 37 \mu\text{eV}/\text{T}^2$) are plotted as lines and the disordered ones with markers for localized excitons states.

These results suggest that the correct theoretical interpretation of the experimental γ_2 factors measured on narrow quantum wells cannot be achieved without taking into account the mass enhancement. This is in contrast with many other exciton properties in disordered quantum wells which are not so sensitive to the electron mass.

Finally, the localization of the wave function can be compared in Fig. 2.11 b and c. There are only tiny differences seen in the localization of the plotted local ground state since its localization is proportional to the total exciton mass $M = m_e + m_h$, which changes only by few per cent ($M^{(1)} = 0.3 m_0$ and $M^{(2)} = 0.311 m_0$).

2.8 Real quantum well

Now it is the right moment to compare our theory with experiments. Unlike in all other cases in the literature we are not going to adjust the parameters of the disorder but we deduce them from the experiment. Having these disorder parameters we may apply our theory as before and compare calculated photoluminescence spectra with the measured ones. The fact that the structural data, which is our input into the calculation, and the optical measurements

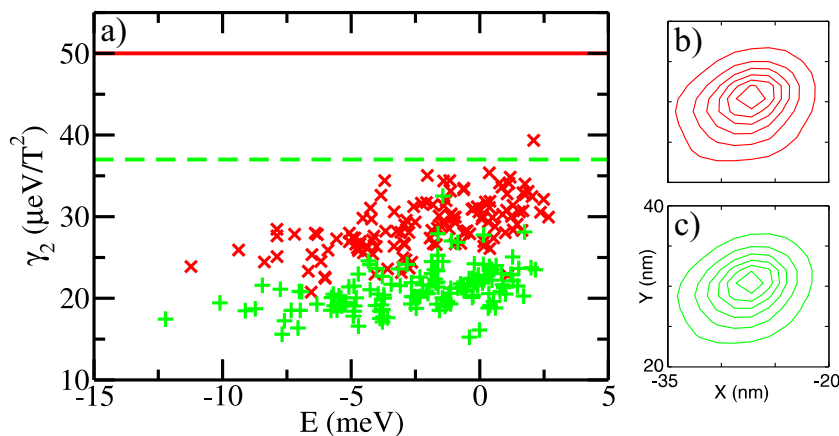


Figure 2.11: Statistics of the diamagnetic shift γ_2 : diagonal crosses using $m_e^{(1)}$, circles $m_e^{(2)}$, solid (dashed) line: no disorder for $m_e^{(1)}$ ($m_e^{(2)}$). The center-of-mass projection of the wave functions Eq. (2.24) of the local ground state using b) $m_e^{(1)}$ and c) $m_e^{(2)}$.

were performed on the same spot of the sample enables to verify the validity of the theory.

2.8.1 Experiment

The investigated heterostructure contained five intrinsic GaAs quantum wells of 4, 6, 8, 10 and 20 nm nominal widths, separated by 15 nm wide barriers of intrinsic $\text{Al}_{0.3}\text{Ga}_{0.7}\text{As}$. The structure was grown by molecular beam epitaxy. The cross-sectional scanning tunneling microscopy (XSTM) measurements were performed on an atomically smooth (110) surface, which had been prepared by in-situ cleavage of the sample in an ultra high vacuum. Cross-sectional constant-current topographs of all five quantum wells were taken with atomic resolution over lateral lengths of typically 200 nm. After the XSTM measurements, the sample was transferred into a confocal microscope setup with a lateral spatial resolution of 500 nm at a wavelength of 800 nm. The accuracy with which the optical focus and the position of the XSTM measurements coincided was better than 200 μm . Further details of the samples and the experiment can be found in Ref. [REW⁺07].

A section of the constant-current topograph of the 4 nm quantum well is displayed in Fig. 2.12 (the entire topograph is ~ 200 nm long). The image gives the height $h(x, z)$ in linear gray scale which is related to the variations of the Aluminum concentration with atomic precision. Strictly speaking, single Aluminum atoms were not imaged, since at the applied negative bias voltages

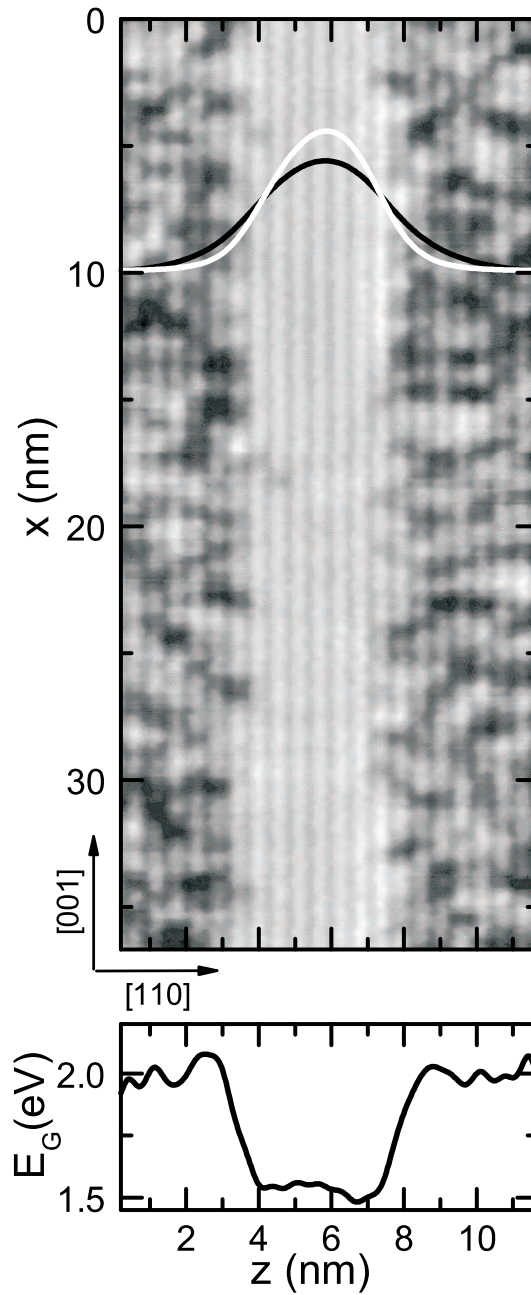


Figure 2.12: Top: Constant-current XSTM topograph of the 4 nm wide quantum well, recorded at a bias voltage of $U_B = -2$ V and a tunneling current $I_T = 100$ pA. The crystallographic axes are indicated. The z -confinement wave functions $v_a^2(z)$ for the electron (black curve) and the heavy hole (white curve). Bottom: Deduced bandgap profile as a function of z , averaged along the x -direction and after removal of the atomic corrugation.

only the group-V sublattice is visible [SA93]. Nonetheless, the topographic variation on an atomic scale demonstrates the sensitivity to the Aluminum distribution. There is a clear difference in the average height $\langle h(x, z) \rangle_x$ between the well and the barrier regions of about 25 pm. We presume that this height difference not only reflects the global difference in the average Aluminum concentrations, but that it can also serve as a local gauge for the Aluminum distribution in the barriers and at the interfaces.

2.8.2 Potential reconstruction and generation

The atomic-scale contrast of the images allows us to extract the structural properties in the cleavage plane that are needed as input in the calculation of optical spectra.

The topographs are assumed to be a direct representation of the local Aluminum concentration and therefore the alloy bandgap in the structure, and a linear scaling of the topography height $h(x_i, z_j)$ to the local band gap is applied,

$$E_G(x_i, z_j) = E_{G, GaAs} + b h(x_i, z_j). \quad (2.27)$$

The scaling factor b is determined by taking a gap difference of 500 meV [VS] to the $\text{Al}_{0.3}\text{Ga}_{0.7}\text{As}$ alloy in the barrier, and was found to be $b = -19.8$ meV/pm. The local band gap is distributed with the band offset ratio $f_e/f_h = 0.65/0.35$.

Applying perturbation theory, the effective in-plane bandgap fluctuations are then given by

$$\tilde{W}(x_i) = \sum_j E_G(x_i, z_j) (f_e v_e^2(z_j) + f_h v_h^2(z_j)). \quad (2.28)$$

Here, the $v_a(z_j)$ are the single particle wave functions Eq. (1.64) in the one-dimensional potential derived from the x -averaged confinement potential $U_a(z_{a,j}) = f_a \langle E_G(x_i, z_j) \rangle_x$ (Fig. 2.12 bottom). The XSTM measurement gives the disorder potential in the cleavage plane ($y = 0$) only, $\tilde{W}(x_i, 0)$. Therefore, the experimental information on the strength and the correlation of the lateral disorder is restricted to the x -direction alone.

However, the disorder in both in-plane directions (x and y) is relevant for the inhomogeneous broadening of excitonic transitions. Although both directions are crystallographically equivalent in zinc blend symmetry, the growth takes place on reconstructed surfaces which can lead to anisotropic growth in the quantum well plane. For instance, the appearance of elongated islands or one-monolayer-deep "holes" has been reported [GVG⁺97]. Any anisotropy of the interfaces shows up clearly in a preferential linear polarization direction

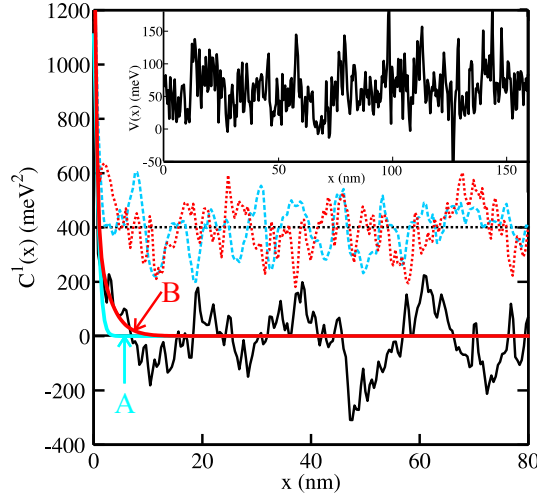


Figure 2.13: The experimental potential autocorrelation (solid black), its fit with ansatz A (blue) and B (red), and an example of the autocorrelation of the numerically generated potential (dotted, for clarity shifted upwards by 400 meV). Inset: The reconstructed one-dimensional potential $\tilde{W}(x_i)$ from the experiment.

of the emission from exciton doublets. This has been confirmed by optical measurements on growth-interrupted samples [GSS⁺96]. The same kind of fine structure splitting but without preferred orientation has been observed. Consequently, we assume that the correlations of the bandgap fluctuations are *isotropic* in the xy -plane, and the reduced information from the XSTM cut along x is sufficient.

The experimental XSTM topograph gives not only a one-dimensional subset of the potential, but is restricted to a limited number of data points ($N = 400$ covering 160 nm, inset of Fig. 2.13). Consequently, the one-dimensional autocorrelation

$$C(x_i) = \frac{1}{N} \sum_{l=1}^N \tilde{W}(x_i + x_l, 0) \tilde{W}(x_l, 0) \quad (2.29)$$

shows large fluctuations at all distances (solid black curve in Fig. 2.13) which do not reflect a statistically relevant correlation. In order to reveal the *true* correlation we have to seek for a fit of the averaging function. Two fit

Table 2.1: Fitted parameters for fit ansatz A and B Eq. (2.30).

	ansatz A	ansatz B
σ_1 (meV)	33.4	11.7
σ_2 (meV)	X	29.8
l_{c1} (nm)	0.4	1.7
l_{c2} (nm)	X	0.2
χ^2 (meV ²) $\times 10^9$	1.82	1.71

functions are considered

$$\begin{aligned}
 \text{A: } A(\mathbf{r}_j) &= \frac{\sigma}{\eta} e^{-|\mathbf{r}_j|/l_c}, & \eta^2 &= \sum_j e^{-2|\mathbf{r}_j|/l_c}, \\
 \text{B: } A(\mathbf{r}_j) &= \frac{\sigma_1}{\eta_1} e^{-|\mathbf{r}_j|/l_{c1}} + \frac{\sigma_2}{\eta_2} e^{-|\mathbf{r}_j|/l_{c2}}, & \eta_i^2 &= \sum_j e^{-2|\mathbf{r}_j|/l_{ci}}, \quad (2.30)
 \end{aligned}$$

where σ_i (l_{ci}) is the weight (the correlation length) of i^{th} component for the fit ansatz B. In the case of ansatz A $\sigma^2 = \langle \tilde{W}^2(\mathbf{r}_j) \rangle = C(0)$ is the potential variance and l_c the correlation length. The obtained values are summarized in Tab. 2.1. The corresponding correlation fits are shown as blue (A) and red (B) curves in Fig. 2.13. The knowledge of the averaging function $A(\mathbf{r}_j)$ allows an effective generation of the potential in (discrete) Fourier space [GB94]

$$\tilde{W}(\mathbf{k}_l) = \tilde{A}(\mathbf{k}_l) \tilde{U}(\mathbf{k}_l), \quad \langle \tilde{U}^*(\mathbf{k}_l) \tilde{U}(\mathbf{k}_j) \rangle = \delta_{lj}. \quad (2.31)$$

where $\tilde{U}(\mathbf{k}_l)$ is a complex-valued Gaussian distributed white noise. The side condition $\tilde{U}^*(\mathbf{k}_l) = \tilde{U}(-\mathbf{k}_l)$ guarantees the reality of the generated potential in real space. Examples of the generated potentials are shown in Fig. 2.14. The difference in the correlation lengths can be clearly observed.

A comparison between the experimental input (solid curve in Fig. 2.13) and numerically generated examples (dotted curves) for the autocorrelation function reveals the existence of fluctuations (speckling) in both cases. Their typical shape, however, matches only in the case of ansatz B, which points to a sub-optimal model for the averaging function $A(\mathbf{r}_j)$ of ansatz A. At this point the conclusion should be made that ansatz B describes better the experiment data. However, a problem is the very limited statistics obtained from the experiment which limits the reliability of the ansatz with four fitting parameters. In the following both ansatz A and B will be discussed since they represent a sort of limiting cases of the short and longer correlation and none of them is perfect in all criteria (comparing theory and experiment).

The interesting aspect is that the information on the correlations in the growth-direction (z) is qualitatively contained in the value of $\sigma = \sqrt{C(0)}$.

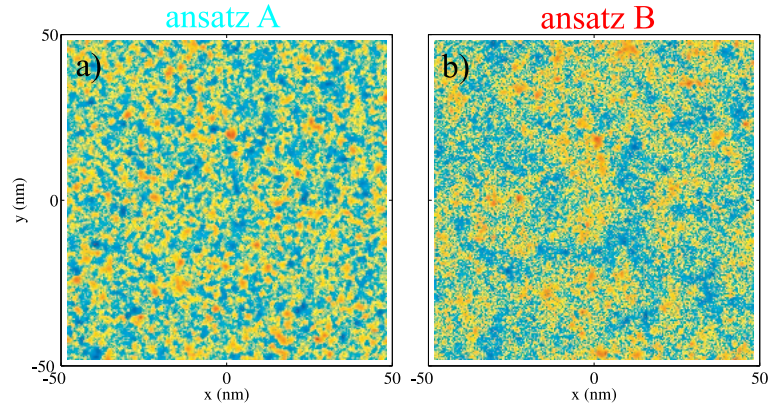


Figure 2.14: Examples of the generated two-dimensional potentials according to the Eq. (2.31).

This can be seen as follows: The value of σ is completely insensitive to lateral (x) correlations as it only represents the standard deviation of the potential. If there are, however, correlations of the local bandgap in the growth-direction, this will result in increased fluctuations of the weighted z -average in Eq. (2.28), compared with a completely uncorrelated Aluminum distribution. The effect of z -correlations in the Aluminum distribution can be quantified by comparing the determined σ -value with that obtained after an intentional removal of all z -correlations from the XSTM-image. This can be done, e.g., by randomly shifting the individual atomic rows in the barriers along the x -direction with respect to each other. For this situation, one obtains a σ of about 30 % smaller than the actual one. Therefore, z -correlations contribute significantly to the inhomogeneous broadening of the optical spectra. In fact, certain z -correlations are already discernible by close inspection of the topograph in Fig. 2.12, where weak stripe-like contrasts in the z -direction are visible, especially in the right barrier regions.

2.8.3 Micro-photoluminescence

A useful comparison between experiment and theory requires the knowledge of the exciton occupation N_α . Unfortunately, a proper calculation of N_α solving kinetic equations [Run02] is technically very demanding in this case, since too many states have to be included.⁵ Instead of calculating these non-equilibrium occupations, we make some physically justified assumptions: At

⁵The main problem is the evaluation of the scattering matrix elements between different exciton states α , β , and acoustic phonons. The exciton wave functions have four coordinates, calculations are performed for $60^4 = 12960000$ grid points.

elevated temperatures, we are pretty sure that the excitons are in thermal equilibrium with a temperature T_X close to the lattice one. As a consequence, absorption Eq. (1.54) (Fig. 2.15 black) and photoluminescence Eq. (1.55) (Fig. 2.15 magenta) are simply related by a Maxwell-Boltzmann occupation factor,

$$P(\omega) = e^{-\hbar\omega/k_B T_X} D(\omega). \quad (2.32)$$

Such a procedure has been used successfully before, e.g. in Ref. [GVMPC94].

However, the occupation of the tail states calculated using Eq. (2.32) would be overestimated at low temperatures [MZKL03]. We circumvent this assuming that all states with the energy lower than a hypothetical PL maximum have a constant occupation. The hypothetical PL maximum is determined as the absorption maximum minus the Stokes shift S which can be approximately calculated as [GVMPC94]

$$S = \frac{\sigma_A^2}{k_B T}, \quad (2.33)$$

where σ_A is obtained by the Gaussian fit of the absorption. This occupation will be called quasi-thermal (Fig. 2.15 orange).

In the optical experiments, micro-photoluminescence (μ PL) with a spatial resolution of 600 nm was measured. Fig. 2.16 shows μ PL spectra of the 4 nm wide quantum well, recorded at a temperatures of 4 K (a) and 50 K (b). Typical features of exciton spectra from disordered quantum wells can be seen [ZBH⁺94; HBH⁺94]: The spectrum shows an inhomogeneous broadening with individual bright peaks on the low-energy side due to strongly localized excitons. On the high-energy side, a more continuous spectrum with many closely spaced peaks is seen.

The temperature dependent change in transition energy due to bandgap reduction [Ada94] was taken into account in the calculations of the spectra at the higher temperature. A bandgap difference of 2.5 meV between the lattice temperatures $T_L = 4$ K and $T_L = 50$ K was precisely determined in the experiment from the shift of individual localized states when the temperature was continuously raised.

The agreement between measured and calculated PL spectrum depends on the used ansatz for the fit function: Excellent agreement is found for ansatz A (Fig. 2.16 blue). Although equilibrium does not hold at $T = 4$ K, the high energy tail of the μ PL can be fitted using Eq. (2.32) with an effective exciton temperature of $T_X = 20$ K (Fig. 2.15a). The overall spectral shape and the inhomogeneous width are well modeled – they are characteristic for the disorder potential considered. Naturally, the individual peak positions cannot be compared due to the inherent randomness of the potential generation.

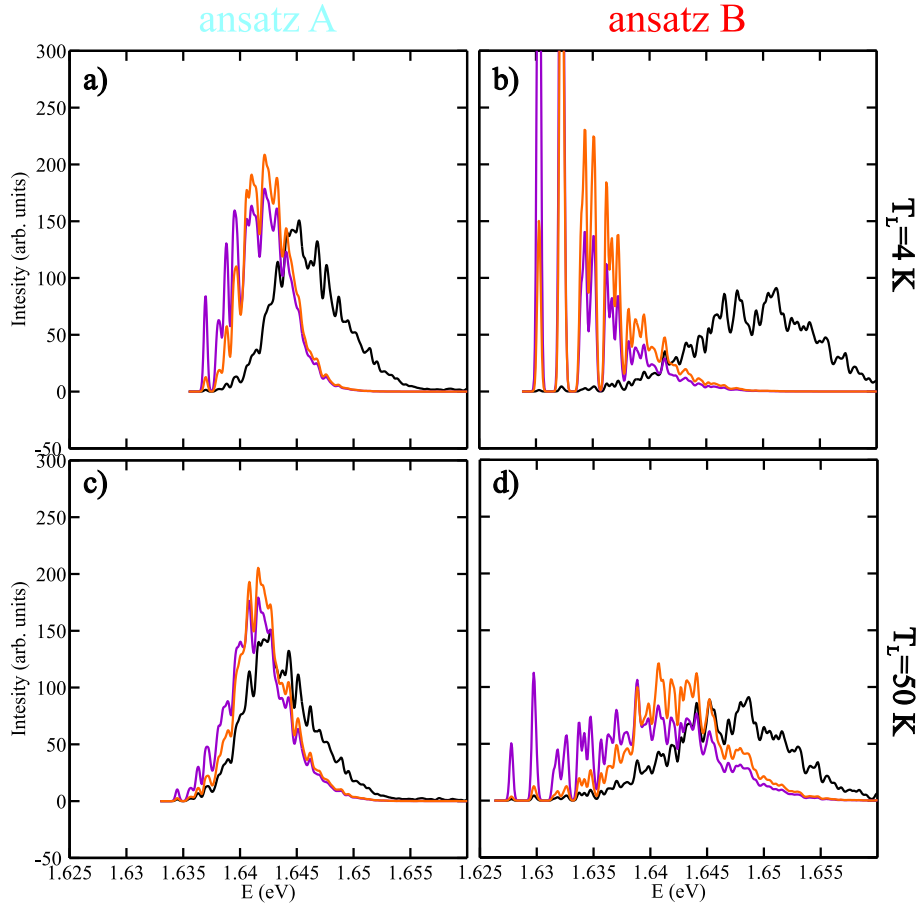


Figure 2.15: Calculated absorption spectra (black), PL spectra with thermal occupation (magenta) and quasi-thermal occupation (orange) for two temperatures $T_L = 4$ K (a and b) and $T_L = 50$ K (c and d) of the 4 nm wide quantum well. The sampled area for the absorption calculation (dashed) corresponds to the size of the optical focus in the experiment (600×600 nm²). The effective exciton temperature T_X was adjusted at high energy tail of the experimental PL (see text). Individual lines are Gaussian broadened with $\sigma_G = 0.15$ meV Eq. (C.8).

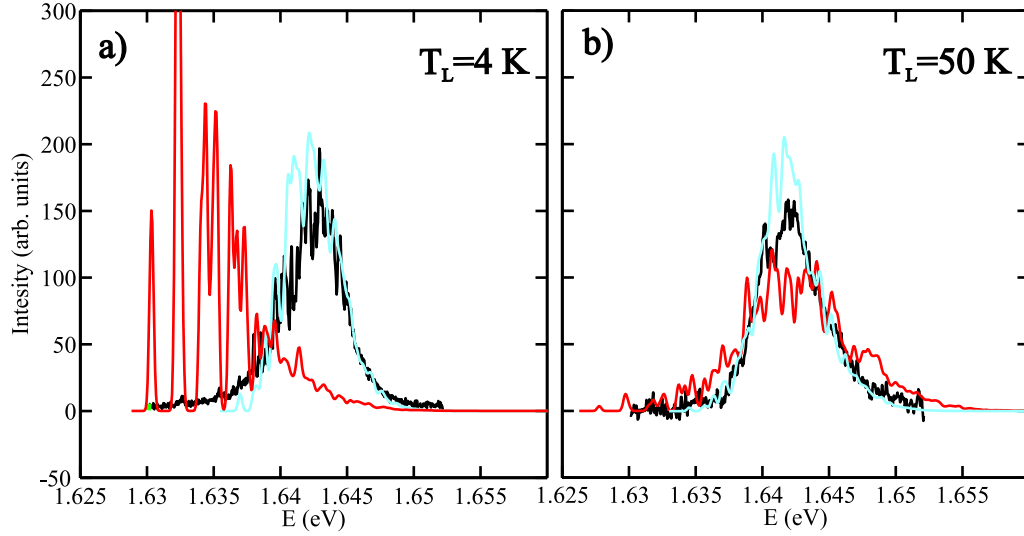


Figure 2.16: Comparison between measured μPL spectra (black) and calculated ones with quasi-thermal occupation (blue ansatz A and red ansatz B) for two temperatures $T_L = 4 \text{ K}$ a) and $T_L = 50 \text{ K}$ b) of the 4 nm wide quantum well. The same spot as in Fig. 2.12 is used. Other parameters same as in Fig. 2.15.

The comparison in the case of the ansatz B does not look so convincing since the absorption spectra is almost twice as wide as for the ansatz A. This is caused by the longer correlation length while the variance is kept fixed. Consequently, also the PL line is too wide and differences between thermal and quasi-thermal occupation become more pronounced. Since the absolute energetic position of the PL line is adjusted in order to obtain optimal agreement at $T = 50 \text{ K}$, it leads to clear disagreement at $T = 4 \text{ K}$. Nevertheless, the striking differences in Fig. 2.16 b) red should not be overevaluated since some discrepancies come from our assumption of the occupation function.

The comparison between simulated and measured μPL spectra cannot be regarded as a conclusive check of the validity and quality of our approach. In contrast, the diamagnetic shift provides such a check since here individual exciton states are studied. This is also the reason why the μPL measurement with its sharp lines is superior to the broad and structureless far-field PL spectrum.

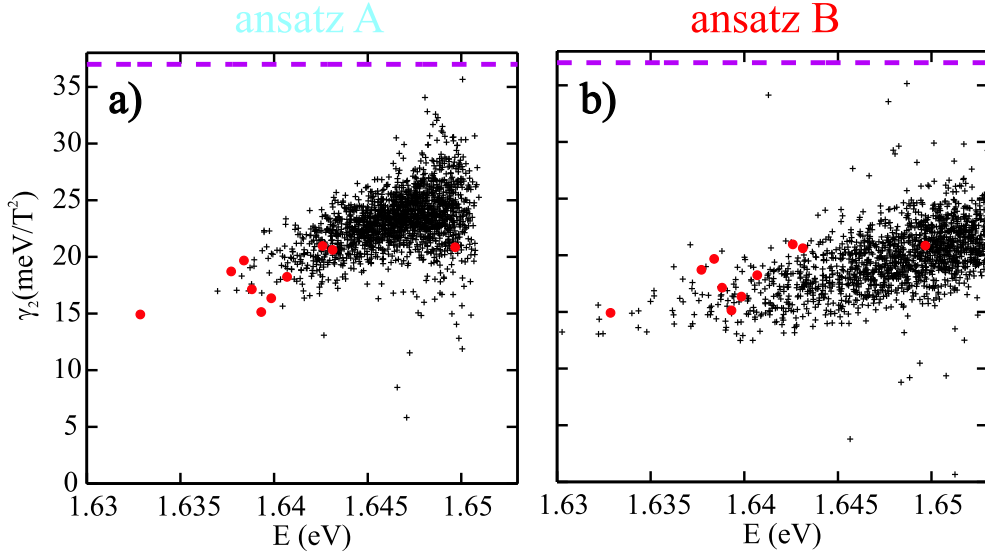


Figure 2.17: Diamagnetic shift coefficients of single exciton states in a 4 nm wide quantum well. Measured data (circles) are taken from Ref. [ERW⁺06] and compared with the calculation (crosses) of ansatz: A and B. The dashed line shows the theoretical value without disorder.

2.8.4 Diamagnetic shift coefficient

From the overall shift of the PL with magnetic field, a coefficient $\gamma_{tot} = 22 \mu\text{eV}/\text{T}^2$ in the present sample could be extracted. This is definitely below the calculated ideal value of $\gamma^{id} = 37 \mu\text{eV}/\text{T}^2$ which is marked in Fig. 2.17 as dashed horizontal line. We have to conclude again that the disorder-induced localization reduces the shift coefficient dramatically. The nice agreement between the measured and calculated data points in Fig. 2.17 could, however, not be achieved before the enhanced electron mass was included (see Sec. 2.7).

Previous magnetoluminescence experiments [TOIM84; RSN⁺86; SAS95] on a 5 nm wide quantum well gave an average diamagnetic coefficient of the PL line $25 \mu\text{eV}/\text{T}^2$ which is comparable to the range found in the present experiment. Furthermore, the role of an enhanced reduced mass for the γ_α has been recognized early on [SDL⁺89] but the localization caused by disorder was not discussed.

In the experiment, γ_α has been extracted by averaging over the Zeeman doublet. Reliable data, however, can be determined only for states deep in the tail, and having an oscillator strength large enough. Only a few states fulfil these criteria, which reduces the statistics significantly. In the simulation, such a problem does not exist and relevant statistics can be obtained. Very good agreement between theoretical and experimental results (measured on

the same sample but on a different spot) is seen in Fig. 2.17. In the present case the ansatz B gives better agreement than A since the deep tail states have higher probability (nonetheless their absolute energetic position is fixed by PL at $T = 50$ K).

An interesting new feature seen in Fig. 2.17 is the increase of the γ_α *distribution width* with energy. An intuitive explanation is as follows: The most strongly localized states are found in deep minima which have a very narrow distribution of curvatures and depths, which is theoretically predicted by the optimum fluctuation theory [Run02]. On the contrary, less localized states average over a larger area, and find a wide variety of potential shapes. The potential distributions maps directly to the diamagnetic shift. Similar relations exist for the oscillator strength distribution, which have been explored before [LRZ03].

The extracted small correlation lengths show that spatial correlations extend mostly over only few atomic distances. The correlation length may seem unexpectedly short in the case of ansatz A. However, the dominant contribution to the disorder in this structure, grown without growth interruptions, is certainly on the order of 1 nm and below. Additional experimental and theoretical work will be necessary to resolve finer details of the correlation and to conclude which fit ansatz is more appropriate.

On the theoretical side, one could employ a more sophisticated interpretation of the XSTM images beyond the linear scaling, e.g., with a density functional approach, and taking into account the STM-tip correlation. Experimentally, even larger XSTM topographs could in the future improve the statistics on longer correlations and optimally the three-dimensional data would be desirable. For the present work, single and double exponential averaging functions have turned out to be sufficient to obtain convincing agreement between the theoretical computations and the experimental data.

Part III

Exciton in Quantum Ring

Chapter 3

Quantum Ring

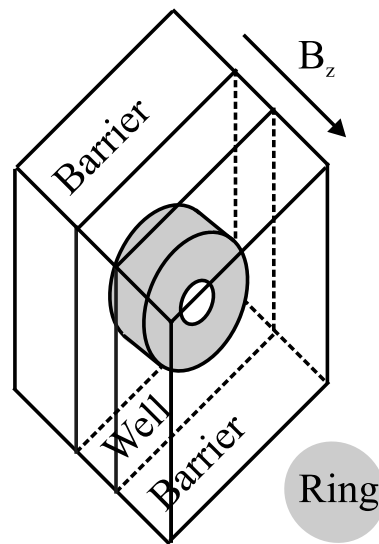


Figure 3.1: Schematic drawing of the investigated nanoring embedded in the quantum well

This chapter is devoted to the properties of the exciton in structures where electron and hole are not only confined in the growth direction but also in the xy -plane, and are subject to an applied perpendicular magnetic field. An example of such a structure, a circular quantum ring embedded in the quantum well, is shown in Fig. 3.1. Before we start to work with the Hamiltonian Eq. (2.2) we may notice that the main difference to the previous chapter is that the in-plane confining potential $W_a(\mathbf{r}_a)$ (either for electron or hole) will have a local maximum at the origin $\mathbf{r}_a = 0$ and minimum at $\mathbf{r}_a = r_0$. These potential properties may force the exciton wave function to

have a form of a closed loop. Such a shape of the wave function is called non-trivial or connected topology. This topology is especially sensitive to the perpendicular magnetic field since it tries to rotate the carriers (electron and hole in opposite directions). In the case of a trivial topology electron and hole rotate around themselves while for a connected topology they can orbit through the ring shaped potential.

As has been already mentioned in the introduction, the Aharonov-Bohm effect which requires the non-trivial topology of the wave function is found only for charged particles. However, the exciton being a composite particle consisting of electron and hole, has zero total charge. Theoretical studies on the basis of a simplified model (zero width of the nanoring) [Cha95; RR00; MC04; CM05; dSUS05; BPSP06] have demonstrated that the exciton Aharonov-Bohm effect (X-ABE), i. e. an oscillatory component in the energy exists.

Let us investigate it more precisely.

3.1 Hamiltonian

Assuming that the nanoring is embedded in a narrow quantum well, the exciton Hamiltonian Eq. (2.2) can be adopted replacing the disorder potential $W_a(\mathbf{r}_a)$ with the lateral confinement $V_a(r_a, \phi_a)$. The separation of the wave function Eq. (1.64) can be directly adopted. Using the symmetric one-particle Coulomb gauge of the vector potential: $\mathbf{A}(\mathbf{r}) = \frac{1}{2}\mathbf{B} \times \mathbf{r}$ (see appendix B for details) the single-exciton Hamiltonian Eq. (2.2) (consider also Eq. (1.72)) is rewritten in electron-hole polar coordinates in the following way

$$\begin{aligned} \hat{H} = & \sum_{a=e,h} \left[V_a(r_a, \phi_a) - \frac{\hbar^2}{2m_a} \frac{1}{r_a} \frac{\partial}{\partial r_a} \left(r_a \frac{\partial}{\partial r_a} \right) \right. \\ & \left. + \frac{1}{2m_a r_a^2} \left(-i\hbar \frac{\partial}{\partial \phi_a} - q_a \frac{eB}{2} r_a^2 \right)^2 \right] + V_C(r_e, r_h, \phi_e - \phi_h). \end{aligned} \quad (3.1)$$

We use the Jacobi coordinates with convenience since the Coulomb potential is a only function of the angle difference

$$\phi = \phi_e - \phi_h, \quad \Phi = \frac{1}{2}(\phi_e + \phi_h), \quad (3.2)$$

$$\phi_e = \Phi + \frac{1}{2}\phi, \quad \phi_h = \Phi - \frac{1}{2}\phi, \quad (3.3)$$

$$\frac{\partial}{\partial \phi_e} = \frac{\partial}{\partial \phi} + \frac{1}{2} \frac{\partial}{\partial \Phi}, \quad \frac{\partial}{\partial \phi_h} = -\frac{\partial}{\partial \phi} + \frac{1}{2} \frac{\partial}{\partial \Phi}, \quad (3.4)$$

where ϕ (Φ) is the relative (average) angle. The Hamiltonian Eq. (3.1) transforms to

$$\hat{H} = \sum_{a=e,h} \left[-\frac{\hbar^2}{2m_a} \frac{1}{r_a} \frac{\partial}{\partial r_a} \left(r_a \frac{\partial}{\partial r_a} \right) + \frac{1}{2m_a r_a^2} \left(i\hbar \left[\frac{\partial}{\partial \phi} \pm \frac{1}{2} \frac{\partial}{\partial \Phi} \right] - \frac{eB}{2} r_a^2 \right)^2 + V_a(r_a, \Phi \pm \frac{1}{2}\phi) \right] + V_C(r_e, r_h, \phi). \quad (3.5)$$

The exciton wave function is expanded into the basis of angular momentum eigenfunctions

$$\Psi_\alpha(r_e, r_h, \phi, \Phi) = \sum_{l,L} u_{l,L,\alpha}(r_e, r_h) e^{il\phi} \frac{e^{iL\Phi}}{2\pi}. \quad (3.6)$$

Taking into account the azimuthal boundary conditions which have the usual form of

$$\Psi_\alpha(r_e, r_h, \phi_e, \phi_h) = \Psi_\alpha(r_e, r_h, \phi_e + 2\pi, \phi_h) = \Psi_\alpha(r_e, r_h, \phi_e, \phi_h + 2\pi), \quad (3.7)$$

and the expansion Eq. (3.6), we find the rule how l depends on L :

$$L \text{ even: } l \text{ integer; } \quad L \text{ odd: } l \text{ half integer.} \quad (3.8)$$

The coupled equations for the expansion functions $u_{l,L,\alpha}(r_e, r_h)$ can be derived straightforwardly. First, we investigate the confining potential matrix elements

$$\begin{aligned} \langle lL | V_a(r_a, \phi_a) | l'L' \rangle &= \delta_{l-l', \pm \frac{L-L'}{2}} V_{L-L'}^a(r_a), \\ V_k^a(r_a) &= \frac{1}{2\pi} \int_0^{2\pi} d\phi_a V_a(r_a, \phi_a) e^{ik\phi_a}, \end{aligned} \quad (3.9)$$

and from the reality of the $V_a(r_a, \phi_a)$ follows $V_k^a = (V_{-k}^a)^*$.

The confining potential can have an arbitrary symmetry (see Fig. 3.2 for examples) which is classified by the two-dimensional point groups. There are two types of them: (i) C_n which consists of all rotations about a fixed point by multiples of the angle $2\pi/n$ and (ii) D_n which consist of the rotations in C_n together with reflections in n axes that pass through the fixed point. In order to derive symmetry properties of $V_k^a(r_a)$ depending on the point group of the potential let us assume that the potential $V_a(r_a, \phi_a)$ is invariant to the rotation by $\phi = \frac{2\pi}{n}$. Changing the variable in the integrand of the Eq. (3.9) by $\phi'_a = \phi_a + \frac{2\pi}{n}$ we obtain

$$V_k^a(r_a) = \frac{1}{2\pi} \int_0^{2\pi} d\phi_a V_a(r_a, \phi_a) e^{ik(\phi_a + \frac{2\pi}{n})}. \quad (3.10)$$

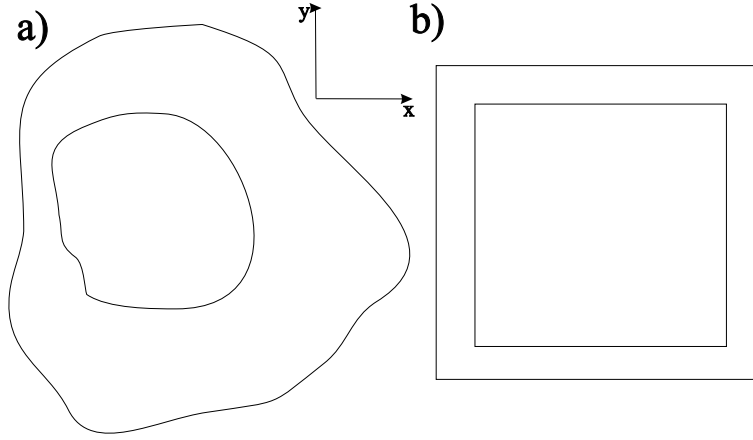


Figure 3.2: Schematic picture of the quantum rings with the C_1 a) and D_4 b) symmetry.

Table 3.1: The symmetries of the in-plane potential and matrix elements V_k Eq. (3.9).

Point group of the potential	Symmetry of V_k
C_n	$V_k \neq 0, k = jn, j$ integer
D_n	$V_k = V_{-k} \neq 0, k = jn, j$ integer
$O(2)$	$V_k = V_0 \delta_{k,0}$

This should be identical to Eq. (3.9) which implies that only elements with $k = jn$, j being integer, are non-zero. Adopting similar arguments it can be proven that the existence of inversion symmetry implies $V_k^a = V_{-k}^a$. The symmetry properties are summarized in Tab. 3.1.

In the case of the lowest symmetry (C_1) the matrix of V_k^a cannot be separated into block matrices since generally all V_k^a are non-zero. As the symmetry is increased (C_n or D_n) the matrix can be separated into n block matrices, which means that the matrix elements $V_{LL'}$ are non zero only if $L - L' = n$ is fulfilled. In the limiting case of $n \rightarrow \infty$ the point groups C_n and D_n are identical¹ and form point group of the circle $C_\infty = D_\infty = O(2)$ with infinitely many block matrices.

Second, we look upon the Coulomb potential matrix elements which are

¹This is only true in two dimensions. The continuous limit of C_n is the *proper* symmetry group of the circle $SO(2)$ consisting of all rotations about a fixed point. Such a point group cannot be visualized. The continuous limit of D_n is $O(2)$, the symmetry group of the circle, consisting of all rotations about a fixed point and reflections in any axis through that fixed point.

diagonal in L

$$\begin{aligned}\langle lL|V_C(r_e, r_h, \phi)|l'L'\rangle &= \delta_{LL'}\tilde{V}_C^k(r_e, r_h), \\ \tilde{V}_C^k(r_e, r_h) &= \frac{1}{2\pi} \int_0^{2\pi} V_C(r_e, r_h, \phi) \cos(k\phi) d\phi, \quad (3.11)\end{aligned}$$

and finally the Hamiltonian can be written down

$$\begin{aligned}\langle lL|\hat{H}(r_e, r_h, \phi, \Phi)|l'L'\rangle &= \\ \delta_{ll'}\delta_{LL'} \sum_{a=e,h} \left[-\frac{\hbar^2}{2m_a} \left(-\frac{1}{r_a} \frac{\partial}{\partial r_a} \left(r_a \frac{\partial}{\partial r_a} \right) + \frac{1}{r_a^2} \left(l \pm \frac{L}{2} + \frac{eB}{2} r_a^2 \right)^2 \right) \right] \\ + \delta_{l-l', \frac{L-L'}{2}} V_{l-l'}^e(r_e) + \delta_{l-l', \frac{L-L'}{2}} V_{l-l'}^h(r_h) + \delta_{LL'} \tilde{V}_C^{l-l'}(r_e, r_h). \quad (3.12)\end{aligned}$$

Introducing the expansion Eq. (3.6), the exciton oscillator strength M_α of Eq. (1.53) simplifies to

$$M_\alpha = \sum_l \int_0^\infty u_{l,0,\alpha}(r, r) r dr. \quad (3.13)$$

Therefore, only the component with $L = 0$ contributes to the oscillator strength.

In the following, the wave function of the state α is analyzed studying the correlated one-particle densities

$$n_\alpha^{(e)}(r_e, \tilde{\phi}) = r_e \int dr_h r_h \left| \psi_\alpha \left(r_e, r_h, \phi = \tilde{\phi}, \Phi = \frac{\tilde{\phi}}{2} \right) \right|^2, \quad (3.14)$$

$$n_\alpha^{(h)}(r_h, \tilde{\phi}) = r_h \int dr_e r_e \left| \psi_\alpha \left(r_e, r_h, \phi = -\tilde{\phi}, \Phi = \frac{\tilde{\phi}}{2} \right) \right|^2, \quad (3.15)$$

for which the angular position of the second particle is fixed at say $\phi_a = 0$. Another possibility would be to fix the r_a coordinate instead of integrating over r_a . In the case of strong confinement in the ring both approaches are equivalent.

3.2 Persistent current and magnetization

Even though the exciton is a neutral particle, it can possess a current at a finite B -field: electron and hole orbit in the nanoring under the B -field in opposite directions, and since they have opposite signs of their charges, their current contributions do add.

The one-particle current density operator at position \mathbf{r} is defined as

$$\hat{\mathbf{J}}_a(\mathbf{r}) = \frac{q_a}{2m_a} [(\hat{\mathbf{p}}_a - q_a e \mathbf{A}(\mathbf{r}_a)) \delta(\mathbf{r}_a - \mathbf{r}) + \delta(\mathbf{r}_a - \mathbf{r}) (\hat{\mathbf{p}}_a - q_a e \mathbf{A}(\mathbf{r}_a))].$$

The expectation value of the radial current $\hat{J}_{a,r}$ is nonzero only for continuum states and will not be discussed further. In the present case, the azimuthal current $\hat{J}_{a,\phi}(r, \phi) \mathbf{e}_\phi$ takes the form

$$\begin{aligned} \hat{J}_{a,\phi}(r, \phi) = & \frac{q_a}{2m_a} \left[\left(-i\hbar \frac{1}{r_a} \frac{\partial}{\partial \phi_a} - \frac{q_a e B r_a}{2} \right) \frac{\delta(r - r_a)}{r} \delta(\phi - \phi_a) \right. \\ & \left. + \frac{\delta(r - r_a)}{r} \delta(\phi - \phi_a) \left(-i\hbar \frac{1}{r_a} \frac{\partial}{\partial \phi_a} - \frac{q_a e B r_a}{2} \right) \right]. \end{aligned} \quad (3.16)$$

The total exciton current consists of the electron and hole ones, which have to be added and integrated over the cross section of the nanoring,

$$I_\alpha = \int_0^\infty dr \langle \alpha | \hat{J}_{e,\phi}(r, \phi) + \hat{J}_{h,\phi}(r, \phi) | \alpha \rangle. \quad (3.17)$$

Since the operator Eq. (3.16) is not an explicit function of ϕ_a there is no dependence of $\langle \alpha | \hat{J}_{a,\phi}(r, \phi) | \alpha \rangle$ on ϕ as can be easily checked taking the expansion Eq. (3.6). Consequently, the total current I_α is independent of angle ϕ in accordance with Kirchhoff's laws of current conservation.

The one-particle magnetization operator is defined as

$$\hat{\mathbf{M}}_a(\mathbf{r}) = \frac{1}{2} \mathbf{r} \times \hat{\mathbf{J}}_a(\mathbf{r}). \quad (3.18)$$

The only nonzero expectation value of the magnetization which integrated over all space is directed along z and has the magnitude

$$M_\alpha = \pi \int dr r^2 \langle \alpha | \hat{J}_{e,\phi}(r, \phi) + \hat{J}_{h,\phi}(r, \phi) | \alpha \rangle. \quad (3.19)$$

With the expansion Eq. (3.6) the persistent current (PC) and the magnetization can be written explicitly as

$$\begin{aligned} I_\alpha = & \frac{e\hbar}{2\pi} \sum_{l,L} \int dr r \int dr' r' \left[\left(\frac{l + \frac{L}{2}}{r^2} - \frac{1}{2\lambda^2} \right) \frac{u_{l,L,\alpha}^2(r, r')}{m_e} \right. \\ & \left. + \left(\frac{l - \frac{L}{2}}{r^2} - \frac{1}{2\lambda^2} \right) \frac{u_{l,L,\alpha}^2(r', r)}{m_h} \right], \end{aligned} \quad (3.20)$$

$$\begin{aligned} M_\alpha = & \frac{e\hbar}{2} \sum_{l,L} \int dr r \int dr' r' \left[\left(l + \frac{L}{2} - \frac{r^2}{2\lambda^2} \right) \frac{u_{l,L,\alpha}^2(r, r')}{m_e} \right. \\ & \left. + \left(l - \frac{L}{2} - \frac{r'^2}{2\lambda^2} \right) \frac{u_{l,L,\alpha}^2(r', r)}{m_h} \right]. \end{aligned} \quad (3.21)$$

Comparing Eq. (3.20) and Eq. (3.21), the difference is an additional factor πr^2 in the integrand of the magnetization. The expression for the magnetization can also be derived using the Hellmann-Feynman theorem

$$M_\alpha = -\frac{dE_\alpha(B)}{dB}. \quad (3.22)$$

3.3 Circular quantum ring

As a special case we investigate the case of the highest circular ($O(2)$) symmetry. A ring with such a high symmetry can not be probably grown but this assumption simplifies the problem a lot and enables to get a better insight. Due to the rotational invariance caused by the circular symmetry one degree of freedom may be factorized as follows from the principles of quantum mechanics. This is total angle motion as can be verified checking the commutator $[\hat{H}, -i\hbar\frac{\partial}{\partial\Phi}] = 0$. It follows also from Tab. 3.1 that only the matrix elements $V_0(r_a)$ contributes and this means that L is a good quantum number. The Hamiltonian Eq. (3.12) reduces thus to

$$\begin{aligned} \hat{H}_{LL'}^{ll'}(r_e, r_h) = & \delta_{LL'} \left\{ \delta_{ll'} \sum_{a=e,h} \left[\frac{\hbar^2}{2m_a} \left(-\frac{1}{r_a} \frac{\partial}{\partial r_a} \left(r_a \frac{\partial}{\partial r_a} \right) \right. \right. \right. \\ & \left. \left. \left. + \frac{1}{r_a^2} \left(l \pm \frac{L}{2} + \frac{eB}{2\hbar} r_a^2 \right)^2 \right) + V_a(r_a) \right] + \tilde{V}_C^{l-l'}(r_e, r_h) \right\}. \end{aligned} \quad (3.23)$$

and consequently the wave function expansion Eq. (3.6) to

$$\Psi_\alpha(r_e, r_h, \phi, \Phi) = \sum_l u_{l,\alpha}(r_e, r_h) e^{il\phi} \frac{e^{iL\alpha\Phi}}{2\pi}. \quad (3.24)$$

In order to derive analytical expression additional assumptions are required.

3.3.1 Zero width ring

In the limiting case of strong electron and hole confinement the wave function can be further factorized

$$\Psi_\alpha(\mathbf{r}_e, \mathbf{r}_h) = \psi_\alpha(\phi_e, \phi_h) f_e(r_e) f_h(r_h), \quad (3.25)$$

where $f_a(r_a)$ are one-particle confinement wave functions in the radial direction centered at R_a and the angle dependent part is expanded as in the previous expansions Eqs. (3.6) and (3.24)

$$\psi_\alpha(\phi, \Phi) = \sum_l c_l^\alpha e^{-il\phi} \frac{e^{iL\alpha\Phi}}{2\pi}. \quad (3.26)$$

Strong lateral confinement can be achieved either by combining materials with appropriate band alignments or by the inclusion of strain. After averaging the Hamiltonian Eq. (3.23) with functions $f_a(r_a)$ one gets a new Hamilton matrix

$$\hat{H}_{LL'}^{ll'} = \delta_{LL'} \left\{ \delta_{ll'} \left[\frac{\hbar^2}{2\mu_X R_X^2} \left(l + \frac{eB}{2\hbar} R_X^2 + \frac{L}{2} p \right)^2 + \frac{\hbar^2}{2(m_e R_e^2 + m_h R_h^2)} \left(\frac{eB}{2\hbar} (R_e^2 - R_h^2) - L \right)^2 \right] + \tilde{V}_C^{l-l'}(R_e, R_h) \right\}, \quad (3.27)$$

where R_X is an effective ring radius for the exciton and p is a phase shift

$$R_X^2 = \frac{R_e^2 R_h^2 (m_e + m_h)}{m_e R_e^2 + m_h R_h^2}, \quad p = \frac{m_h R_h^2 - m_e R_e^2}{m_h R_h^2 + m_e R_e^2}. \quad (3.28)$$

This Hamiltonian has been intensively studied by many authors since its introduction [Cha95; GUKW02; dSUG04; dSUS05; BPSP06]. The further simplification of the Coulomb potential to $\tilde{V}_C^k(R_e, R_h) = v_C$ (contact potential) enables an analytical solution with the transcendental equation for the ground state energy [RR00; MC04] and with a closed form for the absorption spectrum [CM05] using the Green's function technique.

Absorption

The approach of [CM05] can be illustrated extending it to the case of different electron and hole radii. First, the Hamiltonian Eq. (3.27) for $L = 0$ is rewritten into a more compact way with the contact potential

$$\hat{H} = T_X \left(-i \frac{\partial}{\partial \phi} + f_X \right)^2 + \gamma + v_C \delta(\phi), \quad (3.29)$$

where $T_X = \frac{\hbar^2}{2\mu R_X^2}$ is the kinetic energy, $f_X = \frac{\pi B R_X^2}{\Phi_0}$ magnetic flux and $\gamma = \frac{e^2 B^2 (R_e^2 - R_h^2)^2}{8(m_e R_e^2 + m_h R_h^2)}$ energy shift. Second, we consider the unperturbed Green's function of the Schrödinger equation with $v_C = 0$ which is usually defined as

$$(\hbar\omega + i0^+ - \tilde{H}_0) G_0(\phi, \phi', \omega) = \delta(\phi - \phi'). \quad (3.30)$$

Its solution can be found straightforwardly

$$G_0(\phi, \phi', \omega) = \frac{1}{2\pi} \sum_{n=-\infty}^n \frac{e^{in(\phi-\phi')}}{\hbar\omega + i0^+ - T_X(n + f_X)^2 - \gamma}, \quad (3.31)$$

and is given explicitly in a special case

$$G_0(0, 0, \omega) = \frac{1}{4T_X\beta^{1/2}} [\cot(\pi(f_X + \beta^{1/2})) - \cot(\pi(f_X - \beta^{1/2}))], \quad (3.32)$$

where $\beta = \frac{\hbar\omega - \gamma}{T_X}$. Considering further also the Coulomb interaction it can be shown using standard techniques of many body theory that the Dyson equation is fulfilled

$$G(\phi, \phi', \omega) = G_0(\phi, \phi', \omega) - v_C \int_0^{2\pi} G_0(\phi, \phi'', \omega) \delta(\phi'') G_0(\phi'', \phi', \omega), \quad (3.33)$$

with the solution

$$G(\phi, \phi', \omega) = G_0(\phi, \phi', \omega) - v_C \frac{G_0(\phi, 0, \omega) G_0(0, \phi', \omega)}{1 + v_C G_0(0, 0, \omega)}. \quad (3.34)$$

The optical interband polarization is the solution of the Eq. (1.48) (setting the electromagnetic field to one for simplicity)

$$(\hbar\omega + i0^+ - H)\mathcal{P}(\phi_e, \phi_h, \omega) = -d_{cv}\mathcal{U}\delta(\phi_e - \phi_h), \quad (3.35)$$

where \mathcal{U} is an overlap of radial and z -confinement wave functions

$$\mathcal{U} = \int dr r f_e(r) f_h(r) \int dz v_e(z) v_h(z). \quad (3.36)$$

The susceptibility is obtained calculating electron-hole overlap Eq. (1.50)

$$\chi(\omega) = |d_{cv}|^2 \mathcal{U}^2 \int_0^{2\pi} d\phi \mathcal{P}(\phi, \phi, \omega). \quad (3.37)$$

and comparing Eqs. (3.34) and (3.37) we get

$$\chi(\omega) = |d_{cv}|^2 \mathcal{U}^2 \frac{G_0(0, 0, \omega)}{1 + v_C G_0(0, 0, \omega)}. \quad (3.38)$$

The absorption being the imaginary part of $\chi(\omega)$ can be easily evaluated with the help of the Eq. (3.32).

Oscillatory component and persistent current

Let us turn our attention back to the angle dependent Coulomb potential. The total energy as a function of the magnetic field can be written as

$$E_\alpha(B) = E_\alpha(0) + \Delta E_\alpha^{(1)}(B) + \Delta E_\alpha^{(2)}(B), \quad (3.39)$$

where $\Delta E_\alpha^{(1)}(B)$ is a strictly periodic function of B with the period [Cha02]

$$B_P = \frac{2\hbar}{e} \frac{1}{R_X^2}, \quad (3.40)$$

and is called oscillatory component, and $\Delta E_\alpha^{(2)}(B)$ (the second term in the square brackets of Eq. (3.27)) is a parabolic function of the magnetic field with zero of the energy shifted to $B_{Z,L}$

$$B_{Z,L} = L \frac{2\hbar}{e} \frac{1}{R_e^2 - R_h^2}. \quad (3.41)$$

The persistent current induced by an exciton in state α (Eq. (3.20)) can be also obtained from a version of the Hellman-Feynman theorem after introducing the one-particle flux [WFK94; MC04] $\Phi_{B,\alpha} = \pi R_a^2 B$

$$I_\alpha = -\frac{\partial E_\alpha(\Phi_{B,e}, \Phi_{B,h})}{\partial \Phi_{B,e}} - \frac{\partial E_\alpha(\Phi_{B,e}, \Phi_{B,h})}{\partial \Phi_{B,h}}. \quad (3.42)$$

In the present case, however, this would call for a calculation of the problem in dependence on two different (fictitious) B -fields in $E_\alpha(\Phi_{B,e}, \Phi_{B,h})$. From the Hamiltonian Eq. (3.27) the exciton flux can be defined as

$$\Phi_{B,X} = \pi R_X^2 B, \quad (3.43)$$

and the exciton energy can be regarded as a function of the exciton flux $E_\alpha(\Phi_{B,X})$. It turns out that the exciton PC calculated from the definition Eq. (3.42) is equivalent to the derivative of the oscillatory component of the exciton energy only,

$$I_\alpha = -\frac{1}{\pi R_X^2} \frac{d\Delta E_\alpha^{(1)}(B)}{dB}. \quad (3.44)$$

This means that the term quadratic in B ($\Delta E_\alpha^{(2)}$) does not contribute to the PC. From the general definition of the magnetization Eq. (3.22) a relation between the magnetization and the PC can be found easily,

$$M_\alpha = \pi R_X^2 I_\alpha - \frac{d\Delta E_\alpha^{(2)}(B)}{dB}. \quad (3.45)$$

The second term is the intrinsic magnetization originating from the inner electron and hole motion in the exciton while the first one being proportional to the PC, is related to the non-trivial (connected) topology of the wave function. Only in the case of identical electron and hole radii, $R_e = R_h$, the PC and the magnetization are proportional, since the term $\Delta E_\alpha^{(2)}$ is absent.

3.3.2 Exciton Aharonov-Bohm effect

Overview

First, let us start with experiment where contradictory results are found: An ensemble of InP/GaAs type II quantum *dots* has been studied [RGWCMR04]. A theoretical explanation based on [KKG98] described below indicated some X-ABE oscillations in a single dot. However, in a very recent single dot experiment [dGGN⁺06] on InP/GaAs quantum dots (grown under different conditions) no oscillations have been observed.

In order to explain the experiment [RGWCMR04] the electron-hole interaction has been taken only as a perturbation since the strong parabolic confinement for electron in the quantum dot is assumed. The hole is found in the ring-like potential minimum with radius R_h due to the strain and Coulomb interaction. The total energy can be then expressed as

$$E_X = E_g + \sqrt{(\hbar\omega_0)^2 + (\hbar\omega_c/2)^2} + \frac{\hbar^2}{2m_h R_h^2} (l_h - f_h)^2, \quad (3.46)$$

where E_g is the bandgap energy including exciton binding energy, $\hbar\omega_0$ is the confinement energy of electron, $\omega_c = eB/m_e$ is the cyclotron frequency, l_h the hole angular momentum quantum number, and f_h is the hole magnetic flux in units of Φ_0 .

Unfortunately, the X-ABE in *nanorings* has not been observed yet in contrast to charged excitons (complex of exciton and electron) [BKH⁺03].

Theoretically, there are only few works that go beyond zero width ring [HZLX01; SU01; GBW02]. However, no oscillatory component of the energy $\Delta E_\alpha^{(1)}(B)$ has been confirmed for the ground state. Nevertheless, a recent calculation on two-dimensional annular lattices [PDER05] indicated that the X-ABE of the ground state for nanorings exists, but in this model the energy shift quadratic in the magnetic field was neglected.

Furthermore, several proposals have been made to improve the observability of oscillations, such as applying an electric field to separate electron and hole [MC03; ZZC05] or different confinements for electron and hole [GUKW02]. The effect of weak disorder or impurity scattering (in general losing the cylindrical symmetry) has been investigated with the result that optically non-active (dark) states can become bright ones [dSUG04; dSUS05]. This effect is also investigated in detail in Sec. 3.5.

Objectives

It is necessary to stress that it is *not* the aim of our work to model material properties with the most accurate description. Out of this reason some effects

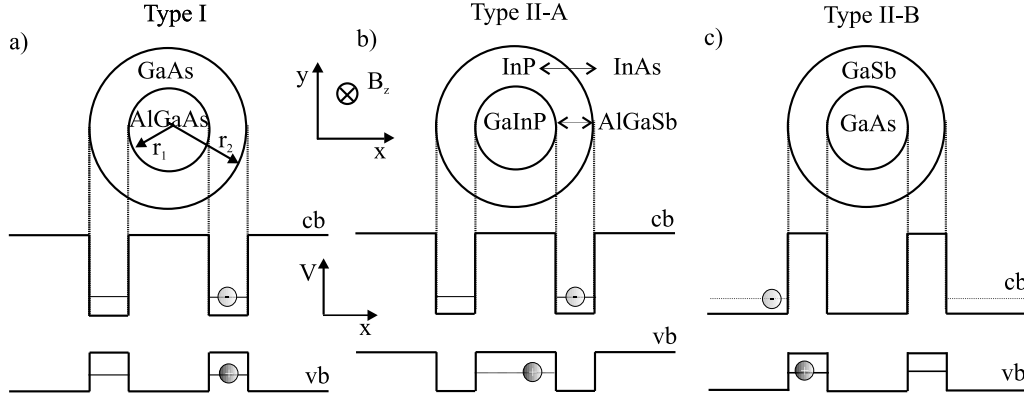


Figure 3.3: Schematic drawing of the investigated nanoring and the geometry within the x - y -plane: (a) type I, (b) type II-A, and (c) type II-B band alignment (see text). The magnetic field is directed along the growth direction z . Specific electron and hole positions (including strain) are visualized.

which may play an important role in selected materials, like piezoelectric fields, image charge effects, or even valence and conduction band mixing, are neglected.

We will investigate in what follows

- ◇ **Type I** nanoring, where the electron and the hole are confined together.
- ◇ **Type II-A** nanoring, where the electron is confined in the ring and the hole has a ring-like barrier.
- ◇ **Type II-B** nanoring, where the hole is confined in the ring and the electron has a ring-like barrier.

These are schematically shown in Fig. 3.3. The well and ring material parameters are summarized in Tab. A.1 and A.2 in the appendix A. The effective masses are chosen according to the material in which the particle is found predominantly.

In the investigation of the X-ABE we concentrate on *the optically active state with the lowest eigenenergy* E_α in this Section, since its proper confirmation in finite width nanorings represented an open question. We propose the following method for observing oscillations: *The second derivative of the energy with respect to the B-field.*

We have chosen B -field strengths up to $B = 25$ T which can be easily achieved in experiment. The strain calculation is described in detail in the appendix F.

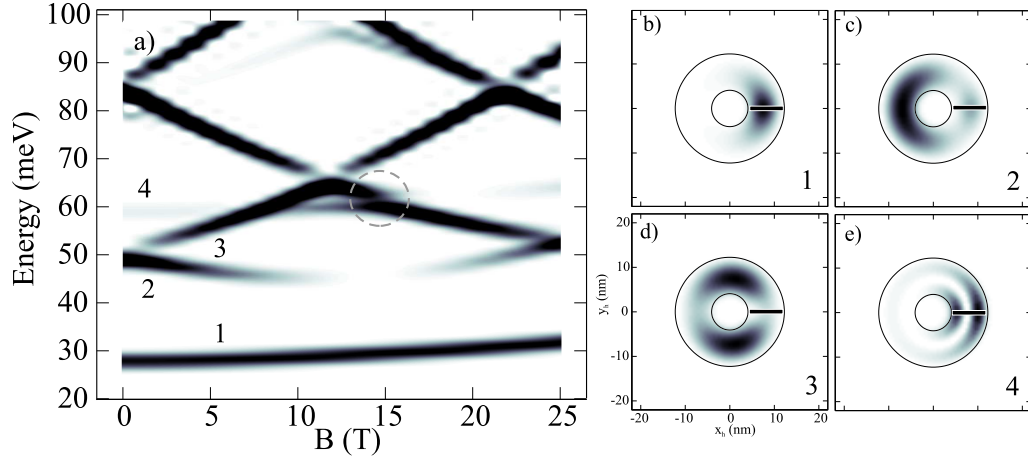


Figure 3.4: Absorption spectrum (a) of a GaAs/AlGaAs nanoring with radii $r_1 = 4$ nm and $r_2 = 12$ nm. The lines are Gaussian broadened with $\sigma = 1$ meV Eq. (C.8), and the oscillator strength (for the ground state divided by ten) is given in linear grey scale (step like features are artefacts of the interpolation). The circle focuses on the specific anti-crossing (see text). The correlated hole densities at $B = 2$ T are given for the first four lowest bright states (b)-(e). The black rectangle indicates the fixed electron position.

Type I: GaAs/AlGaAs

Structure: The choice of GaAs/AlGaAs for type I structure is rather straightforward since it is the most frequently investigated direct semiconductor. The strain can be safely neglected in this structure due to the small lattice mismatch.

This contrasts with previously investigated self-assembled InAs/GaAs nanorings [LLG⁺00; BWO04] which have been grown with an interesting method: First, InAs is grown on the Si doped GaAs substrate and dots are formed. Then, these dots are overgrown with thin layer of GaAs and annealed at the growth temperature. The drastic changes in the morphology due to the strain are observed when InAs escapes from the center and volcanos appear.

There is also a newly developed technique which allows to grow concentric GaAs/AlGaAs nanorings [KMO⁺05]. The rings are grown using modified droplet epitaxy. First, cation (Ga) atoms are supplied and their nanometersized droplets form. Then, the anion (As) atoms are supplied and according to its flux intensity either strain-free dots, rings or even double concentric rings are grown. The rings have almost circular symmetry.

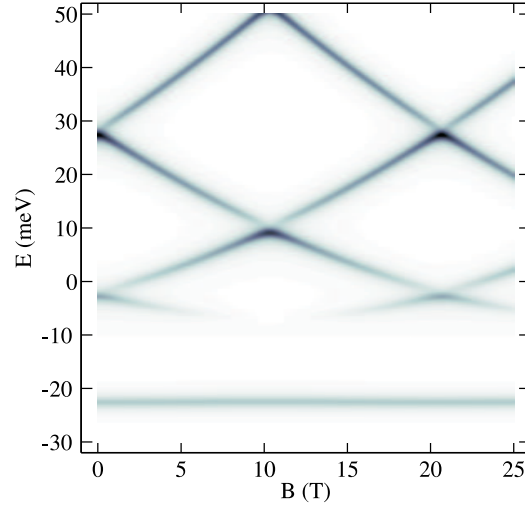


Figure 3.5: a) Absorption spectrum of the zero width nanoring ($r_e = r_h = 8$ nm). The lines are Gaussian broadened with $\sigma = 1$ meV Eq. (C.8), and the oscillator strength (for the ground state divided by ten) is given in linear grey scale.

The structure investigated here consists of a $\text{Al}_{0.23}\text{Ga}_{0.77}\text{As}$ 4 nm wide quantum well between $\text{Al}_{0.3}\text{Ga}_{0.7}\text{As}$ barriers. A nanoring of pure GaAs is placed inside the $\text{Al}_{0.23}\text{Ga}_{0.77}\text{As}$ well.

Absorption: As an example we discuss the absorption spectrum Eq. (1.54) of an GaAs/AlGaAs nanoring as plotted in Fig. 3.4a where the oscillations of the excited states are indeed clearly visible, while the ground state shows only a smooth and monotonic energy shift. Before discussing the properties of the lowest bright state we focus our attention to one interesting feature of excited states, namely the anti-crossing marked by a circle in Fig. 3.4. On a first glance, the absorption spectrum resembles the result of the simplified model (Fig. 3.5): The first three lowest bright states can also be found in the simplified model as plotted in Fig. 3.4b-d (being even, even and odd with respect to ϕ at $B = 0$ T). Only the fourth state (Fig. 3.4e) cannot be found in the simplified model since the hole is found in its first excited radial state, which is absent in a zero width ring. Its overlap with the electron part and consequently the oscillator strength is, however, tiny. Nevertheless, this even state manifests itself strongly by the anti-crossing with the next even state at around $B = 13$ T. This kind of anticrossing, even though somewhat marginal, goes beyond the description of the simplified model. From now on, let us concentrate on the lowest bright state.

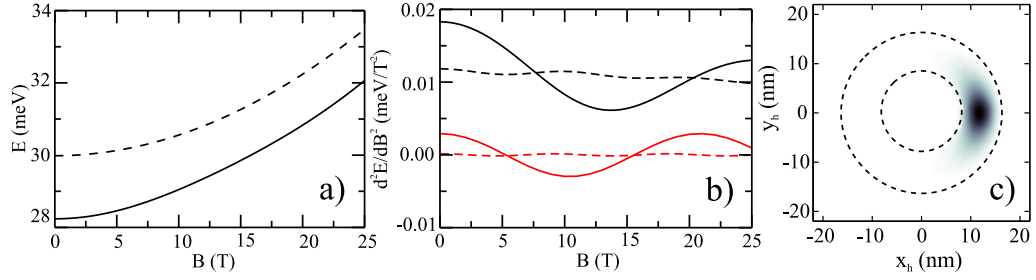


Figure 3.6: The B -field dependence of lowest bright (ground) state energy (a) and its second derivative in type I GaAs/AlGaAs nanorings, solid - $r_1 = 4$ nm, $r_2 = 12$ nm, and dashed - $r_1 = 8$ nm, $r_2 = 16$ nm. The full calculation (black) is compared to results for infinitesimal narrow rings Eq. (3.27) (red). The periods of the oscillations Eq. (3.40) are $B_P = 20.8$ T (solid) and $B_P = 9.2$ T (dashed). Projected hole density $n^{(h)}$ according to Eq. (3.15) at $B = 0$ T (c). The ring boundaries are shown as dashed circles.

Results: Up to now there has not been any clear evidence of oscillations of the lowest bright (ground) state for finite width nanorings. The problem becomes evident looking at Fig. 3.6a, where on the first glance the only dependence of the energy on the B -field is the smooth and monotonic increase. Although for nanorings of finite width a separation of the diamagnetic shift like Eq. (3.39) is not possible in a strict sense, we will understand in the following $\Delta E_\alpha^{(1)}$ as the oscillating part and $\Delta E_\alpha^{(2)}$ as the smooth monotonic part ($L_\alpha = 0$). The behavior of the exciton ground state energy in the limit $B \rightarrow 0$ has been studied in Ref. [WR98] finding a non-trivial dependence on the one-particle confinement and exciton relative motion. In the present case, the strong electron (hole) ring confinement fixes the electron (hole) radial position $r_{e(h)}$ and the strong Coulomb interaction fixes the relative distance r , which means that the quadratic dependence on B and consequently its contribution to the second derivative are almost constant with the B -field. This enables to extract the second - oscillatory - component from the second derivative as seen in Fig. 3.6b.

The strong dependence of the oscillations amplitude on the ring radius is remarkable. The expectation values of $R_a^2 = \langle r_{e(h)}^2 \rangle$ at $B = 0$ T from the full solution were used as input parameters in the simplified model. A comparison of the simplified with the full model shows good agreement for the period and the amplitude of the oscillations, and its strong dependence on the ring radius as well. The main difference is the absence of the term $\Delta E_\alpha^{(2)}$ in the simplified model. It is the finite radial extension of the exciton relative wave function (plotted in Fig. 3.6c) which gives a nonzero contribution to this

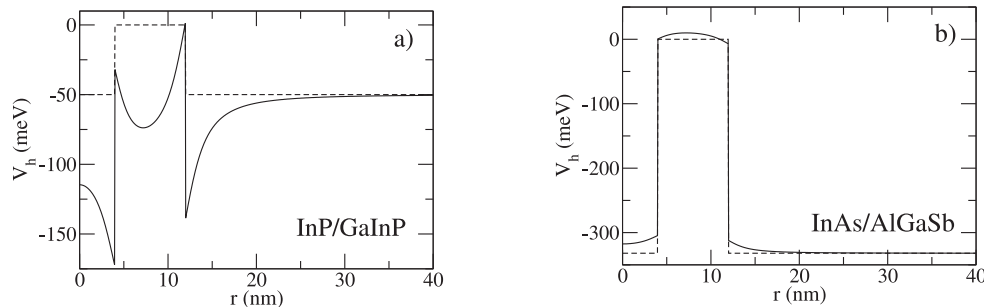


Figure 3.7: The hole potential in the x - y -plane for $z = 0$ of the InP/GaInP (a) and InAs/AlGaSb (b) nanorings without (dashed) and with (solid) strain included.

energy. After having compared results of both models in this case, further we will discuss only the full solution. Note, however, that the period Eq. (3.40) gives generally a good estimate.

Let us direct our attention to type II systems where more pronounced effects are expected.

Type II-A: InP/GaInP

Structure: InP/GaInP self-assembled quantum dots have been investigated since many years both theoretically and experimentally (see [PHJ⁺05] and references therein). Possibly, rings may be grown as well, e. g. using the same procedure as for InAs/GaAs [GMRS⁺97] or GaAs/AlGaAs [KMO⁺05] nanorings. We have investigated a structure consisting of a 4 nm wide $\text{Ga}_{0.51}\text{In}_{0.49}\text{P}$ quantum well between AlAs barriers. The nanoring is pure InP. Such a structure guarantees that the hole is always found around the ring (in the xy -plane) and not above or below the ring (in growth (z -) direction). This is not a necessary condition for the X-ABE. The situation where the hole (electron) is found above or below is also of interest. This goes beyond the scope of our work since we would not be able to take advantage of the z -separation. The strain plays an important role in this material [JPP03], as is clearly shown in Fig. 3.7a.

Results: Since the deep minimum of the hole potential is formed at the inner edge of the ring (Fig. 3.7a), the hole is found there. Such a state is named *hole-in* (depicted in Fig. 3.8c). The effective electron-hole separation is thus decreased with respect to the strain-free case. The state hole-in is the ground state for any ring radius. Excluding composition changes, the

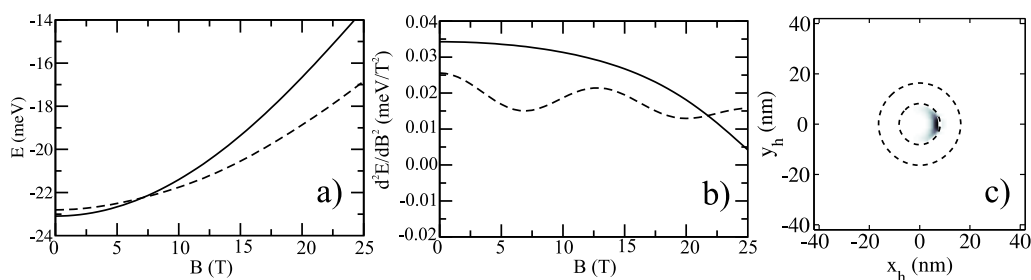


Figure 3.8: The B -field dependence of lowest bright state energy (a) and its second derivative (b). Solid - $r_1 = 4$ nm, $r_2 = 12$ nm, and dashed - $r_1 = 8$ nm, $r_2 = 16$ nm InP/GaInP nanoring. The solid line in (a) is shifted by 20 meV for comparison. Projected hole density $n^{(h)}$ according to Eq. (3.15) at $B = 0$ T (c). The ring boundaries are shown as dashed circles. The periods of the oscillations Eq. (3.40) are $B_P = 40.9$ T (solid) and $B_P = 11.8$ T (dashed).

height of the ring-like barrier for the hole can decrease by changing the well width in the z direction. For high B -fields, a transition from type II to type I may occur due the enhanced penetration of the hole wave function into the ring. This has been already predicted for quantum dots in Ref. [JPP03]. The energy of the lowest bright states as a function of B -field is plotted in Fig. 3.8a. Again, no evidence of oscillations is seen by the naked eye. The analysis of the second derivative (Fig. 3.8b) reveals that (i) the amplitude of the oscillation is increased compared to type I (as expected), and (ii) the period of the oscillation is increased as well since the hole samples a smaller magnetic flux (see Eq. (3.40)) compared to type I.

Type II-A: InAs/AlGaSbAs

Structure: The InAs/AlGaSb system has several advantages for observing the X-ABE in type II-A systems compared to InP/GaInP as will be discussed below. This system is less known compared to GaAs/AlAs or InP/GaInP, but as a quantum well structure well-understood and used (see [OFO05] and references therein). Recently, InAs quantum dots on AlGaSb substrate have been grown [YAGO04]. The fact that $\text{Al}_{0.6}\text{Ga}_{0.4}\text{Sb}$ is an indirect semiconductor [AJJA83] is of less importance since the electron is found predominantly in InAs, which means that the approximation taking into account only the Γ point is sufficient. A problem is the small difference (0.083 eV) between the conduction band edge in InAs and the valence band edge in $\text{Al}_{0.6}\text{Ga}_{0.4}\text{Sb}$ [VMRM01]. The applicability of the effective mass approximation is questionable here [CTCL96]. Nevertheless, we believe as a first approximation [XCQ92] it can be adopted. The investigated structure con-

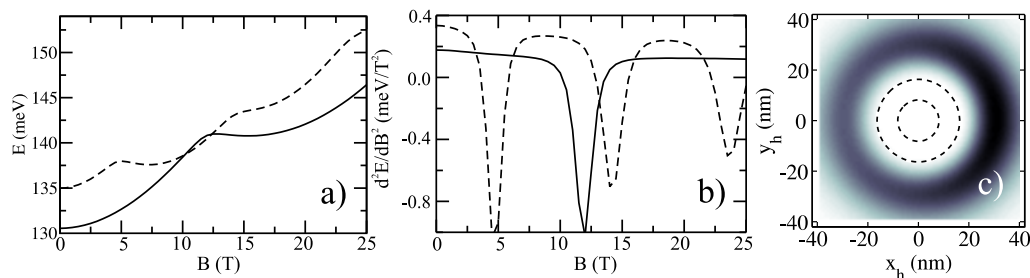


Figure 3.9: The B -field dependence of lowest bright state energy (a) and its second derivative (b). Solid - $r_1 = 4$ nm, $r_2 = 12$ nm, and dashed - $r_1 = 8$ nm, $r_2 = 16$ nm InAs/AlGaSb nanoring. Projected hole density $n^{(h)}$ according to Eq. (3.15) at $B = 0$ T (c). The ring boundaries are shown as dashed circles. The periods of the oscillations Eq. (3.40) are $B_P = 19.9$ T (solid) and $B_P = 8.8$ T (dashed).

sists of a $\text{Al}_{0.6}\text{Ga}_{0.4}\text{Sb}$ 4 nm wide quantum well between AlSb barriers. A InAs nanoring is placed in the $\text{Al}_{0.6}\text{Ga}_{0.4}\text{Sb}$ well. Even though the lattice mismatch between InAs and AlGaSb is small (1%), our calculation includes strain (see Fig. 3.7b).

Results: The influence of the strain on the hole potential for InAs/AlGaSb is shown in Fig. 3.7b. Compared to InP/GaInP, there are striking differences. The effect of strain is much smaller due to the much smaller lattice mismatch and the sign of the strain contribution is opposite. Instead of compression in the ring as for InP/GaInP (enlarging the bandgap), there is dilatation in the case of InAs/AlGaSb which lowers the bandgap. This leads to the repulsion of the hole from the ring and thus to a weakening of the Coulomb interaction. In contrast to InP/GaInP, the minimum of the hole potential is found outside of the ring (Fig. 3.7b) for any ring radius. The hole is found outside of the ring –*hole-out*– as depicted in Fig. 3.9c. The difference between the potential value in the middle and outside the ring decreases with increasing inner ring radius.

As stated above, due to its material properties a large oscillation amplitude is found here, as seen in Fig. 3.9a and b. Even without any further analysis, the lowest bright state, hole-out, shows clear oscillations. Please note a change of the scale by a *factor of ten* in Fig. 3.9b compared to Fig. 3.8b! In both cases kinks in $E(B)$ (sharp minima in d^2E/dB^2) resemble the one-particle ABE and are consequence of the weak Coulomb interaction.

An interesting new effect is found in larger rings, namely a transition from hole-in to hole-out. Depending on the ring geometry one of them is the

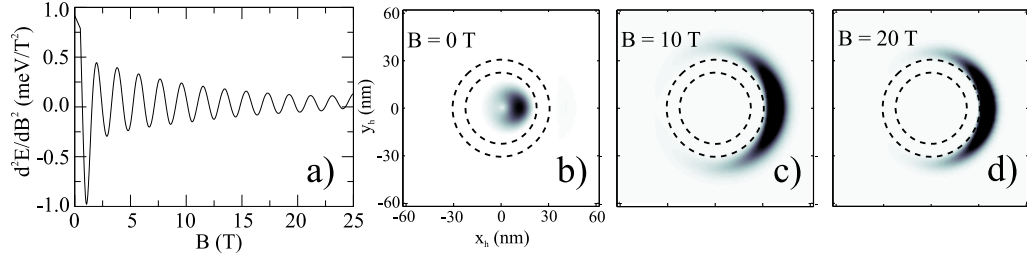


Figure 3.10: The second derivative with respect to the B -field of the lowest bright state energy (a) of the InAs/AlGaSb nanoring with radii $r_1 = 22$ nm and $r_2 = 30$ nm. Projected hole density $n^{(h)}$ according to Eq. (3.15) at $B = 0$ T (b), $B = 10$ T (c), and $B = 20$ T (d). The ring boundaries are shown as dashed circles. The period of the oscillations Eq. (3.40) is $B_P = 1.9$ T.

lowest bright state and the other one the second lowest. The strain profile favors the state hole-out. On the other hand, the Coulomb interaction prefers the state hole-in. As the strain profile in the middle and outside of the ring becomes similar for larger rings, the Coulomb interaction dominates and the state hole-in becomes the lowest bright state. This situation is demonstrated in Fig. 3.10b. The lowest bright state changes with increasing B -field: from hole-in (Fig. 3.10b) to hole-out (Fig. 3.10c and d). The state hole-in has a larger energy shift $\Delta E^{(2)}$, which can be verified by calculating the effective hole radii $\langle r_h^2 \rangle$ and checking the expression for $\Delta E_\alpha^{(2)}(B)$. The transition occurs at around $B = 1.5$ T. Since we always follow the lowest bright state the second derivative shows a sharp peak at the transition (Fig. 3.10a). We note that the small overlap of the hole-in and hole-out wave functions does not allow to distinguish between level crossing and anti-crossing, at least within our numerical precision. Due to the large radius of the ring, the oscillation period is small (according to Eq. (3.40) $B_P = 1.9$ T). The decay of the oscillation amplitude is due to a decrease in exciton Bohr radius with B -field (compare Fig. 3.10c and Fig. 3.10d).

Type II-B: GaSb/GaAs

Structure: GaSb/GaAs self-assembled quantum dots of type II-B have attracted a certain interest recently (see [TEL⁺04] and references therein). The strain plays a very important role in these structures and modifies significantly the conduction and valence band energies: The strain-free offsets $E_e = 0.063$ eV and $E_h = -0.77$ eV are modified to $E_e = 0.65$ eV and $E_h = -0.86$ (minimum). The substantial change of the electron potential is

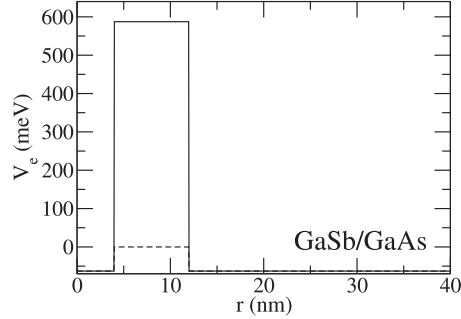


Figure 3.11: The electron potential in the x - y -plane for $z = 0$ of the GaSb/GaAs nanoring without (dashed) and with (solid) strain included.

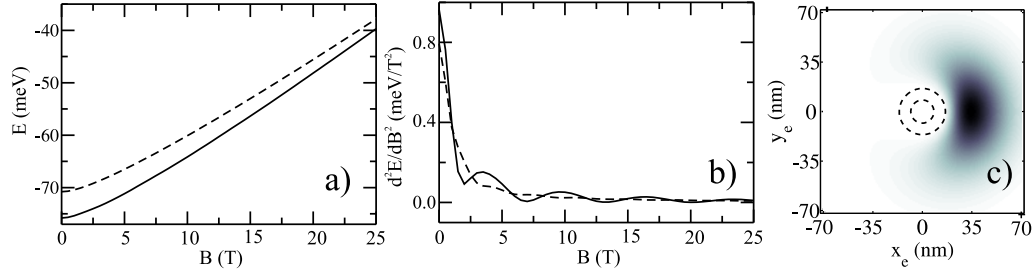


Figure 3.12: The B -field dependence of lowest bright state energy (a) and its second derivative (b). Solid - $r_1 = 4$ nm, $r_2 = 12$ nm, and dashed - $r_1 = 8$ nm, $r_2 = 16$ nm GaSb/GaAs nanoring. Projected electron density $n^{(e)}$ according to Eq. (3.14) at $B = 0$ T (c). The ring boundaries are shown as dashed circles. The periods of the oscillations Eq. (3.40) are $B_P = 2.9$ T (solid) and $B_P = 1.5$ T (dashed).

shown in Fig. 3.11. These results are comparable with those in Ref. [PP05]. The investigated structure consists of a GaAs 4 nm wide quantum well between $\text{Al}_{0.3}\text{Ga}_{0.7}\text{As}$ barriers, a GaSb nanoring is placed in the well.

Results: The increase of the lowest bright state energy by 40 meV from $B = 0$ T to $B = 25$ T (Fig. 3.12a) is large compared to all previous values and again no clue of oscillation is seen. In the second derivative (Fig. 3.12b), a sharp initial decay is revealed. The origin of this decay can be understood studying the wave function. The hole is strongly confined in this system and the electron potential has a high ring-like barrier as mentioned above. The correlated electron density plotted in Fig. 3.12c shows that the shallow Coulomb potential localizes the electron part of the wave functions only

weakly. The electron is very sensitive to the B -field. Due to the quadratic term $\Delta E^{(2)}$, the electron is forced to move quickly towards the hole (i. e. to the nanoring) with increasing B -field. This behavior leads to the initial decay in the second derivative (Fig. 3.12b). Later on, the wave function stabilizes and oscillations appear (Fig. 3.12b). Their amplitude is comparable to values found in InP/GaInP. The advantage of the GaSb/GaAs system is the large Bohr radius due to the large electron-hole separation. On the contrary, the disadvantage is the sensitivity of the electron to the B -field due to its small mass and shallow confinement.

Discussion

Now, we compare and discuss the results of the previous section and conclude which material combination is preferential for X-ABE.

Our results show unambiguously that a weakening of the Coulomb interaction increases the oscillation amplitudes, which has been already shown for the simplified model [GUKW02; dSUS05]. The reason is that electron and hole can sample the entire ring more easily if the exciton is weakly bound (larger exciton Bohr radius), and the wave function can acquire the necessary ring topology. The mutual confinement of electron and hole (type I) has turned out to be inferior to the systems where electron and hole are separated by the conduction and valence band alignments in the xy -plane (type II). One unwanted consequence of the spatial electron-hole separation is that the lowest bright state is not any more the ground state for larger B -fields [Cha02; GUKW02; BPSP06] (in contrast to type I). This may result e. g. in losses of photoluminescence intensity if some non-radiative decay channels are present. These kinetic effects are studied in the next Chapter.

Comparing the results for different material systems, we find that for large amplitude of X-ABE oscillations the ideal structure is of type II-A with the following properties: Light electron mass, strong electron confinement, and high barrier for holes. These criteria can be discussed qualitatively: (i) The light electron mass leads to a larger Bohr radius and higher probability of the particle to sample the whole nanoring. (ii) Strong electron confinement is needed in order to force the light electron to orbit around the ring. (iii) A high barrier for holes is necessary for a "good" type II nanoring, thus avoiding the penetration of the wave function into the ring. The material which matches these criteria best is InAs/AlGaSb in our case. This system clearly deserves further investigations, both theoretically and experimentally.

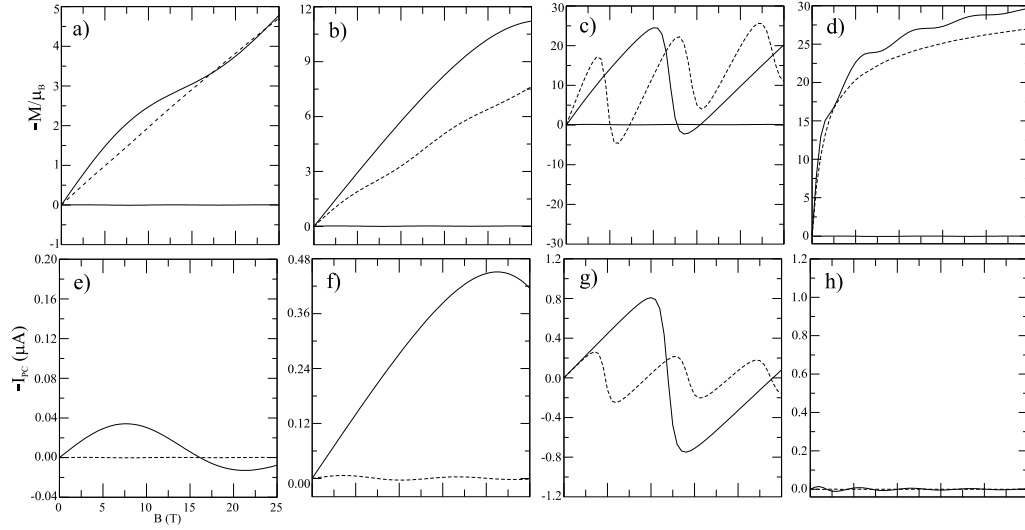


Figure 3.13: Magnetization (a - d) and persistent current (e - h) and of the nanorings with radii $r_1 = 4$ nm, $r_2 = 12$ nm (solid) and $r_1 = 8$ nm, $r_2 = 16$ nm (dashed) of the lowest bright state. Materials: GaAs/AlGaAs (a, e), InP/GaInP (b, f), InAs/AlGaSb (c, g), and GaSb/GaAs (d, h). The scaling factor between the PC and the magnetization is held constant in all cases. All curves are multiplied by minus one in order to see better the correspondence between magnetization and the first derivative of energy.

3.3.3 Persistent current and magnetization

After having examined the X-ABE in different materials, we investigate now the persistent currents and the magnetization in a more compact way.

The PC Eq. (3.20) and the magnetization Eq. (3.21) can be measured under special conditions: (i) The exciton should be excited into the optically active state (in our case always the lowest one). (ii) The excitation power should be sufficient in order to give a measurable signal but small enough to avoid exciton-exciton interaction. We assume one exciton per nanoring in the following, which corresponds to extremely strong excitation. A more realistic value of the excitation would reduce the scales in Fig. 3.13 accordingly. The state-of-the-art experimental technique (SQUID²) enables to measure the magnetization directly [MCB93]. The measurement of the

²Superconducting Quantum Interface Device uses the properties of electron-pair wave coherence and Josephson Junction (weak link between two superconductors) to detect very small magnetic fields. The typical geometry is the ring with two (or more) Josephson Junctions and the measured current is the function of the magnetic field threading the ring.

current requires additional contacts on the nanoring which may complicate the already difficult assembling of the nanorings even more. A measurement of either the persistent current or the magnetization in the nanoring is an extremely challenging task.

First, the magnetization of the exciton in the ring with finite width (Fig. 3.13a-d) can be divided roughly also into two contributions according to the analogy with the simplified model Eq. (3.45): The first (oscillatory) part comes from the orbiting of electron and hole around the nanoring while the second monotonic part (nearly linear in B) is related to the inner exciton motion where electron and hole orbit around each other. The weight of each contribution depends on the wave function topology. The dominance of the first contribution is seen only in the case of weak Coulomb interaction where the magnetization has even positive values (negative in the plot), i. e. pointing into the same direction of the B -field itself, thus behaving paramagnetically. Such an effect could be interesting for further applications, namely a sign switch of the optically induced coherent magnetization by the B -field. Unfortunately, this effect is rather weak. In all other cases both parts contribute with different weights. The linear component is found also for excitons in quantum wells or dots.

Second, the exciton PC shown in Fig. 3.13e-h exhibit periodic oscillations for each ring geometry and for all materials, even though the oscillation amplitude may be very small (as e. g. in Fig. 3.13d). The period and the relative amplitude of the oscillations agree well with those of the second derivative of the energy with respect to the magnetic field. Furthermore, the results confirm the relation Eq. (3.44) qualitatively also for finite width nanorings since they indeed remind of the first derivative of the oscillatory component of the exciton energy. A quantitative comparison is in general not possible since the smooth (non-oscillatory) component of the diamagnetic shift cannot be extracted unambiguously. From the theoretical point of view it turns out that a measurements of the PC would give a more direct information on the non-trivial ring topology of the wave function.

3.4 Circular quantum dot

Even though the nanoring is an ideal structure for the observation of either X-ABE or PC, there is an experimental observation backed by theoretical analysis [RGWCMR04] that excitons in InP/GaAs quantum dot of type II exhibit also X-ABE. Taking our approach we focus now our attention on this system.

The investigated quantum dot is schematically plotted in Fig. 3.14a).

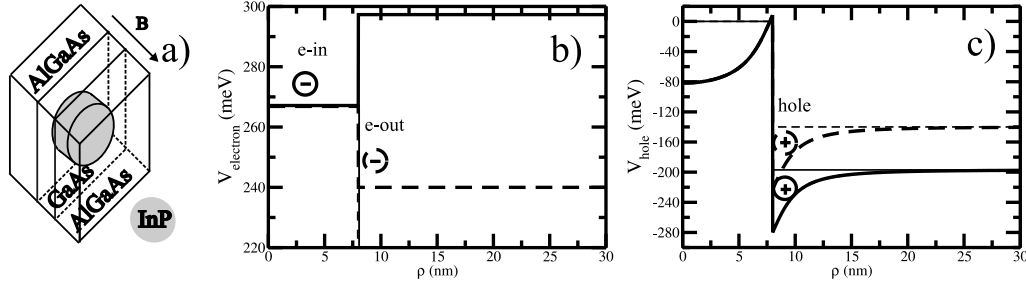


Figure 3.14: a) Schematic picture of the investigated geometry and materials, a buried InP dot in the GaAs/AlGaAs quantum well. b) (c): The electron (hole) band edges for the case *e-in* (solid) and the *e-out* (dashed) in ρ direction for $z = 0$. The chemical band offsets are shown as thin lines.

It consists of the cylindrical InP quantum dot placed inside a 4 nm wide AlGaAs/GaAs quantum well. The electron and heavy-hole band edges are shown in Fig. 3.14b) and c) (for details of the calculation see appendix F).

We consider two values for the chemical electron and hole band offsets of InP on GaAs: (a) $E_e = -0.297$ eV, $E_h = 0.197$ eV [dW89] and (b) $E_e = -0.240$ eV, $E_h = 0.140$ eV [VMRM01]. InP/GaAs without strain is a type II structure. If the strain is included, the two parameter choices lead to a quite different behavior: (a) the electron is confined in the dot with $\tilde{E}_e = -25$ meV called *e-in* (Fig. 3.14 solid), or (b) the dot acts as barrier for the electron, $\tilde{E}_e = 21$ meV called *e-out* (Fig. 3.14 dashed). Such a surprising result has been already predicted [PP05].

The main focus lies again on the behavior of the lowest bright exciton state with magnetic field. Such a state is also the ground state for zero magnetic field. In Fig. 3.15 correlated one-particle densities for hole and electron are plotted for *e-in* [a, b, c, d] and *e-out* [e, f, g, h] with dot radius of $r = 16$ nm. The electron part differs more: either the electron is confined in the dot (Fig. 3.15b) and d)) or outside the dot due to the Coulomb interaction with the hole (Fig. 3.15f) and h)).

As has been already pointed out in order to observe any oscillatory component of the energy on the B-field it is necessary that the wave function closes around the origin. The diameter of the dot has to be comparable with the exciton Bohr radius ($a_B = 9$ nm) to fulfil this condition. This condition is well fulfilled for *e-in* and for *e-out* only in the case of smaller dots.

In the investigated cases, the hole part of the wave function connects around the origin for both types when $r = 8$ nm and only for *e-in* when $r = 16$ nm. In the *e-in* and *e-out* structures, the heavier particle (hole, $m_h = 0.22$) has a ring-like confinement and the lighter one (electron) has not

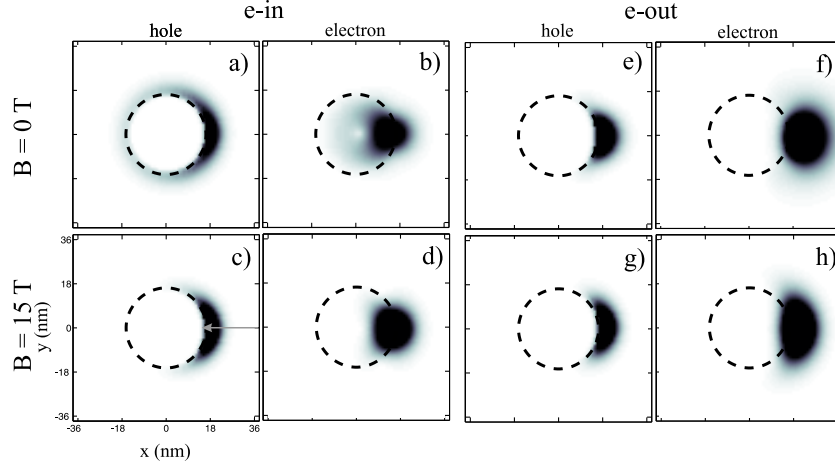


Figure 3.15: Correlated one-particle densities according to Eqs. (3.14) and (3.15) at $B = 0$ T [a, b, e, f] and $B = 15$ T [c, d, g, h] for e -in (see text) [a, b, c, d] and e -out [e, f, g, h] with $r = 16$ nm in Cartesian coordinates. The hole density [a, c, e, g] and the electron one [b, d, f, h] are shown. The dot boundaries are shown as dashed circles. The maximum value of the electron (hole) density is same in all cases. The grey arrow indicates the fixed position of the second particle.

only a very shallow one-particle potential but also a shallow ring-like potential due to the Coulomb interaction. Taking into account the small effective mass of the electron ($m_e = 0.077$), it can be concluded that the electron is more "delocalized" around the potential minima. This leads to the fact that the electron part of the wave function does not connect efficiently around the origin. Such a behavior is clearly visible in Fig. 3.15. Furthermore, with increasing B-field both particles move towards each other ($\langle r_e - r_h \rangle$ decreases) and even the hole loses its ring topology (Fig. 3.15c).

Absorption spectra with clear evidence of oscillations for higher states are plotted in Fig 3.16a) and b) for the case e -in. The calculated second derivatives for different configurations (see caption) are depicted in Fig. 3.16c). There are no clear oscillations seen. Due to the weak confinement of both particles, the second derivate of the non-oscillatory part decreases with B-field, and dominates the behavior completely.

Our results are not fully comparable with the experiments published in Ref. [RGWCMR04; dGGN⁺06] due to the additional confinement in the growth direction which we assume. But still some correspondence can be expected since the heavy-hole potential minimum originating from the strain is found around the dot and not above or below. This means that our in-plane

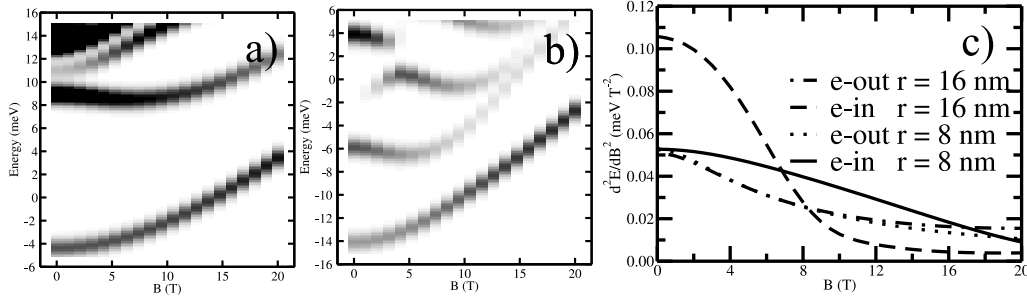


Figure 3.16: Absorption spectra for the case *e-in* with dot radius $r = 8$ nm (a) and $r = 16$ nm (b). In both cases the lines are Gaussian broadened with $\sigma = 0.52$ meV Eq. (C.8) and the oscillator strength (grey scale) is the same. Step-like features in the absorption are due to the finite resolution with respect to the magnetic field. c): The second derivative of the lowest bright states with respect to the magnetic field for *e-in* with strain (dashed-dotted $r = 8$ nm, dotted $r = 16$ nm) and *e-out* (solid $r = 8$ nm, dashed $r = 16$ nm).

model and its conclusions are to some extent applicable. The present results are in a rather good agreement with those published in Ref. [dGGN⁺06] where no oscillations have been seen. Since the experiment [dGGN⁺06] is performed on a single quantum dot, it is in a way superior to the ensemble measurements reported in Ref. [RGWCMR04]. Since the dots in the experiments are grown under different conditions, their shape and consequently the strain profile may differ significantly.

3.5 Non-circular quantum ring

We have treated the circular symmetry so far. Even though such a high symmetry is highly idealized it has given us an insight what X-ABE is and how it is related to the PC. Now we investigate a ring with D_1 symmetry as an example of low symmetry structure. There are many possibilities how this ring could look like. Here we study a model of the ring whose boundaries are two circles. The inner one is centered at the origin. The outer one is centered at point whose distance to the origin is b as indicated in Fig. 3.17. The potential has non-zero value V_0^a only between these two rings.

First, the matrix elements Eq. (3.9) have to be calculated

$$V_k^a(r_a) = \frac{V_0^a}{2\pi} \int_{-\pi}^{\pi} d\phi e^{ik\phi} \theta(r_a - r_1) \theta(r_2^2 - (r_a \cos(\phi) - b)^2 - r_a^2 \sin^2(\phi)).$$

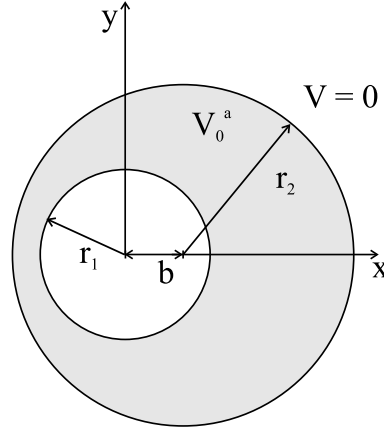


Figure 3.17: Schematic picture of the ring with D_1 symmetry with indicated ring radii r_i , the distance between ring centers b , and non-zero potential value V_0^a inside the ring.

The step functions lead to integration boundaries $\pm\phi$ given by

$$\cos(\phi(r_a)) = \frac{1}{2} \frac{b^2 + r_a^2 - r_2^2}{r_a b}, \quad (3.47)$$

and the matrix element is equal to

$$V_k^a(r_a) = V_0^a \left[\frac{1}{k\pi} \sin(k\phi(r_a)) \theta(r_a - r_2 + b) \theta(r_2 + b - r_a) + \delta_{k,0} \theta(r_a - r_1) \theta(r_2 - b - r_a) \right], \quad (3.48)$$

which properly satisfies the relation $V_k^a = V_{-k}^a$. The Hamiltonian is identical to Eq. (3.12).

Second, we study the eigenenergies with their corresponding oscillator strengths and the second derivatives which are plotted as a function of the magnetic field in Fig. 3.18 for type I nanoring. The behavior of the lowest three energies is not qualitatively different from the case of the circular symmetry since the energetically lowest states for different quantum numbers L do not cross. Their mixing manifests itself by the larger energy splitting among states with different $|L|$ and by the lifting of the degeneracy for the same $|L|$ at $B = 0$ T. Consequently, the oscillator strength is redistributed. The D_1 symmetry group implies that there is one symmetry axis, let us say the x -axis. The wave function transforms in the following way

$$\hat{T}_x \Psi_\alpha(x_e, y_e, x_h, y_h) = \Psi_\alpha(x_e, -y_e, x_h, -y_h) = \pm \Psi_\alpha(x_e, y_e, x_h, y_h). \quad (3.49)$$

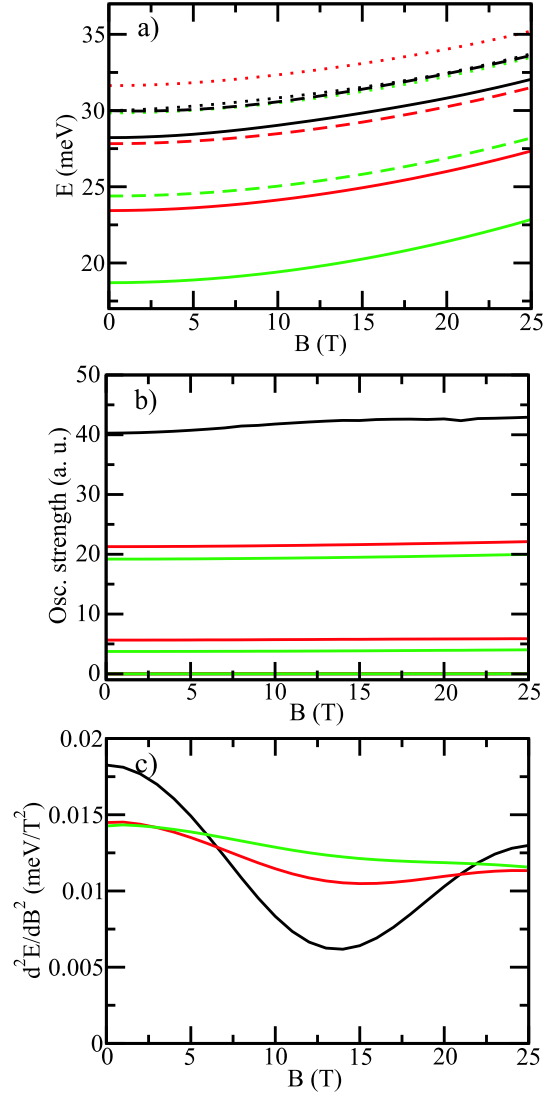


Figure 3.18: Energies (a) and corresponding oscillator strengths (b) of the ground (solid), the first (dashed), and the second (dotted) excited states, and the second derivative of the ground state energy (c) as a functions of the B -field for type I GaAs/AlGaAs nanorings with radii $r_1 = 4$ nm, $r_2 = 12$ nm and different shifts $b = 0$ nm black, $b = 1$ nm red, and $b = 2$ nm green.

There are two kinds of states with respect to this symmetry operation: even and odd ones. The odd ones have zero oscillator strength as immediately follows from Eq. (3.49). The doubly degenerate states with $L \neq 0$ of the circular nanoring can form an even and odd linear combination with respect to \hat{T}_x . As the symmetry is lowered these combinations are mixed. In the case of the C_1 symmetry all states could be optically active.³

The energetic order of even and odd states can be estimated for the lowest ones. The ground state is always even as shown in Fig. 3.18b. The first excited is an odd one since the contribution of the Coulomb interaction is similar to the ground state one but the kinetic energy is lower than for the next even one (analogous with e.g. a quantum well). The excited states have different Coulomb contributions and that's why their order cannot be determined in general.

The second derivative shown in Fig. 3.18c reveals that the ring topology of the wave function weakens as the outer ring is shifted more from the origin. The effective width d_R of the nanoring becomes angle dependent and varies from its minimum $d_R = r_2 - b - r_1$ at $\phi_a = \pi$ to its maximum $d_R = r_2 + b - r_1$ at $\phi_a = 0$. Due to the confinement energy it is convenient for the exciton wave function to be found predominantly at $\phi_a = 0$. Thus the value of the exciton wave function at $\phi = \pi$, and consequently the ring topology, is accordingly decreased. The ring topology is lost if $b \geq r_2 - r_1$ and the confinement potential is a banana-like quantum dot.

Let us turn now our attention towards type II nanoring. We investigate a special case of the InP/GaInP nanoring without strain assuming that the hole potential is dot-like. This guarantees that the hole is found always in the middle of the nanoring as it would be if the strain is taken into account. The strain would only modify the exact potential profile but not the symmetry.

As it has been already mentioned the spatial separation of the electron and hole leads to the darkening of the ground state with magnetic field. This is illustrated in Fig. 3.19a where crossings among states with different quantum number L are seen. Like for the type I nanoring all states are mixed if the symmetry is decreased to the D_1 symmetry, and inevitably all crossings become anti-crossings or disappear completely depending on the degree of displacement. In the present case there is no evidence of any anti-crossing left for the lowest states as clearly seen in Fig. 3.19a and consequently, the energy dependence on the magnetic field is qualitatively the same as for the

³However, it is important to notice that we were discussing only the brightness of exciton states with respect to the center-of-mass motion. Regarding the relative motion exciton states can be categorized as bright and dark ones at zero magnetic field too. In one-dimensional case they are even (bright) and odd (dark) ones, in two-dimensional case they are s - (bright), p -, d -,...like (dark).

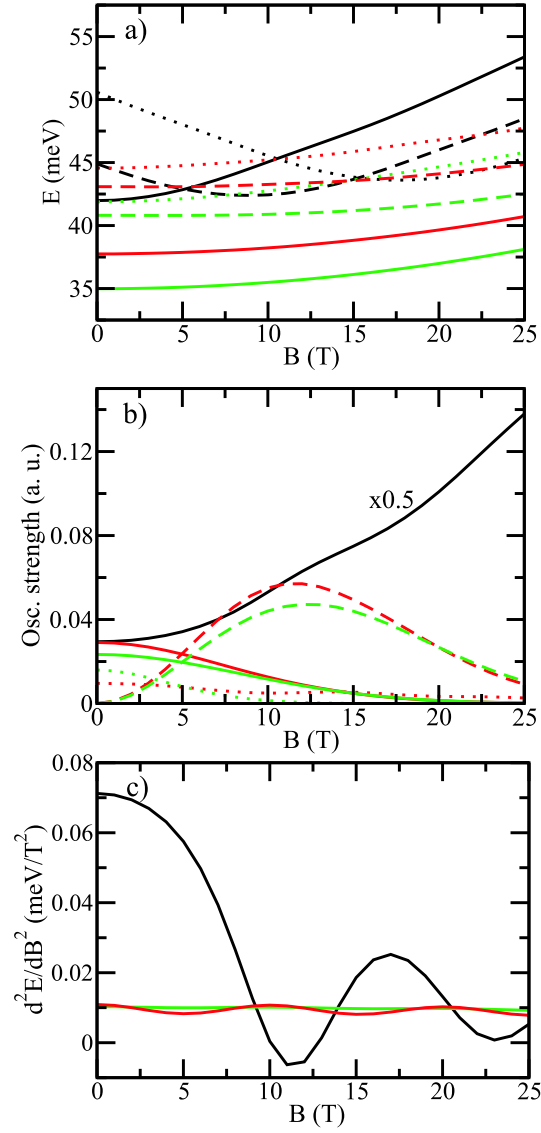


Figure 3.19: Energies (a) and corresponding oscillator strengths (b) as a functions of the B -field for type II InP/GaInP nanorings with radii $r_1 = 8$ nm, $r_2 = 16$ nm (for details see text) and different shifts $b = 0$ nm black (the lowest bright state $L = 0$ - solid, $L = 1$ - dashed, and $L = 2$ - dotted), $b = 1$ nm red (the ground (solid), the first (dashed), and the second (dotted) excited states), and $b = 2$ nm green.

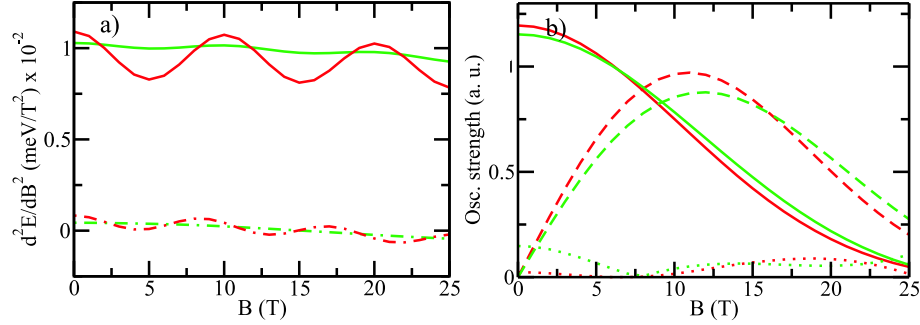


Figure 3.20: a) The comparison of the second derivatives of the ground state of the finite (solid, as in Fig. 3.19) and zero width nanoring (dashed-dotted, $r_e = 12.4$ nm, $r_h = 4.8$ nm for details see text). b) Oscillator strengths as a functions of the B -field for the three lowest states (the ground (solid), the first (dashed), and the second (dotted) excited states) of the zero width nanoring. In both cases different shifts $b = 1$ nm (red) and $b = 2$ nm (green) were considered.

type I nanoring.

However, the difference between type I and II nanorings becomes apparent when the oscillator strength is studied as depicted in Fig. 3.19b. The oscillator strength changes with the magnetic field as the character of the exciton wave function changes e.g. the main component of the ground state wave function for $B = 0$ T is $L = 0$, it is shifted to $L = 1$ for $B = 10$ T. This results in a decrease of the oscillator strength which is transferred to the first excited state (and increased due to the larger electron-hole overlap). Later on it is transferred to the second and higher excited ones where the states with different quantum numbers L mix. Although the ground state oscillator strength becomes exponentially small with increasing magnetic field it is never exactly zero, which has an interesting implications when the exciton kinetics is taken into account (see Sec. 4.3).

Unlike the case of the type I nanoring, the oscillation period changes with b (Fig. 3.19c). This is also accompanied by a decrease of the oscillation amplitude due to the loss of the ring topology with increasing b . The period of oscillations is no more related to the exciton relative motion with the period B_P but to the periodic exchange of the ground state main component from L to $L + 1$. Its period, can be derived within the zero width model from Eq. (3.41),

$$B_{P,2} = \frac{2\hbar}{e} \frac{1}{R_e^2 - R_h^2}. \quad (3.50)$$

In the present case, taking $R_e = \langle r_e \rangle = 12.3$ nm and $R_h = \langle r_h \rangle = 4.4$ nm we obtain $B_{P,2} = 9.9$ T, which agrees well with the observed period in Fig. 3.20c.

In order to apply the zero width model to non-circular symmetry the radial and azimuthal motion Eq. (3.25) has to be factorized. The expansion of the azimuthal part is again

$$\psi_\alpha(\phi, \Phi) = \sum_{l,L} c_{l,L}^\alpha e^{-il\phi} \frac{e^{iL\Phi}}{2\pi}, \quad (3.51)$$

which preserves the symmetry of the problem and the matrix elements $V_k^a(r_a)$ have to be averaged

$$V_k^a = \int_0^\infty dr r V_k^a(r) \eta_a^2(r). \quad (3.52)$$

The question is a choice of the proper functions $\eta_a(r)$. Assuming that the loss of the circular symmetry is rather weak and that the ring topology of the wave function is preserved we take for the functions $\eta_a(r_a)$ the confinement function of the circular ring ($b = 0$) $f_a(r_a)$.

Disregarding from the obvious constant contribution to the second derivative coming from the inner exciton motion the agreement between finite and zero width model is reasonable as seen in Fig. 3.20a. The underestimated oscillation amplitude is influenced by the choice of the radial functions $\eta_a(r)$. Nonetheless, the oscillator strengths for the three lowest states in the zero width model show qualitatively the same behavior as in the finite width model (compare Fig. 3.19b and Fig. 3.20b). At this point it may be concluded that the zero width model describes the main features of the full one.

Finally, the brief exploration of the circular symmetry attenuation has demonstrated that the amplitude of X-ABE gets weaker since the lower the symmetry the higher the probability that the wave function localizes and loses the general ring topology. However, if the asymmetry is weak and the electron and hole are spatially separated as in type II structures, the ground state, which has an oscillatory component and is always bright, exists.

Chapter 4

Emission kinetics

In the previous chapter we have seen that the exciton ground state in a nanoring is not necessarily optically active for every magnetic field. This is especially true for the circular nanoring if the electron and hole are spatially separated. Since the consequences of this fact for the photoluminescence have not been discussed yet we focus on them in this chapter.

Even though the exciton emission kinetics in nanostructures (e.g. for the case of disordered quantum wells see [Run02] and references therein) have been investigated theoretically since many years, nanorings have not been under such a focus so far. The reason may be that interesting effects are expected in type II nanorings only [dSUG04] which have not been grown up to now.

Here we derive expressions for the exciton-phonon scattering matrix elements and show examples of the photoluminescence quenching with increasing magnetic field under steady state conditions, including a non-radiative decay.

4.1 Theory

Let us assume that the eigenenergies E_α and corresponding wave functions ψ_α of the Hamiltonian Eq. (3.12) are known. We suppose that excitons are at the final stage of their thermalization after optical excitation and that their density is such low ($n_{exc}a_B \ll 1$) that exciton-exciton scattering is negligible.

In order to drive kinetic equation for the exciton population the exciton Hamiltonian which includes coupling to photons and to acoustic phonons has

to be written down in the second quantization [HK94; ZRS03]

$$\begin{aligned} \mathcal{H} = & \sum_{\alpha} E_{\alpha} b_{\alpha}^{\dagger} b_{\alpha} + \sum_{\mathbf{k}} \hbar \Omega_{\mathbf{k}} c_{\mathbf{k}}^{\dagger} c_{\mathbf{k}} + i \sum_{\alpha, \mathbf{k}} g_{\mathbf{k}, \lambda} (\mathcal{M}_{\alpha} b_{\alpha}^{\dagger} c_{\mathbf{k}} - \mathcal{M}_{\alpha}^{*} c_{\mathbf{k}}^{\dagger} b_{\alpha}) \\ & + \sum_{\mathbf{q}} \hbar \omega_{\mathbf{q}} a_{\mathbf{q}}^{\dagger} a_{\mathbf{q}} + \sum_{\alpha, \beta, \mathbf{q}} t_{\alpha\beta}^{\mathbf{q}} (a_{\mathbf{q}}^{\dagger} + a_{\mathbf{q}}) b_{\alpha}^{\dagger} b_{\beta}, \end{aligned} \quad (4.1)$$

where b_{α}^{\dagger} (b_{α}), $c_{\mathbf{k}}^{\dagger}$ ($c_{\mathbf{k}}$), and $a_{\mathbf{q}}^{\dagger}$ ($a_{\mathbf{q}}$) are bosonic creation (annihilation) operators of excitons, photons, and acoustic phonons respectively,

$$g_{\mathbf{k}} = \frac{\sqrt{2\pi\hbar\Omega_{\mathbf{k}}}}{n_R} e_{\mathbf{k}, \lambda}, \quad (4.2)$$

where $e_{\mathbf{k}, \lambda}$ polarization state of the light, $\mathcal{M}_{\alpha} = d_{cv} M_{\alpha}$ is an exciton photon coupling constant, $\hbar\omega_{\mathbf{q}} = \hbar s q$ ($\hbar\Omega_{\mathbf{k}} = \hbar c k / n_R$) is an acoustic phonon (photon) energy dispersion with s being the sound velocity (c being the light velocity and n_R index of refraction), and $t_{\alpha\beta}^{\mathbf{q}}$ are scattering rates between exciton states α and β due to bulk acoustic phonons¹ which are then given by [Tak85]

$$\begin{aligned} t_{\alpha\beta}^{\mathbf{q}} = & \sqrt{\frac{\hbar\omega_{\mathbf{q}}}{2s^2\rho_M V}} \int \int d\mathbf{r}_e d\mathbf{r}_h \Psi_{\alpha}(\mathbf{r}_e, \mathbf{r}_h) (D_c \exp(i\mathbf{q}\mathbf{r}_e) \\ & - D_v \exp(i\mathbf{q}\mathbf{r}_h)) \Psi_{\beta}(\mathbf{r}_e, \mathbf{r}_h), \end{aligned} \quad (4.3)$$

where ρ_M the mass density, V the sample volume, and D_c (D_v) the deformation potential for electron (hole).

The quantities, we are interested in, are polarization P_{α} of the state α and the density matrix $N_{\alpha\beta}$

$$P_{\alpha} = \langle b_{\alpha}^{\dagger} \rangle, \quad N_{\alpha\beta} = \langle b_{\alpha}^{\dagger} b_{\beta} \rangle. \quad (4.4)$$

In order to calculate the time dependence of $P_{\alpha}(t)$ and $N_{\alpha\beta}(t)$ the equation of motion in the Heisenberg picture $i\hbar\partial_t b_{\alpha}^{\dagger} = [\mathcal{H}, b_{\alpha}^{\dagger}]$ has to be considered. This leads to an infinite hierarchy of equations which has to be truncated. Assuming low excitation density and bulk phonons which are in thermal equilibrium because they can easily dissipate energy into faraway regions of the bulk, the expectation values with more than one phonon operator or more than two exciton operators together are factorized as²

$$\langle a_{\mathbf{q}}^{\dagger} a_{\mathbf{q}'} b_{\alpha}^{\dagger} \rangle = \langle a_{\mathbf{q}}^{\dagger} a_{\mathbf{q}'} \rangle \langle b_{\alpha}^{\dagger} \rangle = \delta_{\mathbf{q}\mathbf{q}'} n_B(\hbar\omega_{\mathbf{q}}) \langle b_{\alpha}^{\dagger} \rangle, \quad (4.5)$$

¹Although bulk phonons do not exist in layered system this is a very good approximation especially for GaAs/AlGaAs quantum wells [WG88; SD01].

²More precisely, following dynamical variables are considered: $P_{\alpha} = \langle b_{\alpha}^{\dagger} \rangle$, $N_{\alpha\beta} = \langle b_{\alpha}^{\dagger} b_{\beta} \rangle$, $\hat{T}_{\alpha\mathbf{q}} = \langle a_{\mathbf{q}}^{\dagger} b_{\alpha}^{\dagger} \rangle$, $\tilde{T}_{\alpha\mathbf{q}} = \langle a_{-\mathbf{q}}^{\dagger} b_{\alpha}^{\dagger} \rangle$, and $T_{\alpha\beta\mathbf{q}} = \langle a_{\mathbf{q}}^{\dagger} b_{\alpha}^{\dagger} b_{\beta} \rangle$.

where $n_B(\hbar\omega_q)$ is the Bose-Einstein occupation function. Proceeding further adopting the Markov and rotating wave approximation, we obtain

$$\begin{aligned} i\hbar\frac{\partial}{\partial t}N_{\alpha\beta}(t) &= ((E_\beta - E_\alpha) - i\hbar(\Gamma_\alpha + \Gamma_\beta))N_{\alpha\beta}(t) + i\hbar\delta_{\alpha\beta}\sum_{\rho}\gamma_{\alpha\rho}N_{\rho\rho}(t) \\ &\quad - 2\text{Im}\mathcal{M}_\alpha E_0(t)P_\alpha(t), \\ i\hbar\frac{\partial}{\partial t}P_\alpha(t) &= (E_\alpha - i\hbar\Gamma_\alpha + E_0(t)\mathcal{M}_\alpha)P_\alpha(t), \end{aligned} \quad (4.6)$$

where an incident light field $E_{\mathbf{k}}(t) = \delta_{\mathbf{k}\mathbf{k}_0}E_0(t)$ is directed along \mathbf{k}_0 and the total outscattering rate is defined as

$$2\Gamma_\alpha = r_\alpha + \sum_{\beta}\gamma_{\beta\alpha}, \quad (4.7)$$

where the phonon scattering rates

$$\begin{aligned} \gamma_{\alpha\beta} &= \frac{2\pi}{\hbar}\sum_{\mathbf{q}}|t_{\alpha\beta}^{\mathbf{q}}|^2 [(n_B(\hbar\omega_q) + 1)\delta(E_\beta - E_\alpha - \hbar\omega_q) \\ &\quad + n_B(\hbar\omega_q)\delta(E_\beta - E_\alpha + \hbar\omega_q)], \end{aligned} \quad (4.8)$$

and radiative rates (see appendix E)

$$r_\alpha = \frac{2\pi}{\hbar}\frac{2\pi\hbar\Omega_{\mathbf{k}}}{n_R^2}|\mathcal{M}_\alpha|^2\sum_{\mathbf{k},\lambda}e_{\mathbf{k},\lambda}\delta(E_\alpha - \hbar\Omega_{\mathbf{k}}), \quad (4.9)$$

have been introduced.

However, in the present section we do not aim to describe a coherent dynamics within the first picoseconds. Rather we concentrate on the non-coherent dynamics on longer time scale. The polarization is then almost zero and consequently also off-diagonal terms of density matrix since $N_{\alpha\beta}(t) = P_\alpha^*(t)P_\beta(t)$ holds. The final equations take the form of

$$\frac{\partial}{\partial t}N_\alpha = g_\alpha + \sum_{\beta}\gamma_{\alpha\beta}N_\beta - \left(r_\alpha + d_\alpha + \sum_{\beta}\gamma_{\beta\alpha}\right)N_\alpha, \quad (4.10)$$

where g_α is a state dependent generation (source) term and d_α a phenomenological non-radiative decay rate, representing processes as e. g. exciton annihilation via impurities, escape into the wetting layer or Auger processes. We note that even though these equations could be written immediately they are not invariant under unitary transformation and thus the results depend on the choice of the basis.

These equations are then solved numerically for the steady state situation $\frac{\partial}{\partial t} N_\alpha = 0$ which is experimentally relevant. Summing the kinetic equations Eq. (4.10) over all states α , a conservation law for the exciton occupation in the steady state is found

$$\sum_{\alpha} g_{\alpha} = \sum_{\alpha} (r_{\alpha} + d_{\alpha}) N_{\alpha}. \quad (4.11)$$

If the non-radiative rate is zero ($d_{\alpha} = 0$) the number of excitons which are optically generated and then decay radiatively is identical. Consequently, the spectrally integrated PL intensity

$$P(\omega) = \pi \sum_{\alpha} M_{\alpha}^2 N_{\alpha} \delta(\hbar\omega - E_{\alpha}), \quad (4.12)$$

$$\int d\omega P(\omega) = \text{const}_B \quad (4.13)$$

is constant with e.g. magnetic field. Thus the PL quenching is a clear indication of nonradiative processes ($d_{\alpha} \neq 0$).

First, we start with the evaluation of the radiative rates r_{α} which give the coupling between light and exciton in the state α explicitly

$$r_{\alpha} = r_{cv} |M_{\alpha}|^2; \quad r_{cv} = \frac{4}{3} \frac{d_{cv} E_g^3 n_R}{\hbar^4 c^3}. \quad (4.14)$$

The detailed derivation can be found in the appendix E. Taking into account the single sublevel approximation Eq. (1.64) and the expansion of the lateral part of the wave function Eq. (3.6), the rates r_{α} have the form of

$$r_{\alpha} = r_{cv} \left| \int_{-\infty}^{\infty} dz v_e(z) v_h(z) \sum_l \int_0^{\infty} dr r u_{l,0,\alpha}(r, r) \right|^2. \quad (4.15)$$

Second, we focus on the calculation of scattering rates between exciton states α and β . The expansion of the wave function Eq. (3.6) gives

$$t_{\alpha\beta}^{\mathbf{q}} = \sqrt{\frac{\hbar\omega_{\mathbf{q}}}{2s^2\rho_M V}} \times \sum_{L,L'} e^{i(L-L')\Phi_{\mathbf{q}}} \left(S_{L,L'}^{\alpha\beta e}(\mathbf{q}_{\parallel}) K_e(q_z) D_c - S_{L,L'}^{\alpha\beta h}(\mathbf{q}_{\parallel}) K_h(q_z) D_v \right), \quad (4.16)$$

introducing state dependent "overlap" matrix functions $S_{L,L'}^{\alpha\beta e(h)}(\mathbf{q}_{\parallel})$ and a z -dependent contribution

$$S_{L,L'}^{\alpha\beta e(h)}(\mathbf{q}_{\parallel}) = \sum_l \int_0^\infty dr_e r_e dr_h r_h u_{l,L,\alpha}(r_e, r_h) \times u_{l \mp \frac{L-L'}{2}, L', \beta}(r_e, r_h) J_{L-L'}(q_{\parallel} r_e(h)), \quad (4.17)$$

$$K_a(q_z) = \int dz v_a^2(z) e^{-iq_z z}, \quad (4.18)$$

where $S_{L,L'}^{\alpha\beta e(h)}(\mathbf{q}_{\parallel}) = S_{L',L}^{\beta\alpha e(h)}(\mathbf{q}_{\parallel})$ is satisfied and $J_{L-L'}(x)$ are Bessel functions of the first kind.

Further, the scattering matrix elements $t_{\alpha\beta}^{\mathbf{q}}$ are integrated over \mathbf{q} to obtain the scattering rates $\gamma_{\alpha\beta}$ depending on the energy difference $\Delta E = E_\alpha - E_\beta = \hbar s q$. Defining

$$\gamma_0 = \frac{1}{2\pi \hbar^4 s^5 \rho_M}, \quad T_{L-L'}^{\alpha\beta e(h)}(\mathbf{q}_{\parallel}) \equiv \sum_M S_{M, M-(L-L')}^{\alpha\beta e(h)}(\mathbf{q}_{\parallel}), \quad (4.19)$$

the final expression is obtained as

$$\begin{aligned} \gamma_{\alpha\beta}(\Delta E) &= \gamma_0 n_B(\Delta E) \Delta E^3 \int_0^\pi d\theta \sin(\theta) \times \\ &\sum_{L,L'} \left[S_{L,L'}^{\alpha\beta e}(q_{\parallel}) T_{L-L'}^{\alpha\beta e}(q_{\parallel}) K_e^2(q_{\perp}) D_c^2 + S_{L,L'}^{\alpha\beta h}(q_{\parallel}) T_{L-L'}^{\alpha\beta h}(q_{\parallel}) K_h^2(q_{\perp}) D_v^2 \right. \\ &\left. - (S_{L,L'}^{\alpha\beta e}(q_{\parallel}) T_{L-L'}^{\alpha\beta h}(q_{\parallel}) + S_{L,L'}^{\alpha\beta h}(q_{\parallel}) T_{L-L'}^{\alpha\beta e}(q_{\parallel})) K_e(q_{\perp}) K_h(q_{\perp}) D_c D_v \right], \end{aligned} \quad (4.20)$$

where $q_{\parallel} = q \sin(\theta)$ ($q_{\perp} = q \cos(\theta)$) is the parallel (perpendicular) component of the phonon quasi-momentum.

4.2 Circular quantum ring of zero width

First, we investigate a very simple example of the circular ring width zero width. Despite its simplicity, this example captures main features of finite width model. Adopting the assumptions of a narrow quantum well and of very narrow circular nanorings with radii R_a , the matrix elements $t_{\alpha\beta}^{\mathbf{q}}$ simplify to

$$\begin{aligned} t_{\alpha\beta}^{\mathbf{q}} &= \sqrt{\frac{\hbar \omega_q}{2s^2 \rho_M V}} e^{iL\Phi_q} \left(S_L^{\alpha\beta e} I_L^e(q_{\parallel}) K_e(q_z) D_c - S_L^{\alpha\beta h} I_L^h(q_{\parallel}) K_h(q_z) D_v \right), \\ S_L^{\alpha\beta e(h)} &= \sum_l c_l^\alpha c_{l \mp \frac{L}{2}}^\beta, \quad I_L^a(q_{\parallel}) = \int dr r f_a^2(r) J_L(q_{\parallel} r)_{L=L_\alpha-L_\beta}, \end{aligned} \quad (4.21)$$

where the wave function factorization Eq. (3.25) and expansion Eq. (3.26) with the quantum number L_α have been taken into account. Treating z -confinement and the radial wave functions as delta functions gives $K_a(q_z) = 1$ and $I_L^a(q_\parallel) = J_L(q_\parallel R_a)$.

A nanoring with radii $R_e = 12$ nm and $R_h = 3$ nm is investigated as a model example here. GaAs materials parameters are taken from [SAK01] and give $r_{cv} = 8.9 \times 10^{-1}$ ns $^{-1}$. The approximation of the delta function is not appropriate for the calculation of the radiative rate and that's why we assume that electron-hole overlap can be approximated by Gaussian function

$$r_\alpha = r_{cv} e^{-(R_e - R_h)^2 / 2\sigma_R^2} \left| \delta_{L_\alpha, 0} \sum_l c_l^\alpha \right|^2, \quad (4.22)$$

which can be evaluated for the ground state at $B = 0$ T

$$r_1 = 7.5 \times 10^{-3} \text{ ns}^{-1}, \quad (4.23)$$

where a radial extension $\sigma_R = 4$ nm was taken. The phonon matrix elements are of the following orders

$$\gamma_e = \gamma_0 D_c^2 = 35.4 \times 10^3 \text{ ns}^{-1} \text{ meV}^{-3}, \quad (4.24)$$

where $D_c = 7$ eV was taken. These numbers clearly show that the exciton-phonon scattering dominates the kinetics since ΔE is of the order of a few meV.

We briefly discuss the X-ABE. The second derivative of the energy with respect to the magnetic field is calculated in Fig. 3.3d and the first minimum of the oscillation is exactly at $B_P/2 = 15.4$ T. In this way it could be possible, in principle, to verify an oscillatory component $\Delta E_\alpha^{(1)}(B)$ of the total exciton energy as we have discussed in detail in the last Chapter.

Since the quantum number L_α abruptly changes with the B -field in order to minimize the energy contribution $\Delta E_\alpha^{(2)}(B)$, the ground state is no more optically active Eq. (4.22). This kind of behavior is shown in Fig. 4.1a where the lowest state with $L_\alpha = 1$ ($L_\alpha = 2$) is shown as a dashed (dotted) curve. The energy minimum of the $L_\alpha = 1$ state is found at $B_{Z,1} = 9.7$ T. As expected, the crossing point between the states with $L_\alpha = 0$ and $L_\alpha = 1$ ($L_\alpha = 1$ and $L_\alpha = 2$) is found at around $B_{Z,1}/2$ ($3B_{Z,1}/2$).

In order to estimate quantitatively the change of the PL with magnetic field, we concentrate on the steady state solution of the kinetic equations Eq. (4.10). Calculated PL spectra for state-independent generation $g_\alpha = g$ are shown in Fig. 4.1b and c. Taking into account the excellent optical yield of nanostructures in general, only a very small non-radiative rate $d_\alpha = 0.013 r_1$

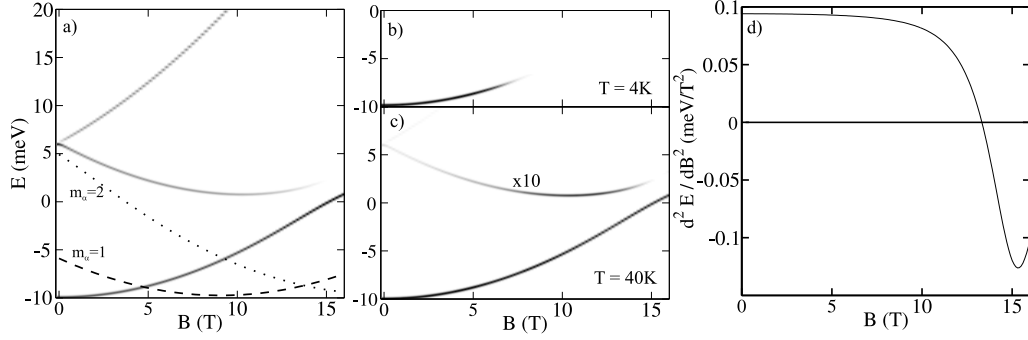


Figure 4.1: a) The absorption spectrum on linear gray scale. The lowest dark states are shown too (dashed: $L_\alpha = 1$ and dotted: $L_\alpha = 2$). Photoluminescence spectra for the lattice temperatures at b) $T = 4$ K and c) $T = 40$ K. d) The second derivative of the lowest bright state with respect to the magnetic field. The nanoring radii of zero width model are: $R_e = 12$ nm and $R_h = 3$ nm. GaAs material parameters from [SAK01]. Other parameters: state-independent generation $g_\alpha = g$, non-radiative decay $d_\alpha = 0.013 r_0$. 22 lowest exciton states were taken into account.

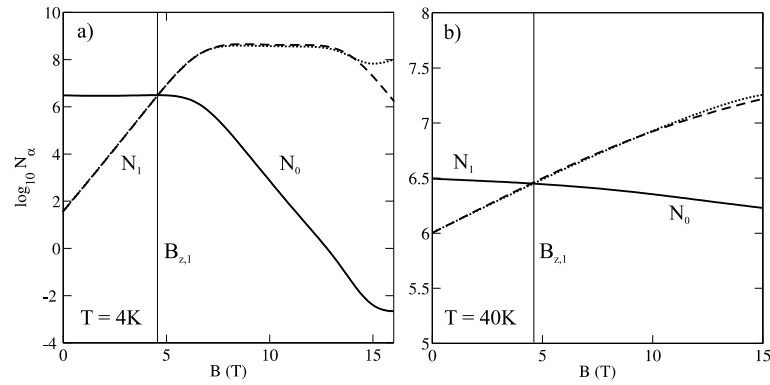


Figure 4.2: The occupation of the lowest optically active state N_0 (solid) and of the lowest optically non-active state N_1 with $L_\alpha = 1$ (dashed) for the lattice temperatures a) $T = 4$ K and b) $T = 40$ K. The dotted line is the equilibrium occupation of N_1^{eq} (see text). Parameters as in Fig. 4.1.

was assumed. Fig. 4.1b demonstrates the sharp luminescence quenching with increasing B -field for a low lattice temperature of $T = 4$ K shortly after the ground state gets dark (at $B_{Z,1}/2$). The PL-quenching is much weaker if the temperature is increased up to $T = 40$ K as shown in Fig. 4.1c where even the second lowest bright state can be observed (magnified by factor of 10).

In order to understand the behavior of the PL with B -field more thoroughly, the occupation of the lowest bright state (with $L_\alpha = 0$), called 0, and the lowest state with $L_\alpha = 1$, called 1, are plotted as function of the B -field in Fig. 4.2. The low temperature case shows a pronounced behavior with magnetic field. At zero B -field the state 0 is strongly occupied and this does not change up to the crossing point of the energies and occupations of both states. On the contrary, the occupation of the state 1 increases linearly (in logarithmic plot) since its energy decreases. As the occupation of the state 0 starts to decrease linearly at around $B = 6$ T the PL starts to quench. The case of higher temperature shows qualitatively similar behavior but the change in the occupation of state 0 and 1 are smoother and smaller compared to the low temperature case. Thermal equilibrium between both states would result in $N_1^{eq} = N_0 \exp(-(E_1 - E_0)/k_B T)$ (k_B being the Boltzmann constant, E_0 and E_1 eigenenergies of both states). As shown by dotted curves in Fig. 4.2, this is well preserved up to $B = 14$ T when the ground state changes its quantum number to $L_\alpha = 2$. In the low temperature case thermal equilibrium is found only among the first few states unlike for the higher temperature where it is achieved for almost all states.

This analysis suggests to measure at higher temperatures in order to diminish the PL-quenching. However, an experimental disadvantage for such a choice is the strongly reduced signal to noise ratio. Since our goal is not only to observe the energy of the lowest bright state with B -field but to calculate the second derivative from the data, noise-free high quality data are desired.

4.3 Non-circular quantum ring of zero width

After discussing the simplest model we turn now our attention towards a non-circular ring. Although we try to make our approach realistic as much as possible some approximations cannot be avoided. Especially, the calculation of the phonon scattering matrix elements represents a serious problem, which can be circumvented by adopting the zero width model for their calculation but with energies coming from the finite width model. Doing so we assume that Bose-Einstein occupation function $n_B(\hbar\omega_q)$ plays a decisive role.

The radiative rates are calculated precisely within finite width model as

$$r_\alpha = r_{cv} \left| \sum_l \int_0^\infty dr r u_{l,0,\alpha}(r, r) \right|^2. \quad (4.25)$$

Adopting now the zero width model and treating further z -confinement and the radial wave functions as delta functions, the matrix elements $\gamma_{\alpha\beta}$ Eq. (4.8) simplify to

$$\begin{aligned} \gamma_{\alpha\beta}(\Delta E) &= \gamma_0 n_B(\Delta E) \Delta E^3 \\ &\sum_{LL'} \left[S_{LL'}^{\alpha\beta e} T_{L-L'}^{\alpha\beta e} I_{L-L'}^{ee}(q_{\parallel}) D_c^2 + S_{LL'}^{\alpha\beta h} T_{L-L'}^{\alpha\beta h} I_{L-L'}^{hh}(q_{\parallel}) D_v^2 \right. \\ &\quad \left. - (S_{LL'}^{\alpha\beta e} T_{L-L'}^{\alpha\beta h} + S_{LL'}^{\alpha\beta h} T_{L-L'}^{\alpha\beta e}) I_{L-L'}^{eh}(q_{\parallel}) D_c D_v \right], \end{aligned} \quad (4.26)$$

$$S_{L,L'}^{\alpha\beta e(h)} = \sum_l c_{l, L}^\alpha c_{l \mp \frac{L-L'}{2}, L'}^\beta, \quad T_{L-L'}^{\alpha\beta e(h)} = \sum_M S_{M, M-(L-L')}^{\alpha\beta e(h)},$$

$$I_M^{ab} = \int_0^\pi d\theta \sin(\theta) J_M [q \sin(\theta) R_a] J_M [q \sin(\theta) R_b]. \quad (4.27)$$

It is important to stress that despite the factorization of the radial and azimuthal motion the symmetry of the problem (D_1 in this case) is preserved.

We investigate slightly asymmetric type II InP/GaInP nanoring with radii $r_1 = 8$ nm, $r_2 = 16$ nm, and $b = 0.5$ nm (for details see Sec. 3.5). Unfortunately, due to the uncertainty in the values of the deformation potentials $D_{c,v}$ for InP/GaInP we take those of GaAs. The radiative rate of the lowest state at $B = 0$ T is equal to

$$r_1 = 2.7 \times 10^{-2} \text{ ns}^{-1}, \quad (4.28)$$

which is still much smaller than the phonon matrix elements Eq. (4.24) and consequently, the exciton-phonon scattering dominates the kinetics as before.

The absorption spectrum plotted in Fig. 4.3a demonstrates nicely how the oscillator strength is transformed to higher states with increasing magnetic field as already discussed in detail in Sec. 3.5. Despite this transfer, the ground state remains optically active, even though its oscillator strength at $B = 25$ T is less than 10^{-2} of the value at $B = 0$ T. Although the oscillation of the ground state cannot be seen by a naked eye, the second derivative reveals them unambiguously in Fig. 4.3b with enhanced amplitude compared to the circular ring plotted in Fig. 3.8. The oscillations of higher states are seen clearly and the period agrees well with Eq. (3.50).

The investigation of the circular ring in the last section has indicated that although the amplitude of the oscillations can be large any presence of

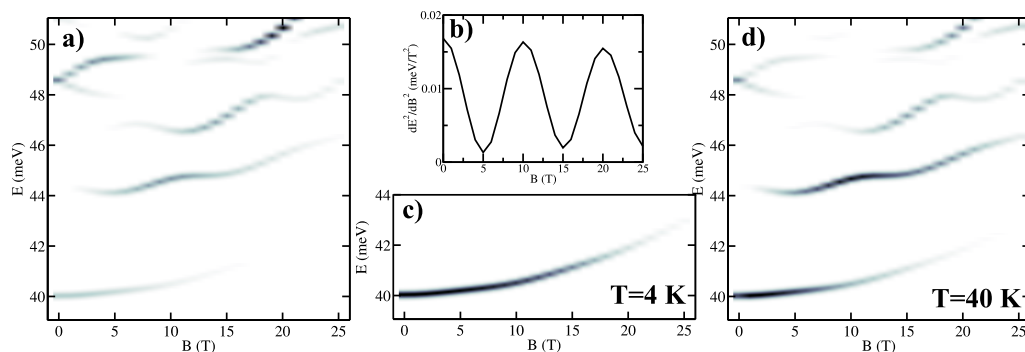


Figure 4.3: a) Absorption spectrum on linear gray scale for type II InP/GaInP nanorings with radii $r_1 = 8$ nm, $r_2 = 16$ nm and $b = 0.5$ nm. b) The second derivative of the ground state with respect to the magnetic field. Photoluminescence spectra for the lattice temperatures at c) $T = 4$ K and d) $T = 40$ K. Other parameters: state-independent generation $g_\alpha = g$ and non-radiative decay $d_\alpha = 0.1 r_1$. 7 lowest exciton states were taken into account (see text for details).

the non-radiative decay channels spoils their observability in the experiment substantially. On the other hand, it has been demonstrated in Sec. 3.5 that the lowering of the symmetry decreases the amplitude of the oscillations in most cases but it also keeps the ground state bright. The photoluminescence spectra depicted in Fig. 4.3c and d show that there is a measurable signal up to almost $B = 25$ T supposing moderate non-radiative decay rate of $d_\alpha = 0.1 r_1$ (factor of ten compared with previous section). Only the ground state is visible for low temperature $T = 4$ K (Fig. 4.3c) in contrast with higher temperature $T = 40$ K where the PL spectrum (Fig. 4.3d) resembles very much the absorption (Fig. 4.3a).

Thus we conclude that surprisingly the small violation of the circular symmetry improves the observability of the X-ABE because the small asymmetry changes crossing among states with different L into periodic anticrossing with period $B_{P,2}$ Eq. (3.50), which manifests itself strongly in the second derivative, and additionally the ground state has always non-zero oscillator strength.

From this point of view we may speculate that the indication of the X-ABE reported in Ref. [RGWCMR04] is influenced by the slight asymmetry of the InP/GaAs quantum dots which was not taken into account in the theoretical interpretation.

Part IV

Summary and Outlook

The excitonic optical properties of disordered quantum wells and ideal quantum rings have been studied. Our theoretical approach has been based on the envelope function formalism, effective mass and single sublevel approximation. The main achievements in the first part can be summarized as follows

- ◇ It has been analytically proven that the ground state energy at $B = 0$ T is a lower boundary for the ground state energy at any magnetic field.
- ◇ Absorption spectra and diamagnetic shifts have been calculated for the exciton in-plane motion without any further approximation.
- ◇ The results of the full calculation have been compared with the factorization into exciton relative and center-of-mass motion. The factorization ansatz leads to incorrect values of the diamagnetic shift.
- ◇ The diamagnetic shift for different single localized excitons of the same energy differs. Its average increases with energy.
- ◇ The enhancement of the electron effective mass due to the confinement is essential for the diamagnetic shift coefficient.
- ◇ Structural data from the XSTM experiment have been analyzed and the potential averaging and correlation functions have been extracted. Generating new potential realizations with the same statistical properties, absorption, photoluminescence spectra and diamagnetic shift coefficients have been calculated. Very good agreement with the experiment has been found.

The main outcomes of the second part are listed below

- ◇ The exciton Hamiltonian of the quantum ring has been derived and expressed in Jacobi angular coordinates.
- ◇ After introducing an angular expansion of the wave function, non-zero matrix elements have been sorted according to the symmetry point group of the confining potential.
- ◇ Within the model of zero width nanoring, analytical expressions have been derived and compared with the full model.
- ◇ The strain has been included into the calculation within the isotropic elasticity approach.

- ◇ Assuming circular symmetry, type I and type II nanorings made of different materials have been studied and the influence of material parameters has been discussed. The close relation between the oscillatory component of the exciton energy with magnetic field and the persistent current has been revealed. Non-circular nanorings have been investigated, too.
- ◇ The exciton emission kinetics via interaction with acoustic phonons has been calculated within the model of zero width nanoring. Analytical expressions for the scattering matrix elements for circular and non-circular nanorings have been calculated. Including non-radiative exciton decay, a quenching of the photoluminescence has been demonstrated.

As an outlook the present our work can be extended into following directions:

- ★ Having the full exciton in-plane wave function at hand, other exciton properties as e.g. the resonant Rayleigh scattering which has been investigated so far with the factorization ansatz, can be calculated. Especially, the perpendicular magnetic field can be included.
- ★ Regarding the comparison between theory and experiment of the quantum well exciton photoluminescence, an exact calculation of the scattering matrix elements for the exciton emission kinetics would be desirable.
- ★ For the quantum rings, the single sublevel approximation could be abandoned which opens the possibility to investigate other confinement structures. Additionally, the strain should be calculated within a more realistic approach of continuum mechanics. Other contributions like piezo-electric fields or image charge effects could be taken into account, too. The approximation of the zero width nanoring should be lifted for the calculation of the emission kinetics. Finally, comparison with experimental data should be regarded as an ultimate check of the theoretical results.

Part V
Appendices

Appendix A

Material parameters

The complete set of material parameters is listed in Tabs. A.1 and A.2.

Table A.1: Selected material parameters used in the calculation.

	a_0 (Å)	E_g (eV)	m_e	m_h^3	a_c (eV)	a_v (eV)	b (eV)
GaAs ¹	5.6533	1.519	0.067 ⁷	0.36 ⁸	-7.2	1.2	-2.0
Al _{0.3} Ga _{0.7} As ¹	5.6556	2.013 ⁵	0.084 ⁶	0.39 ⁶	-6.7	1.6	-2.1
InP ²	5.8687	1.424	0.077	1.67	-7.0	0.4	-2.0
Ga _{0.51} In _{0.49} P ²	5.6553	1.970	0.125	0.60	-7.5	0.4	-2.0
InAs ¹	6.0583	0.417	0.026	0.51	-5.1	1.0	-1.8
Al _{0.6} Ga _{0.4} Sb ¹	6.1197	1.756	0.10	0.56	-5.7	1.2	-1.6
GaSb ¹	6.0959	0.812	0.039	0.71	-6.0	1.1	-1.7

¹[VMRM01], ²[TPJ+02], ³ $m_{hh}^{[110]} = \frac{1}{2}(2\gamma_1 - \gamma_2 - 3\gamma_3)$ [VMRM01], ⁴[JPP01], ⁵recent tight-binding calculation [VS], ⁶[Ada94], ⁷Due to the confinement the electron effective becomes anisotropic and has the values of $m_{e,\parallel} = 0.78$ and $m_{e,\perp} = 0.70$ for 4 nm wide GaAs/AlGaAs quantum well [Eke89]; ⁸Taking into account the exciton center-of-mass motion in quantum wells using the 6 bands $k \cdot p$ theory, "renormalized" hole effective mass is obtained: $m_{h,\parallel} = 0.233$ for 4 nm wide GaAs/AlGaAs quantum well [SRZ00].

Table A.2: Chemical band edges in meV, relative lattice mismatch ϵ_λ and static dielectric constant ϵ_S .

	GaAs/AlGaAs	InP/GaInP	InAs/AlGaSb	GaSb/GaAs
E_e	-257	-600	-1673	63
E_h	-110	50	332	-770
ϵ_λ (%)	0	3.81	-1.00	7.83
ϵ_S	12.5	12.6	15 ¹	12.5

¹[XCQ92].

Appendix B

Gauge transformation

B.1 Choice of the gauge

In principle any gauge of the magnetic field can be used, since physical results should be independent of it. However, this is not true if the numerical solution of the Schrödinger equation is considered because an oscillatory behavior of the wave function may cause problems. In order to see this in more detail we start with the in-plane electron-hole Hamiltonian with the Coulomb one-particle gauge of the magnetic field

$$\mathbf{A}_e(\mathbf{r}_e) = \frac{B}{2}(y_e, -x_e, 0), \quad \mathbf{A}_h(\mathbf{r}_h) = \frac{B}{2}(y_h, -x_h, 0), \quad (\text{B.1})$$

$$\begin{aligned} \hat{H}_{exc} = & -\frac{\hbar^2}{2m_e}\Delta_{\mathbf{r}_e} - \frac{\hbar^2}{2m_h}\Delta_{\mathbf{r}_h} + \frac{e^2 B^2}{8}\left(\frac{r_e^2}{m_e^2} + \frac{r_h^2}{m_h^2}\right) \\ & + V_e(\mathbf{r}_e) + V_h(\mathbf{r}_h) - V_C(\mathbf{r}_e - \mathbf{r}_h) \\ & + \frac{eB}{2m_e}i\hbar[y_e\partial_{x_e} - x_e\partial_{y_e}] + \frac{eB}{2m_h}i\hbar[-y_h\partial_{x_h} + x_h\partial_{y_h}]. \end{aligned} \quad (\text{B.2})$$

Changing the gauge to relative coordinates the transformation function $\lambda(\mathbf{r}_e, \mathbf{r}_h)$ Eq. (1.76) has the form of

$$\mathbf{A}_r(\mathbf{r}) \equiv \check{\mathbf{A}}(\mathbf{r}_e, \mathbf{r}_h) = \frac{B}{2}(y_e - y_h, x_h - x_e, 0), \quad (\text{B.3})$$

$$\lambda(\mathbf{r}_e, \mathbf{r}_h) = \frac{eB}{2\hbar}(y_e x_h - y_h x_e) = \frac{e}{\hbar}\mathbf{A}_r(\mathbf{r}) \cdot \mathbf{R}, \quad (\text{B.4})$$

and the wave function is transformed as

$$\Psi_\lambda(\mathbf{r}_e, \mathbf{r}_h) = \exp\left(-i\frac{e}{\hbar}\mathbf{A}_r(\mathbf{r}) \cdot \mathbf{R}\right) \Psi(\mathbf{r}_e, \mathbf{r}_h). \quad (\text{B.5})$$

The Hamiltonian for $\Psi_\lambda(\mathbf{r}_e, \mathbf{r}_h)$ is just Eq. (2.2). By separating the term $\exp\left(-i\frac{e}{\hbar}\mathbf{A}_r(\mathbf{r}) \cdot \mathbf{R}\right)$ from the wave function, the Hamiltonian Eq. (2.2) has

no longer B terms which depend on the absolute position of one particle (or of the center-of-mass). Thus, any oscillations of the wave function are restricted to its extension in relative space, which is of the order of the exciton Bohr radius. Other gauges with a dependence of the vector potential on the center-of-mass coordinates would lead to oscillating features across the entire sample, which is not suitable for a numerical solution using a finite grid size.

Nonetheless, the one-particle gauge Eq. (B.1) is well suited for the quantum ring, especially if circular symmetry is assumed, because the wave function can be factorized Eq. (3.24). Moreover, due to the lateral confinement which fixes the radial electron and hole positions, magnetic field dependence of the absolute one particle position dominates over the Coulomb interaction.

B.2 Numerical implementation

Although the gauge is chosen so that it was optimally suited for the numerical solution another problem appears. The naive discretization of Hamiltonians the Eqs. (2.2) and (B.2) on a grid results in a form which is not invariant under gauge transformation Eq. (1.76). Instead the discrete form of the continuous *one-particle* gauge transformation has to be considered, which takes the form of

$$\mathbf{A}_\lambda(\mathbf{r}_i) = \mathbf{A}(\mathbf{r}_i) + \frac{1}{\Delta_x}(\lambda(\mathbf{r}_i + \mathbf{\Delta}) - \lambda(\mathbf{r}_i)), \quad (\text{B.6})$$

where \mathbf{r}_i is a two-dimensional vector on a square grid with the grid step Δ_x and $\mathbf{r}_i + \mathbf{\Delta}$ is position of the next neighbor of \mathbf{r}_i in the direction $\mathbf{\Delta}$. Based on ideas of Peierls [Pei32] and Wilson [Wil74], a discretization of the Hamiltonian whose eigenvalues are gauge invariant under Eq. (B.6), has been proposed recently [GU98], where the one-particle kinetic term $T = (-i\nabla - e\mathbf{A}_\lambda(\mathbf{r}))^2$ is discretized as follows

$$T_{ij}^D = \sum_{\mathbf{\Delta}} \frac{1}{\Delta_x^2} [2\delta_{i,j} - U_{\mathbf{\Delta}}(j)\delta_{i-\mathbf{\Delta},j} - U_{\mathbf{\Delta}}(i)\delta_{i+\mathbf{\Delta},j}], \quad (\text{B.7})$$

where

$$U_{\mathbf{\Delta}}(i) = \exp\left(i\frac{e}{\hbar}A_{\mathbf{\Delta}}(\mathbf{r}_i)\right), \quad (\text{B.8})$$

where $A_{\mathbf{\Delta}}$ is the component of \mathbf{A} in the direction $\mathbf{\Delta}$. Even though the eigenenergies calculated using Eq. (B.7) are slightly lower compared to those calculated using the naive discretization, this discretization does not improve the problem of the oscillating phases $\exp\left(-i\frac{e}{\hbar}\mathbf{A}_r(\mathbf{r}) \cdot \mathbf{R}\right)$.

Appendix C

Numerics

The main numerical methods have been used in this work: the Leapfrog and Lanczos method. The Leapfrog method was used when the entire absorption spectrum was required. On the contrary the Lanczos method was used to obtain energies and wave functions of the lowest (tail) states with high precision. Both methods give numerically identical results.

C.1 Leapfrog method

First, let us rewrite the complex linear optical susceptibility Eq. (1.51) as

$$\chi(\omega) = \langle \mu | [\hat{H} - \hbar\omega + i0^+]^{-1} | \mu \rangle, \quad (\text{C.1})$$

$$\langle r | \mu \rangle = d_{cv} \delta(\mathbf{r}_e - \mathbf{r}_h), \quad (\text{C.2})$$

where $|\mu\rangle$ represents an electron-hole excitation state from the semiconductor vacuum. Since a calculation of a sufficient number of eigenvalues and eigenfunctions of the full electron-hole Hamiltonian Eq. (2.2) is demanding (the vector size is $N = 30^4 = 810.000$ or $N = 40^4 = 2.560.000$) the direct diagonalization has to be circumvented by calculating the time evolution of the wave function

$$i\hbar \frac{d}{dt} |\Psi(t)\rangle = \hat{H} |\Psi(t)\rangle, \quad |\Psi(0)\rangle = |\mu\rangle, \quad (\text{C.3})$$

projecting the wave function $|\Psi(t)\rangle$ on $|\mu\rangle$, and performing the Fourier transformation

$$\chi(\omega) = \frac{i}{\hbar} \int_0^\infty dt e^{-i\omega t} \langle \Psi(t) | \mu \rangle. \quad (\text{C.4})$$

The quick and efficient implementation of the time evolution Eq. (C.3) using the Leapfrog method proposed in [GCB96] was adopted. In order to handle

the effects of finite time integration in the Fourier transformation a small Gaussian damping is introduced in Ref. [PTVF02]

$$D(\omega) \equiv \text{Im}\chi(\omega) = \text{Re} \frac{1}{\hbar} \int_0^\infty dt e^{-i\omega t} e^{-(\sigma t/\hbar)^2} \langle \Psi(t) | \mu \rangle. \quad (\text{C.5})$$

The expansion of $|\Psi(t)\rangle$ into the eigenfunctions $|\Psi_\alpha\rangle$ of the Hamiltonian Eq. (2.2)

$$|\Psi(t)\rangle = \sum_\alpha |\Psi_\alpha\rangle \langle \Psi_\alpha | \mu \rangle e^{-iE_\alpha t/\hbar}, \quad (\text{C.6})$$

$$\hat{H}_{exc} |\Psi_\alpha\rangle = E_\alpha |\Psi_\alpha\rangle, \quad (\text{C.7})$$

gives a Gaussian broadened optical density Eq. (1.54)

$$D(\omega) = \sum_\alpha \pi |M_\alpha|^2 \frac{1}{\sqrt{2\pi}\sigma} \exp\left(-\frac{(\hbar\omega - E_\alpha)^2}{2\sigma^2}\right), \quad (\text{C.8})$$

$$M_\alpha = \langle \Psi_\alpha | \mu \rangle. \quad (\text{C.9})$$

Given the eigenenergy, the corresponding eigenfunction can be extracted integrating over the time dependent wave function in a second run

$$\langle \mathbf{r}, \mathbf{R} | \Psi_\alpha \rangle \sim \int dt \langle \mathbf{r}, \mathbf{R} | \Psi(t) \rangle e^{iE_\alpha t/\hbar} e^{-(\sigma t/\hbar)^2}. \quad (\text{C.10})$$

In this way, however, only wave functions of energetically well separated eigenstates can be obtained.

C.2 Implementation and tests

The electron and hole confinement wave functions $v_a(z_a)$ Eq. (1.64) without disorder are calculated numerically. Then, the Coulomb averaging Eq. (1.71) is performed and the factorized Schrödinger equation Eq. (B.2) is numerically solved. The wave function $\phi_{1s}(\mathbf{r}; B)$ obtained in this way is used twice: in the factorization approach and to generate the discretized Coulomb potential for the full solution using the identity

$$V_C(r) = \frac{\left(\frac{\hbar^2}{2\mu} \Delta_{\mathbf{r}}\right) \phi_{1s}(\mathbf{r}; 0)}{\phi_{1s}(\mathbf{r}; 0)} + E_{1s}(0), \quad (\text{C.11})$$

as introduced in [GCB96]. This method also handles the Coulomb singularity at the origin. The Hamiltonian Eq. (2.2) in electron and hole coordinates is

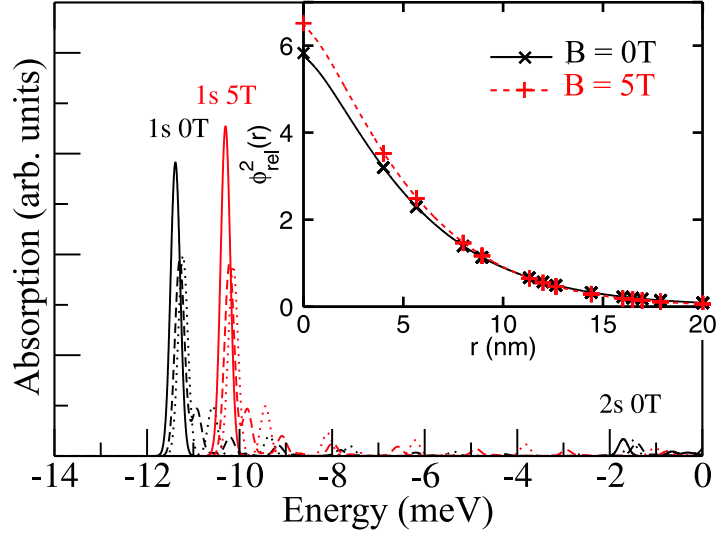


Figure C.1: Absorption spectra without disorder calculated using the exact solution taking Eq. (B.2) for all states (solid). For the full solution, two simulation sizes are used $N = 30^4$ (dotted) and $N = 40^4$ (dashed) with a grid step of 4 nm. Inset: The probability densities of the relative part of the total wave function Eq. (2.24) calculated for the 1s-state of the full solution (crosses) and calculated exactly (line) for 0 T and 5 T (units in 10^{-3} nm^{-2}).

given by

$$\begin{aligned}
 \hat{H}_{exc} = & -\frac{\hbar^2}{2m_e} \Delta_{\mathbf{r}_e} - \frac{\hbar^2}{2m_h} \Delta_{\mathbf{r}_h} + \frac{e^2 B^2}{8\mu} (\mathbf{r}_e - \mathbf{r}_h)^2 \\
 & + V_e(\mathbf{r}_e) + V_h(\mathbf{r}_h) - V_C(r) \\
 & + \frac{eB}{2m_e} i\hbar [(y_e - y_h) \partial_{x_e} - (x_e - x_h) \partial_{y_e}] \\
 & + \frac{eB}{2m_h} i\hbar [(y_e - y_h) \partial_{x_h} - (x_e - x_h) \partial_{y_h}], \quad (C.12)
 \end{aligned}$$

which is implemented instead of Eq. (2.2). The choice of electron and hole coordinates is advantageous for a possible inclusion of disorder from growth simulations [ZGR97].

The factorization ansatz Eq. (2.16) holds precisely in the no-disorder case, which is used to test the full solution. The only optically active state has a constant center-of-mass part (delocalized). The absorption spectra plotted in Fig. C.1 compare full and exact solution. Due to a combined effect of boundary conditions and finite simulation size, the exact spectrum is not fully reconstructed in the full solution. There is a small energy shift of the

dominant peak and additional small peaks appear. Increasing the simulation size the satellite peaks move towards the main peak.

In the presence of disorder the center-of-mass projection of the wave function is localized and far less sensitive to the boundary conditions. Therefore, our implementation is suited for the disorder case (localized states).

An important feature is the almost correct reconstruction in the full solution of the 2s exciton state (the second eigenvalue E_{2s} of Eq. (B.2) with eigenfunction $\phi_{2s}(\mathbf{r})$) since the potential is constructed only with the 1s wave function. The diamagnetic shifts of the 1s and 2s excitons are also obtained correctly with less than 3% error. The relative parts of wave functions plotted in the inset of Fig. C.1 demonstrate the good agreement as well.

C.3 Lanczos method

Unlike the previous method, the Lanczos method enables to calculate the lowest eigenvalues of large sparse hermitian matrices by iteration. It is very efficient and easy to implement. The principles of this method are described e. g. in Ref. [LG96]. As in the case of the Leapfrog method the wave function can be obtained in a second run of the whole iteration. A disadvantage is the fast growth of the computational time with the number of needed eigenvalues. We have implemented this method for the solution of the four-coordinate Schrödinger equation which enabled us to calculate the energies and wave functions of the tail states with very high precision. The time needed is only a fraction of that needed in the Leapfrog method. This becomes important mainly at small grid steps since the number of iterations in the Leapfrog method scales with $1/\Delta_x^2$.

Unfortunately, the straightforward implementation of the Lanczos method leads to the appearance of multiple or even spurious eigenvalues. This is due to the loss of orthogonality of the Lanczos basis during the iteration by round off errors. The remedy is an additional re-orthogonalization of the basis which has to be stored. The storage of the basis in the memory could represent a serious limitation. Nevertheless, this can be overcome if the iteration is restarted after a limited number of steps. Thus, also a small number of basis vector has to be stored only. This variant is called thick-restart Lanczos method and has been introduced only recently for electronic structure calculations [WS98; WS99].

Appendix D

Correlation function

Here, the details of the correlation function reconstruction performed in Sec. 2.8.2 are described. Assuming an arbitrary averaging function A_{mn} on the two-dimensional discrete grid and with the definitions of the one-dimensional discrete Fourier transformation

$$X_k = \sum_{j=0}^{N-1} x_j e^{(-i2\pi) \frac{jk}{N}}, \quad x_j = \frac{1}{N} \sum_{k=0}^{N-1} X_k e^{(i2\pi) \frac{jk}{N}}, \quad (\text{D.1})$$

the averaging function in reciprocal space takes the form of

$$A_{mn} = \frac{1}{N^2} \sum_{p,q=0}^{N-1} \tilde{A}_{pq} e^{(i2\pi) \frac{mp}{N}} e^{(i2\pi) \frac{nq}{N}}. \quad (\text{D.2})$$

Using the standard definition of the disorder potential via

$$W_{mn} = \sum_{kl} A_{|m-k||n-l|} U_{kl}, \quad \langle U_{mn} U_{lk} \rangle = \delta_{mk} \delta_{nl}, \quad (\text{D.3})$$

where the values of U_{kl} are Gaussian distributed random numbers with the variance $\sigma^2 = 1$, the averaged one-dimensional correlation function can be written explicitly as

$$\begin{aligned} \langle C_s^{(1)} \rangle &= \frac{1}{N} \langle W_{m+s0} W_{m0} \rangle = \frac{1}{N} \sum_{kl} A_{|m+s-k||l|} A_{|m-k||l|} \\ &= \frac{1}{N^3} \sum_{pq} |\tilde{A}_{pq}|^2 e^{(i2\pi) \frac{sp}{N}}, \end{aligned} \quad (\text{D.4})$$

where the identity $\sum_k e^{(i2\pi) \frac{kp}{N}} = N \delta_{p,0}$ was used. The Fourier component has the simple form of

$$\langle \tilde{C}_n^{(1)} \rangle = \frac{1}{N^2} \sum_q |\tilde{A}_{nq}|^2. \quad (\text{D.5})$$

The scheme of the program is straightforward: (i) The coefficients A_{mn} are calculated. (ii) The Fourier transformation is performed to obtain \tilde{A}_{mn} . (iii) The one-dimensional correlation function $\tilde{C}_n^{(1)}$ is evaluated. (iv) The correlation $\tilde{C}_n^{(1)}$ is compared to the experimental one and parameters entering A_{mn} are optimized.

Appendix E

Radiative rates

In order to calculate radiative rates Eq. (4.9) the exact form of Bloch functions and light polarization have to be taken into account. We restrict ourselves only to the heavy hole exciton in the quantum well for which Eq. (4.9) modifies to [Run02; And91]

$$r_\alpha = \frac{(2\pi)^2 \Omega_k}{n_R^2} |\mathcal{M}_\alpha|^2 \sum_{\mathbf{k}} \left(1 + \frac{\sqrt{k^2 - k_\parallel^2}}{k} \right) \delta(E_\alpha - \hbar\Omega_{\mathbf{k}}), \quad (\text{E.1})$$

where the first term corresponds to transverse-electric (perpendicular to \mathbf{k}_\parallel and \mathbf{e}_z), and the second one to transverse-magnetic (in the $(\mathbf{k}_\parallel - \mathbf{e}_z)$ plane) polarization. Changing summation to integration $\sum_{\mathbf{k}} \rightarrow \frac{1}{(2\pi)^3} \int d\mathbf{k}$ and performing integration over k_z we obtain

$$r_\alpha = \frac{2\pi\Omega_k}{\hbar c n_R} |\mathcal{M}_\alpha|^2 \int \frac{dk_\parallel}{(2\pi)^2} \left(\frac{k_0}{\sqrt{k_0^2 - k_\parallel^2}} + \frac{\sqrt{k_0^2 - k_\parallel^2}}{k_0} \right) \theta(k_0 - k_\parallel), \quad (\text{E.2})$$

where $k_0 = \frac{(E_g + E_\alpha)n_R}{\hbar c}$, which can be easily integrated

$$r_\alpha = \frac{2\pi\Omega_k}{\hbar c n_R} |\mathcal{M}_\alpha|^2 \frac{2k_0^2}{3\pi} = \frac{4}{3} \frac{E_g^3 n_R}{\hbar^4 c^3} d_{cv}^2 M_\alpha^2, \quad (\text{E.3})$$

where E_α was neglected since it is much smaller than bandgap energy E_g .

Appendix F

Strain

Here we show an example of the heavy and light hole potentials Eq. (1.22) of a nanoring embedded in a quantum well including strain within isotropic elasticity approach Eq. (1.122). This is depicted in Fig. F.1. The heavy hole minimum is found in the quantum well, unlike the light hole one which is outside. Since the confinement in the growth direction is strong enough, both particles are always found in the quantum well. Such a potential profiles guarantee that heavy and light hole are well energetically separated.

For the completeness, we list below the integrals which have to be evaluated.

F.1 Dot

In the case of the dot there are three contributions to the surface integral

$$T_{ij}(\mathbf{r}) = \oint_{S'} \frac{(x_i - x'_i) dS'_j}{|\mathbf{r} - \mathbf{r}'|^3}, \quad (\text{F.1})$$

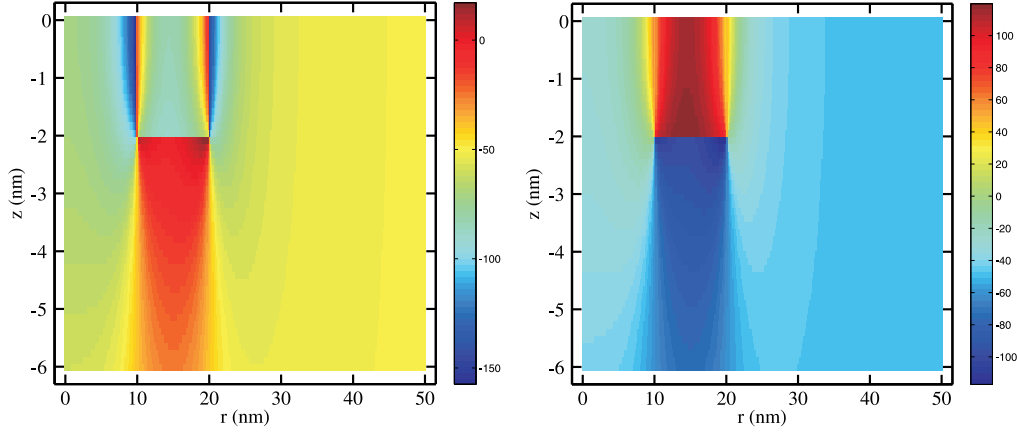


Figure F.1: The heavy (a) and light (b) hole potential profile Eq. (1.22) in meV. The quantum well is 4 nm wide and InP/GaInP ring radii are $r_1 = 10$ nm and $r_2 = 20$ nm. The material parameters are taken from Tab. A.1.

as shown in Fig. F.2a.

$$T_{zz}^{D1}(r, \phi, z) = - \int_0^{r_0} \int_0^{2\pi} \frac{(z+a) r' dr' d\phi'}{\sqrt{r'^2 + r^2 - rr' \cos(\phi - \phi') + (z+a)^2}^3}, \quad (\text{F.2})$$

$$T_{zz}^{D2}(r, \phi, z) = \int_0^{r_0} \int_0^{2\pi} \frac{(z-a) r' dr' d\phi'}{\sqrt{r'^2 + r^2 - rr' \cos(\phi - \phi') + (z-a)^2}^3}, \quad (\text{F.3})$$

$$T_{rr}^{D3}(r, \phi, z) = - \int_0^{2\pi} \int_{-a}^a \frac{(rr_0 \cos(\phi - \phi') - r_0^2) dz' d\phi'}{\sqrt{r_0^2 + r^2 - rr_0 \cos(\phi - \phi') + (z - z')^2}^3}. \quad (\text{F.4})$$

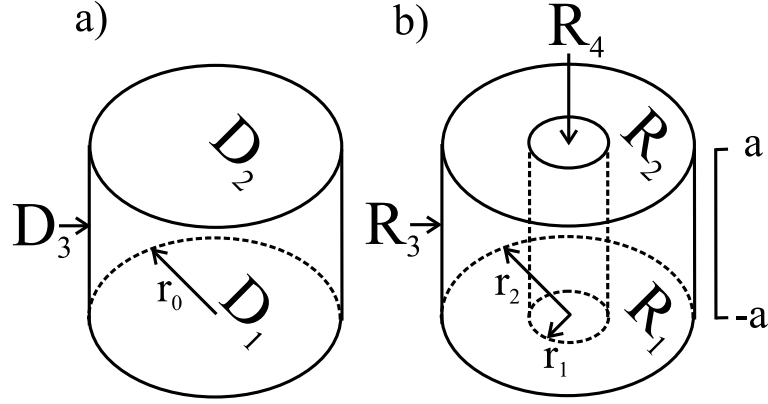


Figure F.2: Schematic picture of the dot a) and ring b) with indicated surfaces which are integrated over taking Eq. (F.1).

F.2 Ring

Similarly for the ring in Fig. F.2b, the following integrals are found

$$T_{zz}^{R_1}(r, \phi, z) = - \int_{r_1}^{r_2} \int_0^{2\pi} \frac{(z+a)r'dr'd\phi'}{\sqrt{r'^2 + r^2 - rr' \cos(\phi - \phi') + (z+a)^2}^3}, \quad (\text{F.5})$$

$$T_{zz}^{R_2}(r, \phi, z) = \int_{r_1}^{r_2} \int_0^{2\pi} \frac{(z-a)r'dr'd\phi'}{\sqrt{r'^2 + r^2 - rr' \cos(\phi - \phi') + (z-a)^2}^3}, \quad (\text{F.6})$$

$$T_{rr}^{R_3}(r, \phi, z) = - \int_0^{2\pi} \int_{-a}^a \frac{(rr_2 \cos(\phi - \phi') - r_2^2) dz' d\phi'}{\sqrt{r_2^2 + r^2 - rr_2 \cos(\phi - \phi') + (z-z')^2}^3}, \quad (\text{F.7})$$

$$T_{rr}^{R_4}(r, \phi, z) = - \int_0^{2\pi} \int_{-a}^a \frac{(-rr_1 \cos(\phi - \phi') + r_1^2) dz' d\phi'}{\sqrt{r_1^2 + r^2 - rr_1 \cos(\phi - \phi') + (z-z')^2}^3}. \quad (\text{F.8})$$

We note that all the results are due to the circular symmetry independent of angle ϕ (thus $\phi = 0$ may be set in all integrands).

Appendix G

List of abbreviations

ABE	Aharonov-Bohm effect
<i>B</i> -field	Magnetic field
μ PL	Micro-Photoluminescence
MBE	Molecular beam epitaxy
PC	Persistent current
PL	Photoluminescence
X-ABE	Exciton Aharonov-Bohm effect
XSTM	Cross-sectional scanning tunneling microscopy

Bibliography

- [AB59] Aharonov, Y.; Bohm, D.: Significance of electromagnetic potentials in the quantum theory. In: *Phys. Rev.*, volume 115:p. 485, 1959.
- [Ada94] Adachi, S.: *GaAs and Related Materials*. World Scientific, Singapore, 1994.
- [AJJA83] Alibert, C.; Joullié, A.; Joullié, A. M.; Ance, C.: Modulation-spectroscopy study of the $\text{Ga}_{1-x}\text{Al}_x\text{Sb}$ band structure. In: *Phys. Rev. B*, volume 27:p. 4946, 1983.
- [And58] Anderson, P. W.: Absence of diffusion in certain random lattices. In: *Phys. Rev.*, volume 109:p. 1492, Mar 1958.
- [And91] Andreani, L. C.: Radiative lifetime of free excitons in quantum wells. In: *Solid State Comm.*, volume 77:p. 641, 1991.
- [BAB⁺94] Brunner, K.; Abstreiter, G.; Böhm, G.; Tränkle, G.; Weimann, G.: Sharp-line photoluminescence and two photon absorption of zero dimensional biexcitons in a GaAs/AlGaAs structure. In: *Phys. Rev. Lett.*, volume 73:p. 1138, 1994.
- [Bas92] Bastard, G.: *Wave mechanics applied to semiconductor heterostructures*. Les éditions de physique, Paris, 1992.
- [BKH⁺03] Bayer, M.; Korkusinski, M.; Hawrylak, P.; Gutbrod, T.; Michel, M.; Forchel, A.: Optical detection of the Aharonov-Bohm effect on a charged particle in a nanoscale quantum ring. In: *Phys. Rev. Lett.*, volume 90:p. 186801, 2003.
- [BP74] Bir, G. L; Pikus, G. E.: *Symmetry and Strain-Induced Effects in Semiconductors*. Wiley, New York, 1974.

- [BPSP06] Barticevic, Z.; Pacheco, M.; Simonin, J.; Proetto, C. R.: Coulomb-interaction effects on the electronic structure of radially polarized excitons in nanorings. In: *Phys. Rev. B*, volume 73:p. 165311, 2006.
- [BSH⁺94] Blackwood, E.; Snelling, M. J.; Harley, R. T.; Andrews, S. R.; Foxon, C. T. B.: Exchange interaction of excitons in GaAs heterostructures. In: *Phys. Rev. B*, volume 50:p. 14246, 1994.
- [BSS⁺99] Bachtold, A.; Strunk, C.; Salvetat, J.-P.; Bonard, J.-M.; Forró, L.; Nussbaumer, T.; Schönenberger, C.: Aharonov-Bohm oscillations in carbon nanotubes. In: *Nature*, volume 397:p. 673, 1999.
- [BWO04] Barker, J. A.; Warburton, R. J.; O'Reilly, E. P.: Electron and hole wave functions in self-assembled quantum rings. In: *Phys. Rev. B*, volume 69:p. 035327, 2004.
- [CA75] Cho, A. Y.; Arthur, J. R.: Molecular beam epitaxy. In: *Prog. Solid State Chem.*, volume 10:p. 157, 1975.
- [CC92] Chao, C. Yi-Ping; Chuang, S. L.: Spin-orbit coupling effects on the valence band structure of strained semiconductor quantum wells. In: *Phys. Rev. B*, volume 46:p. 4110, 1992.
- [Cha60] Chambers, R. G.: Shift of an electron interference pattern by enclosed magnetic flux. In: *Phys. Rev. Lett.*, volume 5:p. 3, 1960.
- [Cha95] Chaplik, A. V.: Magnetoexcitons in quantum rings and in antidots. In: *Pis'ma Zh. Eksp. Teor. Fiz.*, volume 62:p. 885, 1995. [JETP Lett. **62**, 900 (1995)].
- [Cha02] Chaplik, A. V.: Aharonov-Bohm effect for composite particles and collective excitations. In: *Pis'ma Zh. Eksp. Teor. Fiz.*, volume 75:p. 343, 2002. [JETP Lett. **75**, 292 (2002)].
- [CM05] Citrin, D. S.; Maslov, A. V.: Interband optical spectra of magnetoexcitons in semiconductor nanorings: Electron-hole spatial correlation. In: *Phys. Rev. B*, volume 72:p. 073302, 2005.
- [CTCL96] Chiang, Jih-Chen; Tsay, Shiow-Fon; Chau, Z. M.; Lo, Ikai: Conduction-valence Landau level mixing effect. In: *Phys. Rev. Lett.*, volume 77:p. 2053, 1996.

- [CWB⁺91] Chandrasekhar, V.; Webb, R. A.; Brady, M. J.; Ketchen, M. B.; Gallagher, W. J.; Kleinsasser, A.: Magnetic response of a single, isolated gold loop. In: *Phys. Rev. Lett.*, volume 67:p. 3578, 1991.
- [Dap82] Dapkus, P. D.: Metalorganic chemical vapor deposition. In: *Annu. Rev. Mater. Sci.*, volume 12:p. 243, 1982.
- [Dav98] Davies, J. H.: Elastic and piezoelectric fields around a buried quantum dot: A simple picture. In: *J. Appl. Phys.*, volume 84:p. 1358, 1998.
- [dGGN⁺06] de Godoy, M. P. F.; Gomes, P. F.; Nakaema, M. K. K.; Iikawa, F.; Brasil, M. J. S. P.; Caetano, R. A.; Madureira, J. R.; Bortoleto, J. R. R.; Cotta, M. A.; Ribeiro, E.; Marques, G. E.; Bittencourt, A. C. R.: Exciton g -factor of type-II InP/GaAs single quantum dots. In: *Phys. Rev. B*, volume 73:p. 033309, 2006.
- [dSUG04] da Silva, L. G. G. V. Dias; Ulloa, S. E.; Govorov, A. O.: Impurity effects on the Aharonov-Bohm optical signatures of neutral quantum-ring magnetoexcitons. In: *Phys. Rev. B*, volume 70:p. 155318, 2004.
- [dSUS05] da Silva, Luis G. G. V. Dias; Ulloa, Sergio E.; Shahbazyan, Tigran V.: Polarization and Aharonov-Bohm oscillations in quantum-ring magnetoexcitons. In: *Phys. Rev. B*, volume 72:p. 125327, 2005.
- [dW89] de Walle, C. G. Van: Band lineups and deformation potentials in the model-solid theory. In: *Phys. Rev. B*, volume 39:p. 1871, 1989.
- [Eke89] Ekenberg, E.: Nonparabolicity effects in a quantum well: Sublevel shift, parallel mass, and Landau levels F. In: *Phys. Rev. B*, volume 40:p. 7714, 1989.
- [Ell57] Elliott, R. J.: Intesity of optical absorption by excitons. In: *Phys. Rev.*, volume 108:p. 1384, 1957.
- [ERW⁺06] Erdmann, M.; Ropers, C.; Wenderoth, M.; Ulbrich, R. G.; Malzer, S.; Döhler, G. H.: Diamagnetic shift of disorder-localized excitons in narrow GaAs/AlGaAs quantum wells. In: *Phys. Rev. B*, volume 74:p. 125412, 2006.

- [Fle80] Fleming, M.: X-ray diffraction study of interdiffusion and growth in $(\text{GaAs})_n(\text{AlAs})_m$ multilayers. In: *J. Appl. Phys.*, volume 51:p. 357, 1980.
- [GB94] Glutsch, S.; Bechstedt, F.: Theory of asymmetric broadening and shift of excitons in quantum structures with rough interfaces. In: *Phys. Rev. B*, volume 50:p. 7733, 1994.
- [GBW02] Galbraith, I.; Braid, F. J.; Warburton, R. J.: Magnetoexcitons in semiconductor quantum rings. In: *Phys. Stat. Sol. (A)*, volume 190:p. 781, 2002.
- [GCB96] Glutsch, S.; Chemla, D. S.; Bechstedt, F.: Numerical calculation of the optical absorption in semiconductor quantum structures. In: *Phys. Rev. B*, volume 54:p. 11592, 1996.
- [GMRS⁺97] García, J. M.; Medeiros-Ribeiro, G.; Schmidt, K.; Ngo, T.; Feng, J. L.; Lorke, A.; Kotthaus, J.; Petroff, P. M.: Inter-mixing and shape changes during the formation of InAs self-assembled quantum dots. In: *Appl. Phys. Lett.*, volume 71:p. 2014, 1997.
- [GSK95] Gammon, D.; Snow, E. S.; Katzer, D. S.: Excited state spectroscopy of excitons in single quantum dots. In: *Appl. Phys. Lett.*, volume 67:p. 2391, 1995.
- [GSS⁺96] Gammon, D.; Snow, E. S.; Shanabrook, B. V.; Katzer, D.S.; Par, D.: Fine structure splitting in the optical spectra of single GaAs quantum dots. In: *Phys. Rev. Lett.*, volume 76:p. 3005, 1996.
- [GU98] Governale, M.; Ungarelli, C.: Gauge-invariant grid discretization of the Schrödinger equation. In: *Phys. Rev. B*, volume 58:p. 7816, 1998.
- [GUKW02] Govorov, A. O.; Ulloa, S. E.; Karrai, K.; Warburton, R. J.: Polarized excitons in nanorings and the optical Aharonov-Bohm effect. In: *Phys. Rev. B*, volume 66:p. 081309, 2002.
- [GVG⁺97] Grousson, R.; Voliotis, V.; Grandjean, N.; Massies, J.; Leroux, M.; Deparis, C.: Microroughness and exciton localization in $(\text{Al,Ga})\text{As}/\text{GaAs}$ quantum wells. In: *Phys. Rev. B*, volume 55:p. 5253, 1997.

- [GVMPC94] Gurioli, M.; Vinattieri, A.; Martinez-Pastor, J.; Colocci, M.: Exciton thermalization in quantum-well structures. In: *Phys. Rev. B*, volume 50:p. 11817, 1994.
- [HBH⁺94] Hess, H. F.; Betzig, E.; Harris, T. D.; Pfeiffer, L. N.; West, K. W.: Near-field spectroscopy of the quantum constituents of a luminescent system. In: *Science*, volume 264:p. 1740, 1994.
- [HK94] Haug, H.; Koch, S. W.: *Quantum theory of the optical and electronic properties of semiconductors*. World Scientific, Singapore, 1994.
- [HZLX01] Hu, Hui; Zhu, Jia-Lin; Li, Dai-Jun; Xiong, Jia-Jiong: Aharonov-Bohm effect of excitons in nanorings. In: *Phys. Rev. B*, volume 63:p. 195307, 2001.
- [IEL⁺01] Intonti, F.; Emiliani, V.; Lienau, C.; Elsaesser, T.; Savona, V.; Runge, E.; Zimmermann, R.; Nötzel, R.; Ploog, K. H.: Quantum mechanical repulsion of exciton levels in a disordered quantum well. In: *Phys. Rev. Lett.*, volume 87:p. 76801, 2001.
- [Inc01] Inc., The MathWorks: Matlab v6.1, 2001.
- [JPP01] Janssens, K. L.; Partoens, B.; Peeters, F. M.: Magnetoexcitons in planar type-II quantum dots in a perpendicular magnetic field. In: *Phys. Rev. B*, volume 64:p. 155324, 2001.
- [JPP03] Janssens, K. L.; Partoens, B.; Peeters, F. M.: Effect of strain on the magnetoexciton ground state in InP/GaInP quantum disks. In: *Phys. Rev. B*, volume 67:p. 235325, 2003.
- [Kea66] Keating, P. N.: Effect of invariance requirement on the elastic strain energy of crystal with application to diamond structure. In: *Phys. Rev.*, volume 145:p. 637, 1966.
- [KKG98] Kalameitsev, A.B.; Kovalev, V.M.; Govorov, A.O.: Magnetoexcitons in type-II quantum dots. In: *Pis'ma Zh. Eksp. Teor. Fiz.*, volume 68:p. 634, 1998. [JETP Lett. **68**, 669 (1998)].
- [KLW⁺03] Kocherscheidt, G.; Langbein, W.; Woggon, U.; Savona, V.; Zimmermann, R.; Reuter, D.; Wieck, A. D.: Resonant

- Rayleigh scattering dynamics of excitons in single quantum wells. In: *Phys. Rev. B*, volume 68:p. 085207, 2003.
- [KMO⁺05] Kuroda, T.; Mano, T.; Ochiai, T.; Sanguinetti, S.; Sakoda, K.; Kido, G.; Koguchi, N.: Optical transitions in quantum ring complexes. In: *Phys. Rev. B*, volume 72:p. 205301, 2005.
- [LDDDB90] Lévy, L. P.; Dolan, G.; Dunsmuir, J.; Bouchiat, H.: Magnetization of mesoscopic copper rings: Evidence for persistent currents. In: *Phys. Rev. Lett.*, volume 64:p. 207490, 1990.
- [LG96] Loan, C. F. Van; Golub, G. H.: *Matrix Computations*. John Hopkins University Press, Baltimore, 1996.
- [LK55] Luttinger, J. M.; Kohn, W.: Motion of electrons and holes in perturbed periodic fields. In: *Phys. Rev.*, volume 97:p. 869, 1955.
- [LL59] Landau, L.D.; Lifshitz, E. M.: *Theory of elasticity*. Pergamon press, London, 1959.
- [LLG⁺00] Lorke, Axel; Luyken, R. Johannes; Govorov, Alexander O.; Kotthaus, Jörg P.; Garcia, J. M.; Petroff, P. M.: Spectroscopy of nanoscopic semiconductor rings. In: *Phys. Rev. Lett.*, volume 84:p. 2223, 2000.
- [LOV⁺02] Lozovik, Yu. E.; Ovchinnikov, I. V.; Volkov, S. Yu.; Butov, L. V.; Chemla, D. S.: Quasi-two-dimensional excitons in finite magnetic fields. In: *Phys. Rev. B*, volume 65:p. 235304, 2002.
- [LRSZ02] Langbein, W.; Runge, E.; Savona, V.; Zimmermann, R.: Enhanced resonant backscattering of excitons in disordered quantum wells. In: *Phys. Rev. Lett.*, volume 89:p. 157401, 2002.
- [LRZ03] Ludwig, H.; Runge, E.; Zimmermann, R.: Exact calculation of distributions for excitonic oscillator strength and inverse participation ratio in disordered quantum wires. In: *Phys. Rev. B*, volume 67:p. 205302, 2003.
- [Lyo94] Lyo, S. K.: Theory of magnetic-field-dependent alloy broadening of exciton-photoluminescence linewidths in semiconductor alloys. In: *Phys. Rev. B*, volume 48:p. 2152, 1994.

- [LZY⁺98] Lew, A. Y.; Zou, S. L.; Yu, E.; Chow, D. H.; Miles, R. H.: Correlation between atomic-scale structure and mobility anisotropy in InAs/Ga_{1-x}In_xSb superlattices. In: *Phys. Rev. B*, volume 57:p. 6534, 1998.
- [MB62] Möllenstedt, G.; Bayh, W.: Messung der kontinuierlichen Phasenschiebung von Elektronenwellen im kraftfeldfreien Raum durch das magnetische Vektorpotential einer Luftspule. In: *Naturwiss.*, volume 49:p. 81, 1962.
- [MC03] Maslov, A. V.; Citrin, D. S.: Enhancement of the Aharonov-Bohm effect of neutral excitons in semiconductor nanorings with an electric field. In: *Phys. Rev. B*, volume 67:p. 121304, 2003.
- [MC04] Mouloupoulos, K.; Constantinou, M.: Two interacting charged particles in an Aharonov-Bohm ring: Bound state transitions, symmetry breaking, persistent currents, and Berry's phase. In: *Phys. Rev. B*, volume 70:p. 235327, 2004.
- [MCB93] Mailly, D.; Chapelier, C.; Benoit, A.: Experimental observation of persistent currents in GaAs-AlGaAs single loop. In: *Phys. Rev. Lett.*, volume 70:p. 2020, 1993.
- [MKS⁺05] Mano, T.; Kuroda, T.; Sanguinetti, S.; Ochiai, T.; Tateno, T.; Kim, J.; Noda, T.; Kawabe, M.; Sakoda, K.; Kido, G.; Koguchi, N.: Self-assembly of concentric quantum double rings. In: *Nano Lett.*, volume 5:p. 425, 2005.
- [MZKL03] Mannarini, G.; Zimmermann, R.; Kocherscheidt, G.; Langbein, W.: Density-matrix description of frequency-resolved secondary emission from quantum wells. In: *Phys. Stat. Sol. (B)*, volume 238:p. 494, 2003.
- [OFO05] Ohtani, K.; Fujita, K.; Ohno, H.: Mid-infrared InAs/AlGaSb superlattice quantum-cascade lasers. In: *Appl. Phys. Lett.*, volume 87:p. 211113, 2005.
- [OTC89] Ourmazd, A.; Taylor, D. W.; Cunningham, J.: Chemical mapping of semiconductor interfaces at near-atomic resolution. In: *Phys. Rev. Lett.*, volume 62:p. 933, 1989.

- [PDER05] Palmero, F.; Dorignac, J.; Eilbeck, J. C.; Römer, R. A.: Aharonov-Bohm effect for an exciton in a finite-width nanoring. In: *Phys. Rev. B*, volume 72:p. 075343, 2005.
- [Pei32] Peierls, R.: Zur Theorie des Diamagnetismus von Leitungselektronen. In: *Zeitschrift für Physik*, volume 80:p. 763, 1932.
- [PHJ⁺05] Persson, J.; Hakanson, U.; Johansson, M. K.-J.; Samuelson, L.; Pistol, M.-E.: Strain effects on individual quantum dots: Dependence of cap layer thickness. In: *Phys. Rev. B*, volume 72:p. 085302, 2005.
- [PP05] Pryor, C. E.; Pistol, M.-E.: Band-edge diagrams for strained III-V semiconductor quantum wells, wires, and dots. In: *Phys. Rev. B*, volume 72:p. 205311, 2005.
- [PTVF02] Press, W. H.; Teukolsky, S. A.; Vetterling, W. T.; Flannery, B. P.: *Numerical recipes in C++*. Cambridge University Press, Cambridge, 2002.
- [REW⁺07] Ropers, C.; Erdmann, M.; Wenderoth, M.; Ulbrich, R. G.; Malzer, S.; Döhler, G. H.; Grochol, M.; Grosse, F.; Zimmermann, R.: Atomic scale structure and optical emission of AlGaAs/GaAs quantum wells. In: *Phys. Rev. B*, volume 75:p. 115317, 2007.
- [RGWCMR04] Ribeiro, E.; Govorov, A. O.; W. Carvalho, Jr.; Medeiros-Ribeiro, G.: Aharonov-Bohm signature for neutral polarized excitons in type-II quantum dot ensembles. In: *Phys. Rev. Lett.*, volume 92:p. 126402, 2004.
- [RMJ⁺95] Runge, E.; Menninger, J.; Jahn, U.; Hey, R.; Grahn, H. T.: Roughness of heterointerfaces and averaging effects by excitons: Interpretation of cathodoluminescence images. In: *Phys. Rev. B*, volume 52:p. 12207, 1995.
- [RR00] Römer, R. A.; Raikh, M. E.: Aharonov-Bohm effect for an exciton. In: *Phys. Rev. B*, volume 62:p. 7045, 2000.
- [RSN⁺86] Rogers, D. C.; Singleton, J.; Nicholas, R. J.; Foxon, C. T.; Woodbridge, K.: Magneto-optics in GaAs-Ga_{1-x}Al_xAs quantum wells. In: *Phys. Rev. B*, volume 34:p. 4002, 1986.

- [Run02] Runge, E.: Excitons in semiconductor nanostructures. In: *Solid State Physics*, volume 57:pp. 149 – 305, 2002. Ed. by H. Ehrenreich and F. Spaepen.
- [RZ00] Runge, E.; Zimmermann, R.: Porter-Thomas distribution of oscillator strengths of quantum well excitons. In: *Phys. Stat. Sol. (B)*, volume 221:p. 269, 2000.
- [SA93] Salemink, H. W. M.; Albrechtsen, O.: Atomic-scale composition fluctuations in III-V semiconductor alloys. In: *Phys. Rev. B*, volume 47:p. 16044, 1993.
- [SAK01] Siantidis, K.; Axt, V. M.; Kuhn, T.: Dynamics of exciton formation for near band-gap excitations. In: *Phys. Rev. B*, volume 65:p. 035303, 2001.
- [SAS95] Someya, T.; Akiyama, H.; Sakaki, H.: Laterally squeezed excitonic wave function in quantum wires. In: *Phys. Rev. Lett.*, volume 74:p. 3664, 1995.
- [SBJ⁺03] Senger, R. T.; Bajaj, K. K.; Jones, E. D.; Modine, N. A.; Waldrip, K. E.; Jalali, F.; Klem, J. F.; Peake, G. M.; Wei, X.; Tozer, S. W.: Magnetoluminescence properties of GaAsSbN/GaAs quantum well structures. In: *Appl. Phys. Lett.*, volume 83:p. 5425, 2003.
- [SBMH92] Snelling, M. J.; Blackwood, E.; McDonagh, C. J.; Harley, R. T.: Exciton, heavy hole, and electron g -factors in type-I GaAs/Al_xGa_{1-x}As quantum wells. In: *Phys. Rev. B*, volume 45:p. 3922, 1992.
- [SD01] Stroschio, M. A.; Dutta, M.: *Phonons in nanostructures*. Cambridge University Press, Cambridge, 2001.
- [SDL⁺89] Smith, Doran D.; Dutta, M.; Liu, X. C.; Terzis, A. F.; Petrou, A.; Cole, M. W.; Newman, P. G.: Magnetoexciton spectrum of GaAs-AlAs quantum wells. In: *Phys. Rev. B*, volume 40:p. 1407, Jul 1989. doi:10.1103/PhysRevB.40.1407.
- [SRZ00] Siarkos, A.; Runge, E.; Zimmermann, R.: Center-of-mass properties of the exciton in quantum wells. In: *Phys. Rev. B*, volume 61:p. 10854, 2000.

- [SS81] Sharvin, D. Y.; Sharvin, Y. V.: Magnetic-flux quantization in a cylindrical film of a normal metal. In: *Pis'ma Zh. Eksp. Teor. Fiz*, volume 34:p. 285, 1981. [JETP Lett. **34**, 272 (1982)].
- [SU01] Song, J.; Ulloa, S. E.: Magnetic field effects on quantum ring excitons. In: *Phys. Rev. B*, volume 63:p. 125302, 2001.
- [Tak85] Takagahara, T.: Localization and energy transfer of quasi-two-dimensional excitons in GaAs-AlAs quantum-well heterostructures. In: *Phys. Rev. B*, volume 31:p. 6552, 1985.
- [TEL⁺04] Timm, R.; Eisele, H.; Lenz, A.; Becker, S. K.; Grabowski, J.; Kim, T.-Y.; Müller-Kirsch, L.; Pötschke, K.; Pohl, U. W.; Bimberg, D.; Dähne, M.: Structure and intermixing of GaSb/GaAs quantum dots. In: *Appl. Phys. Lett.*, volume 85:p. 5890, 2004.
- [TOIM84] Tarucha, S.; Okamoto, H.; Iwasa, Y.; Miura, N.: Exciton binding energy in GaAs quantum wells deduced from magneto-optical absorption measurement. In: *Solid State Comm.*, volume 52:p. 815, 1984.
- [TPJ⁺02] Tadić, M.; Peeters, F. M.; Janssens, K. L.; Korkusiński, M.; Hawrylak, P.: Strain and band edges in single and coupled cylindrical InAs/GaAs and InP/InGaP self-assembled quantum dots. In: *J. Appl. Phys.*, volume 92:p. 5819, 2002.
- [TTZGB90] Tran Thoai, D. B.; Zimmermann, R.; Grundmann, M.; Bimberg, D.: Image charges in semiconductor quantum wells: Effect on exciton binding energy. In: *Phys. Rev. B*, volume 42:p. 5906, 1990.
- [VMRM01] Vurgaftman, I.; Meyer, J. R.; Ram-Mohan, L. R.: Band parameters for III-V compound semiconductors and their alloys. In: *J. Appl. Phys.*, volume 89:p. 5815, 2001.
- [vODNM98] van Oudenaarden, A.; Devoret, M. H.; Nazarov, Yu. V.; Mooij, J. E.: Magneto-electric Aharonov-Bohm effect in metal rings. In: *Nature*, volume 391:p. 768, 1998.
- [VS] Vogl, P.; Scholz, R.: recent k.p calculations. Private communication.

- [WF95] Wendler, L.; Fomin, V. M.: Possible bistability of the persistent current of two interacting electrons in a quantum ring. In: *Phys. Rev. B*, volume 51:p. 17814, 1995.
- [WFC95] Wendler, L.; Fomin, V. M.; Chaplik, A. V.: Persistent currents of few interacting electrons in mesoscopic rings. In: *Solid State Comm.*, volume 96:p. 809, 1995.
- [WFK94] Wendler, L.; Fomin, V. M.; Krokhin, A. A.: Relation between persistent current and band structure of finite-width mesoscopic rings. In: *Phys. Rev. B*, volume 50:p. 4642, 1994.
- [WG88] Wendler, L.; Grigoryan, V. G.: Acoustic interface waves in sandwich structures. In: *Surface Sci.*, volume 206:p. 203, 1988.
- [WH91] Wendler, L.; Hartwig, B.: Effect of the image potential on the binding energy of excitons in semiconductor quantum wells. In: *J. Phys. C*, volume 3:p. 9907, 1991.
- [Wil74] Wilson, K.: Confinement of quarks. In: *Phys. Rev. D*, volume 10:p. 2445, 1974.
- [WMBW94] Wendler, E.; Müller, P.; Bachmann, T.; Wesch, W.: Sub-gap optical properties of amorphous InP produced by ion implantation. In: *J. Non-crystal. Solids*, volume 176:p. 85, 1994.
- [WR98] Walck, S. N.; Reinecke, T. L.: Exciton diamagnetic shift in semiconductor nanostructures. In: *Phys. Rev. B*, volume 57:p. 9088, 1998.
- [WS98] Wu, K.; Simon, H.: Thick-restart Lanczos method for symmetric eigenvalue problems. Technical Report 41284, Lawrence Berkeley National Laboratory, 1998.
- [WS99] Wu, K.; Simon, H.: Thick-restart Lanczos method for electronic structure calculations. Technical Report 42917, Lawrence Berkeley National Laboratory, 1999.
- [XCQ92] Xia, X.; Chen, X. M.; Quinn, J. J.: Magnetoexcitons in a GaSb-AlSb-InAs quantum-well structure. In: *Phys. Rev. B*, volume 46:p. 7212, 1992.

- [YAGO04] Yamamoto, N.; Akahane, K.; Gozu, S.; Ohtani, N.: Growth of InAs quantum dots on a low lattice-mismatched AlGaSb layer prepared on GaAs(001) substrates. In: *Solid State Phenom.*, volume 99-100:p. 49, 2004.
- [YC94] Yu, P. Y.; Cardona, M.: *Fundamentals of Semiconductors*. Springer, Heidelberg, 1994.
- [ZBH⁺94] Zrenner, A.; Butov, L. V.; Hagn, M.; Abstreiter, G.; Böhm, G.; Weimann, G.: Quantum dots formed by interface fluctuations in AlAs/GaAs coupled quantum well structures. In: *Phys. Rev. Lett.*, volume 72:p. 3382, 1994.
- [ZGR97] Zimmermann, R.; Grosse, R.; Runge, E.: Excitons in semiconductor nanostructures with disorder. In: *Pure Appl. Chem.*, volume 69:p. 1179, 1997.
- [ZRS03] Zimmermann, R.; Runge, E.; Savona, V.: *Theory of Resonant Secondary Emission: Rayleigh Scattering versus Luminescence*. Academic Press, San Diego, 2003.
- [ZZC05] Zhang, T. Y.; Zhao, W.; Cao, J. C.: Optical response in a quantum dot superlattice nanoring under a lateral electric field. In: *Phys. Rev. B*, volume 72:p. 165310, 2005.

Danksagung

An erster Stelle muß und möchte ich ganz herzlich meinem Betreuer Prof. Dr. Roland Zimmermann für die Möglichkeit danken, in seiner Arbeitsgruppe an dieser Dissertation arbeiten zu dürfen. Es war die ganze Zeit möglich mit ihm, bei der Physik zu diskutieren und zu lernen, wie ordentliche Wissenschaft gemacht werden muß. Sein breiter Überblick in der Physik hat mir viel gebracht und auch ermöglicht, meine eigene Perspektive zu erweitern. Obwohl die Diskussion oft hart und die Kritik scharf war, bin ich dafür sehr dankbar, weil ich vorab viele Fehler vermeiden konnte. Natürlich muß ich ihm auch für die Bereitstellung des Stipendiums im Rahmen des Graduierten-Kollegs 1024 der Deutschen Forschungsgemeinschaft danken, wo ich andere Doktoranden kennengelernt habe und den interessanten Vorträgen der Kollegen zuhören konnte.

An zweiter Stelle danke ich selbstverständlich Dr. Frank Große, der mir hauptsächlich am Anfang viel geholfen hat und immer bereit war, auch über Dinge außerhalb der Physik zu diskutieren. Nicht zuletzt muß ich erwähnen, daß seine Anforderung an die numerische Genauigkeit bis zur letzten Stelle sich oft als ganz sinnvoll herausgestellt hat.

Dann danke ich allen Mitgliedern der Arbeitsgruppe Halbleitertheorie, die ich während dieser dreieinhalb Jahre getroffen habe. Insbesondere Dr. Egor A. Muljarov bin ich dankbar für viele hilfreiche Diskussionen über analytische Rechnungen und die Physik allgemein. Weiter möchte ich danken den ehemaligen Kollegen Dr. Gianandrea Mannarini für seinen unzerstörbaren Optimismus, der immer die Stimmung verbessert hat, und für die Verwaltung der Windowsrechner, Claus Ropers für interessante Diskussionen wegen unseres gemeinsamen Papers, Dr. Luxia Wang für die Möglichkeit etwas interessantes über China erfahren zu dürfen, Dr. Ben Brüggemann für die Hilfe mit der Betreuung der Linuxrechner, Hannes Guhl für viele interessante Diskussionen auch über die Physik, und zuletzt PD Dr. Volkhard May für die Möglichkeit ein etwas anderes Fach der Physik kennenlernen zu können.

Ein spezieller Dank gehört Prof. Dr. Lutz Wendler für viele interessante Gespräche und das Lesen der Manuskripte meiner Artikel und der Entwürfe

dieser Dissertation.

Die Betreuung der Linuxrechner und die Mehrzahl meiner numerischen Ergebnisse wären nicht möglich ohne große Hilfe der Mitarbeiter des Institutsrechnerzentrums gewesen, nämlich Michael Happ, Volkmar Ullrich und Dr. Burkhard Bunk, der auch teilweise die Verwaltung unseres Netzwerkes übernommen hat.

Schließlich habe ich während dieser Zeit die Zusammenarbeit und Freundschaft mit diesen Personen genossen: Sekretärin Marion Heider, Dr. Andreas Kaiser, Andreas Knittel, Rita Leite, Dr. Milana Michaljowa, Christoph Schindler, Dr. Dmitry Tsvilin, und Dr. Hui Zhu.

V neposlední řadě musím samozřejmě poděkovat své manželce Janě za velkou trpělivost a neutuchající podporu, za níž jsem také vděčen svým rodičům a bratrovi.

Lebenslauf

Persönliches:

Name: Michal Grochol
Geburtsdatum: 22.10.1979
Geburtsort: Ostrava, Tschechische Republik
Nationalität: tschechisch
Familienstand: verheiratet

Ausbildung:

1992-1998 Gymnázium Ostrava-Zábřeh, Tschechische Republik
1998-2003 Studium der Physik an der Karls-Universität in Prag
2003 Diplomarbeit zum Thema:
*Luminescence Spectroscopy of Semiconductor
Quantum Structures*
unter Betreuung von PD Dr. R. Grill
2003-2007 Promotion an der Humboldt-Universität zu Berlin,
Thema:
*Optical Properties of Semiconductor Nanostructures
in Magnetic Field*
unter Betreuung von Prof. Dr. R. Zimmermann

Aufstellung der wissenschaftlichen Veröffentlichungen

Zeitschriftenartikel im Rahmen der Dissertation

1. M. Grochol, F. Grosse, and R. Zimmermann
Diamagnetic shift and localization of excitons in disordered quantum wells
J. Luminescence **112**, 208-211 (2005) (Proc. EXCON 6, Cracow).
2. M. Grochol, F. Grosse, and R. Zimmermann
Exciton wave function properties probed by diamagnetic shifts in disordered quantum wells
Phys. Rev. B **71**, 125339 (2005).
3. M. Grochol, F. Grosse, and R. Zimmermann
Exciton Aharonov-Bohm effect in quantum dot rings
Phys. Stat. Sol. (C) **3**, 2518-2521 (2006) (Proc. NOEKS 8, Mnster).
4. M. Grochol, F. Grosse, and R. Zimmermann
Optical exciton Aharonov-Bohm effect, persistent current, and magnetization in semiconductor nanorings of type I and II
Phys. Rev. B **74**, 115416 (2006).
5. M. Grochol, F. Grosse, and R. Zimmermann
Exciton Aharonov-Bohm effect and emission kinetics in nanorings
Phys. Stat. Sol. (B) **243**, 3834-3839 (2006), (Proc. EXCON 7, Winston-Salem).

6. M. Grochol, F. Grosse, and R. Zimmermann
Exciton diamagnetic shift in realistic quantum wells
Phys. Stat. Sol. (C) **3**, 3492-3495 (2006), (Proc. EXCON 7, Winston-Salem).
7. M. Grochol, F. Grosse, and R. Zimmermann
Exciton Aharonov-Bohm Effect in Embedded Nanostructures
ICPS 28 Proc., in press.
8. C. Ropers, M. Wenderoth, L. Winking, T. C. G. Reusch, M. Erdmann, R. G. Ulbrich, M. Grochol, F. Grosse, R. Zimmermann, S. Malzer and G. H. Döhler
Atomic Scale Structure and Optical Emission of AlGaAs/GaAs Quantum Wells
Phys. Rev. B **75**, 115317 (2007).

Tagungsbeiträge

1. M. Grochol, F. Grosse, and R. Zimmermann
Diamagnetic Shift and Localization of Excitons in Disordered Quantum Wells
DPG Tagung, Regensburg, 2004: Poster contribution
2. M. Grochol, F. Grosse, and R. Zimmermann
Diamagnetic Shift and Localization of Excitons in Disordered Quantum Wells
EXCON 6, Cracow, 2004: Poster contribution
3. M. Grochol, F. Grosse, and R. Zimmermann
Exciton Diamagnetic Shift Reveals New Features in Disorder Statistics
DPG Tagung, Berlin, 2005: Oral contribution
4. M. Grochol, F. Grosse, and R. Zimmermann
Exciton Aharonov-Bohm effect in type II quantum rings
OECS 9, Southampton, 2005: Oral contribution
5. M. Grochol, F. Grosse, and R. Zimmermann
Exciton Aharonov-Bohm effect and dynamics in quantum rings
NOEKS 8, Münster, 2006: Oral contribution
6. M. Grochol, F. Grosse, and R. Zimmermann
Exciton Aharonov-Bohm effect in type I and II nanorings

DPG Tagung, Dresden, 2006: Oral contribution

7a. M. Grochol, F. Grosse, and R. Zimmermann
Exciton Aharonov-Bohm effect and kinetics in nanostructures
EXCON 7, Winston-Salem, 2006: Oral poster contribution

7b. M. Grochol, F. Grosse, and R. Zimmermann
Exciton diamagnetic shift in realistic quantum wells
EXCON 7, Winston-Salem, 2006: Oral contribution

8. M. Grochol, F. Grosse, and R. Zimmermann
Exciton Aharonov-Bohm effect in embedded nanostructures
ICPS 28, Vienna, 2006: Poster contribution

Selbständigkeitserklärung

Hiermit erkläre ich, die vorliegende Arbeit selbständig ohne fremde Hilfe verfaßt zu haben und nur die angegebene Literatur und Hilfsmittel verwendet zu haben.

Michal Grochol
Berlin, den 15. Januar 2007